



Cite as

Nano-Micro Lett.

(2023) 15:68

Recent Advances and Perspectives of Lewis Acidic Etching Route: An Emerging Preparation Strategy for MXenes

Pengfei Huang¹, Wei-Qiang Han¹ ✉

Received: 6 January 2023

Accepted: 5 February 2023

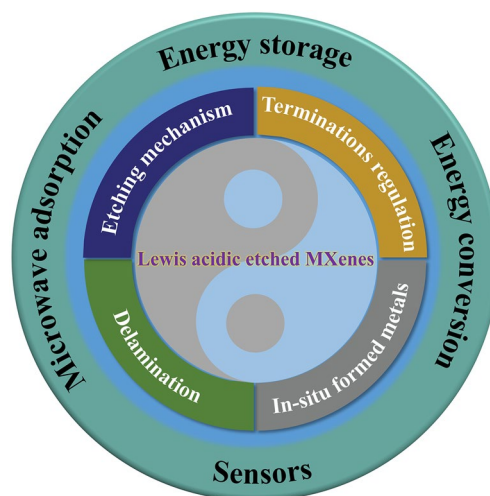
© The Author(s) 2023

HIGHLIGHTS

- As an emerging preparation strategy for MXenes, Lewis acidic etching has attracted increasing attention in the past few years benefiting from a series of merits.
- Lewis acidic etching method is mainly presented from etching mechanism, terminations regulation, in-situ formed metals and delamination of multi-layered MXenes.
- The applications of MXenes and MXene-based composites obtained by Lewis acidic etching route in energy storage and conversion, sensors and microwave adsorption are carefully summarized.

ABSTRACT Since the discovery in 2011, MXenes have become the rising star in the field of two-dimensional materials. Benefiting from the metallic-level conductivity, large and adjustable gallery spacing, low ion diffusion barrier, rich surface chemistry, superior mechanical strength, MXenes exhibit great application prospects in energy storage and conversion, sensors, optoelectronics, electromagnetic interference shielding and biomedicine. Nevertheless, two issues seriously deteriorate the further development of MXenes. One is the high experimental risk of common preparation methods such as HF etching, and the other is the difficulty in obtaining MXenes with controllable surface groups. Recently, Lewis acidic etching, as a brand-new preparation strategy for MXenes, has attracted intensive attention due to its high safety and the ability to endow MXenes with uniform terminations. However, a comprehensive review of Lewis acidic etching method has not been reported yet. Herein, we first introduce the Lewis acidic etching from the following four aspects: etching mechanism, terminations regulation, in-situ formed metals and delamination of multi-layered MXenes. Further, the applications of MXenes and MXene-based hybrids obtained by Lewis acidic etching route in energy storage and conversion, sensors and microwave adsorption are carefully summarized. Finally, some challenges and opportunities of Lewis acidic etching strategy are also presented.

KEYWORDS Lewis acidic etching; MXenes; Etching mechanism; Termination regulation; In-situ formed metals; Delamination; Application



✉ Wei-Qiang Han, hanwq@zju.edu.cn

¹ School of Materials Science and Engineering, Zhejiang University, Hangzhou 310027, People's Republic of China

1 Introduction

The great success of graphene triggers enormous exploration in other two-dimensional (2D) materials, such as transition metal dichalcogenides, hexagonal boron nitride, layered double hydroxides (LDHs), graphitic carbon nitride, germanene, and black phosphorus [1–10]. In 2011, multi-layered $Ti_3C_2T_x$ was first reported by Gogotsi and Barsoum's group, which announces the birth of a brand-new and large family of 2D materials, namely transition metal carbides, nitrides and carbonitrides termed as MXenes [11–13]. They are generally derived from MAX precursors which possess

a formula of $M_{n+1}AX_n$ ($n=1-4$), where M stands for early transition metals (e.g., Ti, Ta, V, Mo, Nb, and Cr), A is mainly group 13 or 14 elements, such as Al, Si and Ga, and X refers to carbon or nitrogen (Fig. 1a) [14–16]. So far, 155 MAX phases have been successfully synthesized [17]. It is worth mentioning that some non-MAX ternary layered compounds such as Mo_2Ga_2C , $Zr_3Al_3C_5$ and $Hf_3Al_3C_5$ can also be used as precursors to prepare MXenes [18–21]. Structurally, MAX precursors possess typical hexagonal closely packed crystal structure with a $P6_3/mmc$ space group, and they are established by stacking of $M_{n+1}X_n$ building blocks that are interleaved with A-site atom layer along the

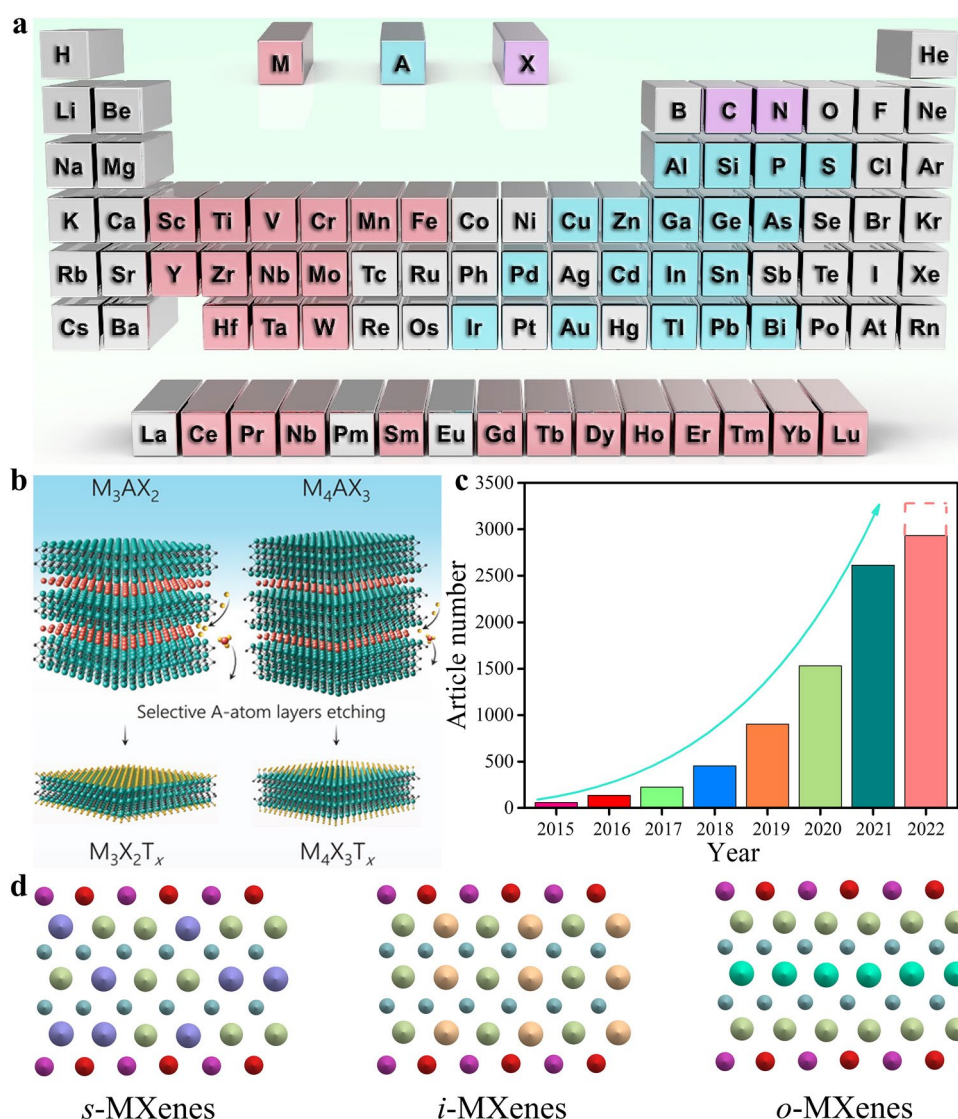


Fig. 1 **a** Element composition of MAX phase. Reproduced with permission from [16] Copyright 2022, Elsevier. **b** Schematic illustration of the preparation of various MXenes from corresponding MAX phases. Reproduced with permission from [26] Copyright 2021, Wiley-VCH. **c** The annual published article numbers of MXenes. **d** Schematic of *s*-MXenes, *i*-MXenes and *o*-MXenes

c direction, leading to strong M-X covalent/metallic/ionic mixed bond and weak M-A metallic bond [21–23]. The difference in bond strength allows the A-site atoms to be selectively removed from MAX phase by a top-down method, and the remaining loosely stacked $M_{n+1}X_n$ architectures terminated with mixed surface groups T (e.g., –O, –OH, and –F) are named as MXenes, leading to a general chemical formula of $M_{n+1}X_nT_x$ ($n = 1–4$, $x \leq 2$) (Fig. 1b) [24–26].

The publications of MXenes have increased significantly in the past eight years and reach around 2600 in 2021 (Fig. 1c). It is noteworthy that the majority of reported articles are focused on $Ti_3C_2T_x$ MXene owing to its superior electronic conductivity ($24,000 \text{ S cm}^{-1}$) and large interlayer spacing [27–30]. Correspondingly, great progress has been achieved in the development of MXenes, especially in compositional and structural diversity. First, there are four kinds of MXenes with different stoichiometries including M_2XT_x , $M_3X_2T_x$, $M_4X_3T_x$ and $M_5X_4T_x$ [27, 31–33]. Then, when the number of elements at the M-site exceeds two, MXenes can be categorized into three types according to the distribution of M-site atoms, namely *s*-MXenes with disordered arrangement, *i*-MXenes with in-plane ordering and *o*-MXenes with out-of-plane ordering (Fig. 1d) [15, 34–36]. Additionally, X-site atoms can be occupied by carbon, nitrogen or both [37–39]. Furthermore, the surface groups of MXenes mainly comprise of –O, –OH, –F, –Cl, –Br, –I, –S, –Se, –Te, –NH, etc., and can also be adjusted by etchants, termination substitution reaction and storage environment [40–43]. To date, nearly 50 various MXenes have been experimentally fabricated [44]. Considering the great tunability of M-site atoms, X-site atoms and surface terminations as well as the structural diversity of MXenes (Fig. 2), the number of MXenes will increase dramatically in the near future, eventually developing into a huge family [45].

MXenes generally exhibit a series of unique properties, including superior electronic conductivity, large and tunable gallery spacing, low ion diffusion barrier, rich surface chemistry, outstanding redox activity, hydrophilicity and wonderful mechanical strength (Fig. 2), making MXenes promising candidates for various fields [34, 45–48]. Specifically, large gallery spacing and rapid ion migration kinetics allow their use in high-performance metal-ion batteries and supercapacitors (SCs) [28, 39, 49, 50]. Flexibility, rich surface chemistry, adjustable interlayer spacing and high mechanical strength of MXenes enable them to be utilized as advanced separation membranes [51]. Excellent

electronic conductivity and light weight of MXenes permit their apply in electromagnetic interference shielding, and ample redox centers endow them with superior catalysis capability [52–54]. Additionally, MXenes colloidal solution can be readily processed into freestanding papers and additive-free inks owing to the superior hydrophilicity [55, 56]. More importantly, the large compositional space, structural diversity and rich interlayer environment of MXenes offer great possibilities for unique combination and adjustability of properties (Fig. 2). For example, nitride MXenes display stronger polarity, higher electronic conductivity and more active sites compared with carbide counterparts, which renders them promising materials for secondary batteries [57]. Besides, high entropy MXenes such as $(Ti_{1/5}V_{1/5}Zr_{1/5}Nb_{1/5}Ta_{1/5})_2CT_x$ offers high mechanical strain owing to the distinct lattice distortions, which can effectively induce the uniform nucleation and deposition of Li metal [58]. Last but not least, the terminations play a key role in tuning the physicochemical characteristics of MXenes, especially in electronic properties. For example, MXenes without surface group possess high electron density near the Fermi level, while surface groups can generally alter the density of states and shift the Fermi level, finally resulting in semiconductor-like characteristics [59–61]. Furthermore, Nb_2C MXene with –Cl, –S or –Se surface groups demonstrated superconductivity, whereas the O or F-terminated Nb_2C fail to enter the superconducting state in the low-temperature region [42, 62]. In summary, MXenes have been widely explored in various fields up to now and the great tunability of electronic, optical, magnetic, mechanical and thermal properties would gradually expand their applications in the future [45, 63].

The effective synthesis strategy is able to adjust the properties of MXenes and make large-scale manufacturing possible [43, 64]. Until now, various preparation approaches for MXenes have been proposed. HF aqueous solution was first exploited to etch MAX precursors in 2011, which endows MXenes with distinct accordion-like morphology and mixed terminations of –OH, –O and –F [11]. However, the strong corrosiveness of HF prevents some researchers from participating in the research of MXenes. In 2014, Ghidui et al. reported the in-situ formation of HF etchant by simply mixing LiF and HCl, which is able to achieve the etching of MAX precursor and improve the safety of experimental operation simultaneously [65]. Nevertheless, it is extremely challenging to prepare MXenes with

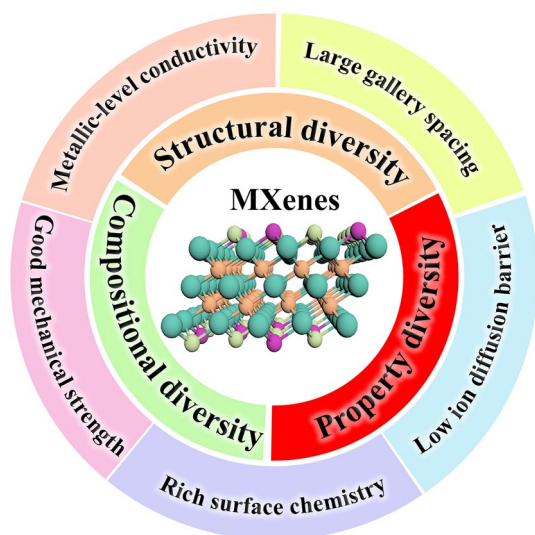


Fig. 2 Schematic illustration of the structural, compositional and property diversity of MXenes

uniform surface terminations by HF or LiF/HCl etching. Very recently, ZnCl_2 Lewis acidic salt was employed to etch Ti_3AlC_2 MAX, which was based on the replacement reaction between Zn^{2+} cations and zero-valence Al of Ti_3AlC_2 MAX, finally leading to Zn metal-decorated multi-layered $\text{Ti}_3\text{C}_2\text{Cl}_2$ MXene [66]. This strategy was further developed into a general route by using various Lewis acidic molten salts etchants to synthesize MXenes [67]. Compared with HF or LiF/HCl etching, Lewis acidic molten salts etching strategy demonstrates a series of advantages, such as greatly enhanced safety because of avoiding the direct or indirect use of hazardous HF, great universality to etch non-Al MAX precursors, the ability to endow MXenes with controllable surface terminations, easy accessibility to in-situ formed metals-modified MXenes and the potential for large-scale application.

The Lewis acidic molten salts etching approach has received considerable attention since 2019 [66, 67], which can be proved by the increasing article numbers (Fig. 3a). In summary, the MXenes and MXene-based composites prepared by Lewis acidic etching route have been applied by researchers from different fields, and significant progress has been achieved in the development of Lewis acidic etching (Fig. 3b–c), showing great utilization potential. Therefore, it is highly required to summarize these advances timely. Nevertheless, to the best of our knowledge, there has been no review discussing the research progress of Lewis acidic

molten salts etching approach. Herein, we systematically summarize the recent advances of Lewis acidic etching strategy. First, we briefly introduce the traditional synthesis techniques of MXenes based on non-Lewis acidic etching route, mainly including HF etching, in-situ HF etching, bifluoride salts etching, electrochemical etching, alkali etching, common molten salts etching, etc. Then, Lewis acidic etching strategy are mainly presented from the following four aspects: etching mechanism, terminations regulation, in-situ formed metals and delamination of multi-layered MXenes (Fig. 4). Subsequently, the applications of MXenes and MXene-based composites produced by Lewis acidic molten salts etching route in energy storage and conversion, sensors and microwave absorption have been comprehensively discussed. Finally, we also propose some perspectives for the challenges and opportunities of Lewis acidic etching. This review aims to provide some help in the future development of Lewis acidic molten salts etching strategy and enable more researchers to fully understand this emerging method, thereby promoting its widespread utilization.

2 MXene Synthesis: Non-Lewis Acidic Etching Methods

2.1 HF Etching

It is well known that graphene can be obtained by mechanical exfoliation of graphite because there is only weak van der Waals interaction between the layers [68, 69]. However, the metallic bond between M and A atoms in MAX precursors is stronger than van der Waals force, which makes it impossible to obtain MXenes via mechanical stripping of MAX precursors [21, 26]. Therefore, researchers have to explore other methods to prepare MXenes. In 2011, Gogotsi and Naguib et al. immersed Ti_3AlC_2 MAX precursor in HF aqueous solution at room temperature and the Al layers can be selectively removed owing to the large difference between Ti–C and Ti–Al bond strength, thus leading to the successful preparation of multi-layered $\text{Ti}_3\text{C}_2\text{T}_x$ MXene with obvious accordion-like morphology (Fig. 5a–b) [11, 70–72]. For the HF etchant, H^+ cations serve as oxidant and F^- anions act as ligand to combine with by-product of the reaction. The etching process is presented as follows:



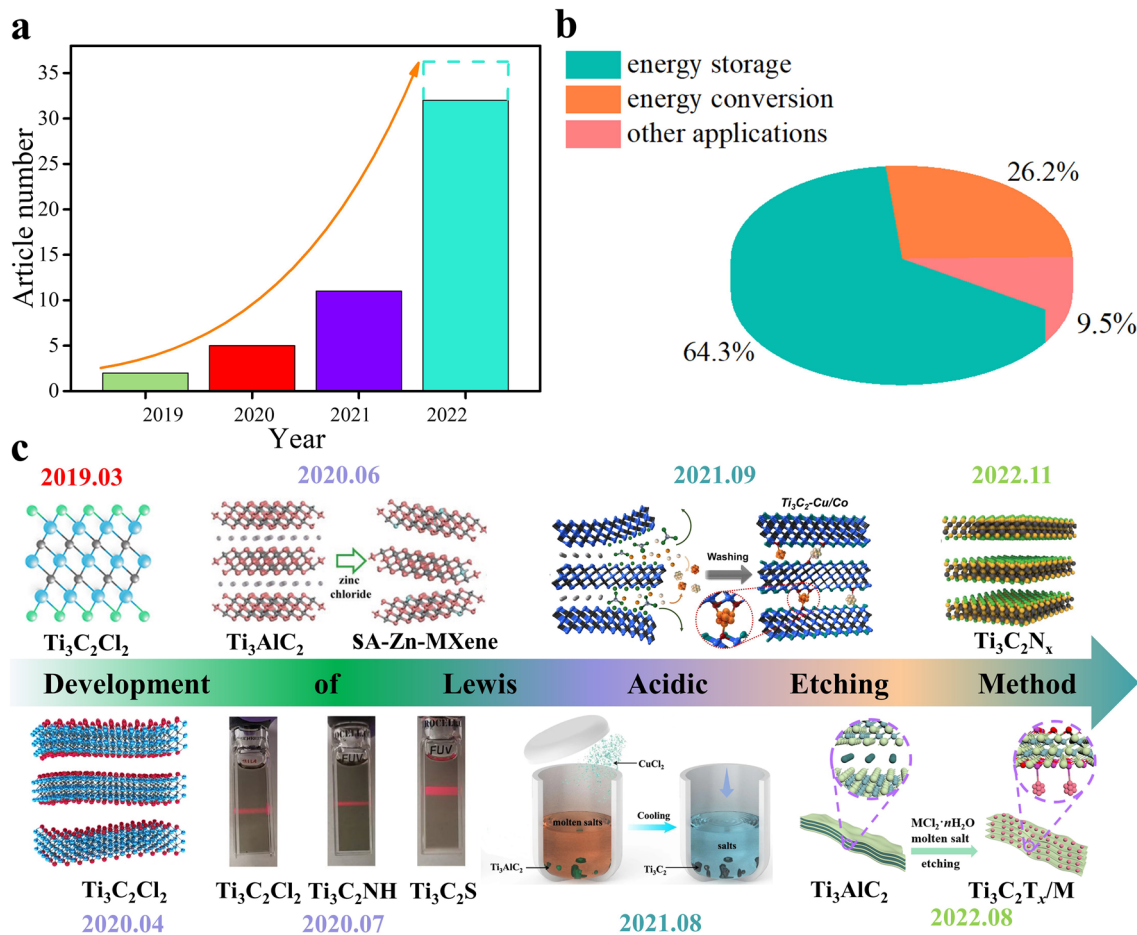
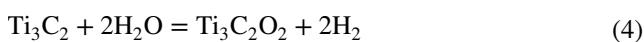
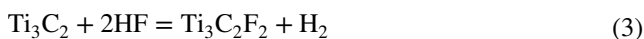
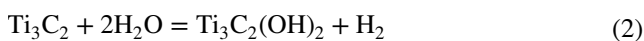


Fig. 3 **a** Annual publications of Lewis acidic etching method. **b** Application ratio of MXenes and MXene-based composites prepared by Lewis acidic etching route in different fields. **c** A timeline showing the development progress of Lewis acidic etching route. Image published in 2019.03: Reproduced with permission from [66] Copyright 2019, American Chemical Society. Image published in 2020.04: Reproduced with permission from [67] Copyright 2020, The Authors, published by Springer Nature. Image published in 2020.06: Reproduced with permission from [157] Copyright 2020, Wiley–VCH. Image published in 2020.07: Reproduced with permission from [42] Copyright 2020, The American Association for the Advancement of Science. Image published in 2021.08: Reproduced with permission from [112] Copyright 2021, The Authors, published by Springer Nature. Image published in 2021.09: Reproduced with permission from [122] Copyright 2021, Wiley–VCH. Image published in 2022.08: Reproduced with permission from [147] Copyright 2022, Wiley–VCH. Image published in 2022.11: Reproduced with permission from [126] Copyright 2022, The Authors, published by Wiley–VCH



Specifically, the almost zero-valence Al atoms in Ti₃AlC₂ precursor lose electrons to become Al³⁺ cations and then combine with F⁻ anions ligand to form soluble AlF₃ [70, 71]. Simultaneously, the multi-layered Ti₃C₂ MXene is generally modified with –O, –OH and –F groups

based on Eqs. (2–4). The introduction of surface functional groups results in the shift of (002) peak to lower angle, which can effectively confirm the successful preparation of MXenes [70, 73]. Since then, a series of MXenes such as Ti₂CT_x, Nb₂CT_x, V₂CT_x, Ti₃CNT_x and Nb₄C₃T_x have been successfully prepared by HF etching [13, 74–77]. Additionally, the obtained multi-layered MXenes can be intercalated by large organic molecules such as dimethyl sulfoxide (DMSO), urea, tetramethylammonium hydroxide (TMAOH), isopropanol (IPA), isopropyl amine (i-PrA), tetrabutylammonium hydroxide (TBAOH), which further expands the gallery spacing and weakens the interlayer

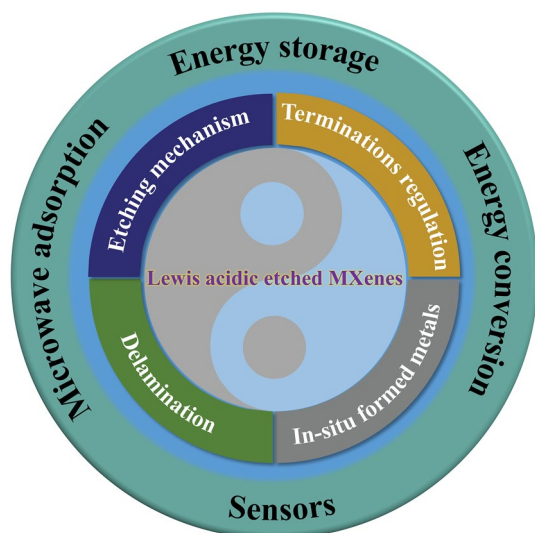


Fig. 4 An overview demonstrating the Lewis acidic etching method

interaction [78–81], finally enabling the multi-layered MXenes to be delaminated into few-layered or single-layered MXenes (Fig. 5c) [82].

MAX precursors with different M-site atoms, A-site atoms, X-site atoms and n values usually require different HF concentration, etching time and reaction temperature. Generally, Mo-based and Nb-based MAX require higher HF concentration than Ti-based MAX to prepare corresponding MXenes [83, 84]. In addition, the etching of Si-based MAX including Ti_3SiC_2 requires HF and other strong oxidants (H_2O_2 , KMnO_4 , etc.) to complete together [85]. Besides, compared with carbide MXenes, nitride MXenes require more precise adjustment of etching parameters during the preparation process, because the M–N bond may be broken under the attack of HF etchant [57]. However, harsh reaction environment could result in the formation of defects, such as Ti vacancy, which can adversely affect the electronic conductivity of MXenes [86]. Furthermore, some non-MAX precursors such as $\text{Zr}_3\text{Al}_3\text{C}_5$, $\text{Hf}_3\text{Al}_4\text{C}_6$ and $\text{Mo}_2\text{Ga}_2\text{C}$ can also be etched by HF to obtain $\text{Zr}_3\text{C}_2\text{T}_x$, $\text{Hf}_3\text{C}_2\text{T}_x$ and Mo_2CT_x MXene, respectively, which greatly expands the scope of precursors and is of great significance to the development of MXenes [18–20]. In general, HF etching method with excellent universality plays a crucial role in the rapid development of MXenes and some researchers still adopt this approach to prepare MXenes until now. Nevertheless, the strong corrosiveness of HF greatly increases the experimental risk and deteriorates its industrialization

prospect. The development of a greener, safer and milder etchant is still the focus in the field of MXenes.

2.2 In-Situ HF Etching

In 2014, a relatively safe etching route by mixing HCl and LiF was proposed by Ghidui et al. to prepare $\text{Ti}_3\text{C}_2\text{T}_x$ MXene [65]. In this approach, HF can be in-situ generated to initiate the etching process based on Eq. (5) and Li^+ cations spontaneously intercalate into the interlayer of $\text{Ti}_3\text{C}_2\text{T}_x$ MXene.



The c -lattice parameter of MXenes obtained by LiF/HCl etching is greatly larger than that of MXenes prepared by HF etching, which is mainly owing to the intercalation of Li^+ cations and water molecules. Benefiting from the hydrophilic nature, the prepared $\text{Ti}_3\text{C}_2\text{T}_x$ MXene demonstrates clay-like behavior and can be processed into different desired shapes such as rolled film. Additionally, clay-like $\text{Ti}_3\text{C}_2\text{T}_x$ MXene can be shaped into the letter “M” and exhibit a high electrical conductivity of 1500 S cm^{-1} . More importantly, thanks to the insertion of Li^+ ions and water, the van der Waals forces between the layers are weakened and multi-layered MXenes can be directly centrifuged after sonication to obtain few-layered MXenes. It is worth mentioning that the molar ratio of LiF and Ti_3AlC_2 MAX has a great influence on the lateral size of the final $\text{Ti}_3\text{C}_2\text{T}_x$ MXene, and higher LiF concentration favors the complete etching of Ti_3AlC_2 MAX and intercalation of more Li^+ ions into the MXene interlayers.

Therefore, in-situ HF etching is further upgraded to the “minimally intensive layer delamination” (MILD) method in 2017 by increasing the molar ratio of LiF and Ti_3AlC_2 MAX to 7.5:1.0, which can achieve the delamination of multi-layered MXenes via simple hand-shaking process rather than ultrasonication [87]. The obtained $\text{Ti}_3\text{C}_2\text{T}_x$ MXene nanosheets demonstrate large lateral size and high quality, resulting in a high electronic conductivity of $4600 \pm 1100 \text{ S cm}^{-1}$. So far, other fluoride salts including NaF, KF, FeF_3 , etc., and acids such as H_2SO_4 have also been used by researchers [88–91]. For example, Soundiraraju et al. reported the successful preparation of Ti_2NT_x MXene by immersing Ti_2AlN MAX in a mixture of KF and HCl [89]. Generally, the in-situ HF etching method based on LiF/HCl etchant has appeared the most in

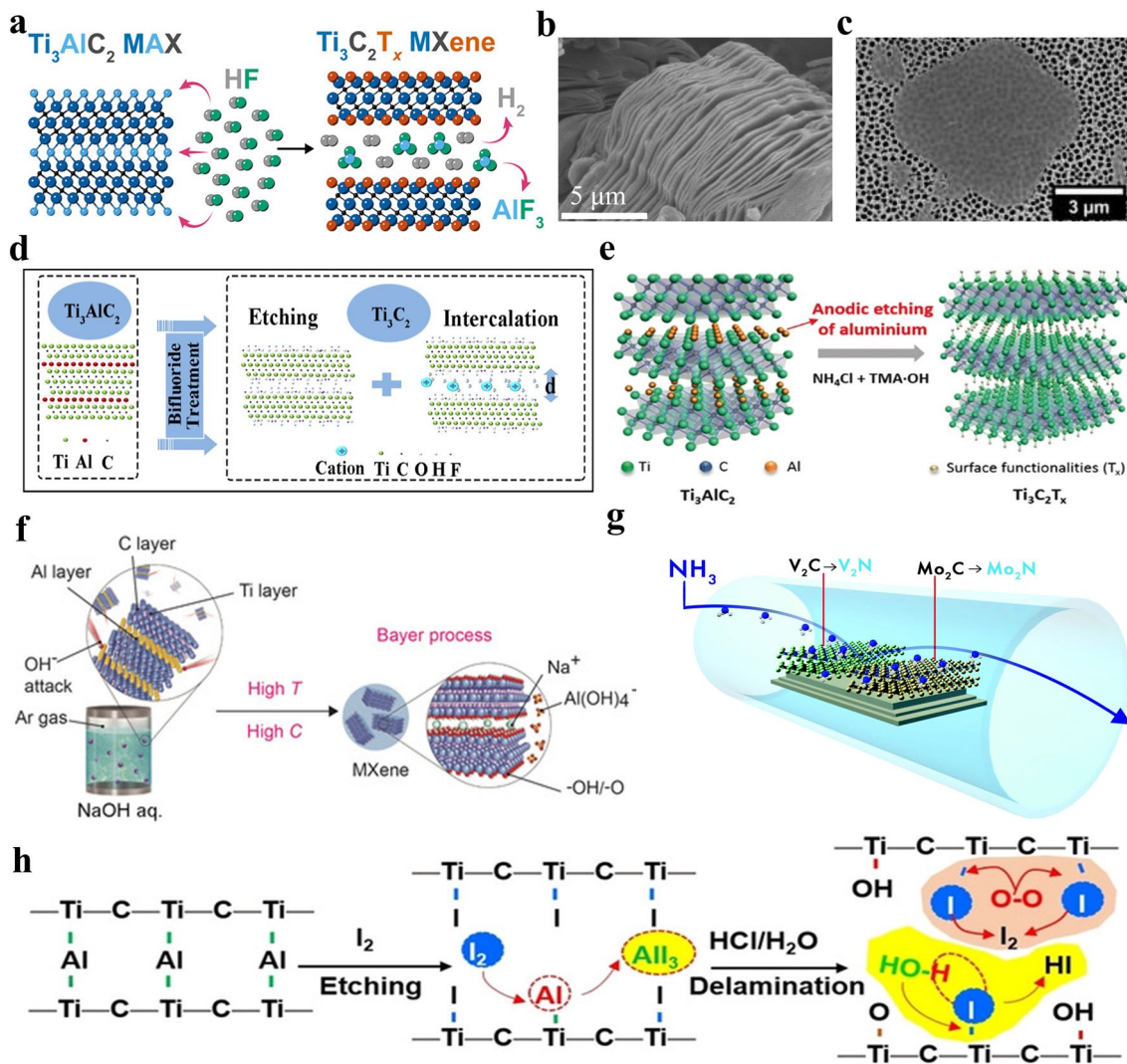


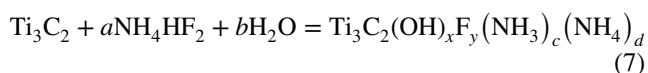
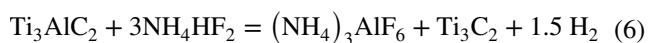
Fig. 5 **a** Schematic showing the preparation of multi-layered $Ti_3C_2T_x$ MXene by HF etching. Reproduced with permission from [70] Copyright 2022, American Chemical Society. **b** SEM image of multi-layered $Ti_3C_2T_x$ MXene. Reproduced with permission from [72] Copyright 2020, Springer Nature. **c** SEM image of single-layered $Ti_3C_2T_x$ MXene. Reproduced with permission from [82] Copyright 2021, American Chemical Society. **d** Schematic exhibiting the reaction mechanism between Ti_3AlC_2 MAX and bifluorides. Reproduced with permission from [93] Copyright 2016, Elsevier. **e** Schematic of the electrochemical etching of Ti_3AlC_2 MAX in a binary aqueous electrolyte. Reproduced with permission from [98] Copyright 2018, Wiley–VCH. **f** Schematic of synthesis of $Ti_3C_2T_x$ MXene by NaOH-assisted hydrothermal method. Reproduced with permission from [101] Copyright 2018, Wiley–VCH. **g** Synthesis of Mo_2N and V_2N MXene via ammoniation strategy. Reproduced with permission from [105] Copyright 2017, Royal Society of Chemistry. **h** Schematic diagram showing the preparation of $Ti_3C_2T_x$ MXene via iodine-assisted etching. Reproduced with permission from [108] Copyright 2021, The Authors, published by Wiley–VCH

the recently published articles on MXenes. The biggest advantage of in-situ HF etching route is the improvement of experimental safety and the ability to prepare MXenes nanosheets with larger lateral sizes and fewer defects. However, cations (Li^+ , Na^+ , K^+ , etc.) will intercalate into MXenes interlayers

during the preparation process and it is difficult to eliminate them from MXenes, which may have an adverse impact on the further application of MXenes in some fields. The relationship between structure and properties should be further investigated.

2.3 Bifluoride Salts Etching

In 2014, bifluoride NH_4HF_2 was used to etch the Ti_3AlC_2 MAX precursor to obtain $\text{Ti}_3\text{C}_2\text{T}_x$ MXene [92]. The reaction mechanism is summarized as follows:

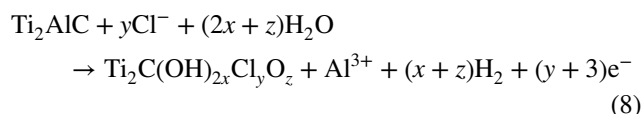


In this method, the selective etching of Al layers from Ti_3AlC_2 MAX and the intercalation of NH_3 and NH_4^+ into the interlayer of $\text{Ti}_3\text{C}_2\text{T}_x$ MXene occur simultaneously. The intercalation of ammonium species effectively increases the interlayer spacing. Further, NaHF_2 and KHF_2 were also utilized as etchants to prepare $\text{Ti}_3\text{C}_2\text{T}_x$ MXene by Feng et al. in 2017 and the etching mechanisms are similar to that of NH_4HF_2 [93] (Fig. 5d). In 2020, Natu et al. used NH_4HF_2 to etch Ti_3AlC_2 MAX with polar organic solvents as the reaction medium instead of water, successfully realizing the water-free synthesis of $\text{Ti}_3\text{C}_2\text{T}_x$ MXene [94]. The NH_4HF_2 can be decomposed into HF and NH_4F , and HF plays the role of etching the Al atomic layers. It is noteworthy that the as-prepared $\text{Ti}_3\text{C}_2\text{T}_x$ MXene is highly fluorinated and the ammonium cations surrounded by organic solvent molecules can intercalate into the layers, which endows MXene with the largest interlayer spacing of 5.07 nm up to now. Overall, the bifluoride salts etching is safer relative to HF etching. However, bifluoride salts are currently only used to etch Ti_3AlC_2 MAX and the universality of the method requires to be further improved.

2.4 Electrochemical Etching

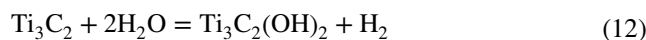
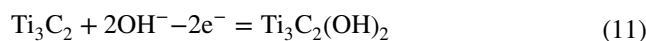
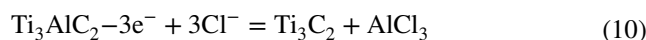
During the etching process of MAX precursors by using the three methods mentioned above, the researchers may be directly or indirectly exposed to hazardous HF, which reduces the safety of the experimental process. Moreover, high content of -F surface group may reduce the electronic conductivity of obtained MXenes and block ion transport, which is not conducive to their application in metal-ion batteries [59]. Therefore, it is urgent to explore fluorine-free etching method. In 2014, Gogotsi et al. removed M-atom and A-atom layers from Ti_3AlC_2 , Ti_2AlC and Ti_3SiC_2 MAX precursors to prepare carbide-derived carbons via electrochemical etching approach [95]. In 2015, Zhao et al. selectively extracted Ti atom layers

from Ti_2SC MAX to obtain carbon/sulfur nanolaminates through electrochemical etching [96]. It can be observed that the above two works failed to obtain MXenes by electrochemical etching method. In 2017, Sun et al. firstly synthesized Ti_2CT_x MXene without -F termination in diluted HCl aqueous electrolyte at 0.6 V for 5 days via electrochemical etching [97], and the mechanism can be exhibited as follows:



At first, only the surface of Ti_2AlC MAX that is in contact with the electrolyte can be etched and the generated Ti_2CT_x MXene is coated on the surface of MAX, which prevents electrolyte from entering the interior and makes it difficult for the inner MAX to be further etched. Subsequently, the Ti_2CT_x MXene on the surface will be transformed into a carbon layer. Finally, a three-layered structure including carbide-derived carbon, Ti_2CT_x MXene and unetched Ti_2AlC MAX are obtained, thus leading to a low yield of MXenes. Some key parameters such as electrolyte concentration, etching potential and time have been proven to have a direct impact on the final etching products.

In 2018, Feng et al. prepared $\text{Ti}_3\text{C}_2\text{T}_x$ MXene with a large lateral size of 18.6 μm in a binary aqueous electrolyte containing NH_4Cl and TMAOH (Fig. 5e) [98]. In this method, the weak Ti–Al bond is broken and then Al^{3+} cations combine with Cl^- anions to form AlCl_3 . The obtained Ti_3C_2 can be terminated by -OH group and the etching process is illustrated as follows:

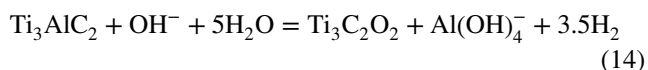
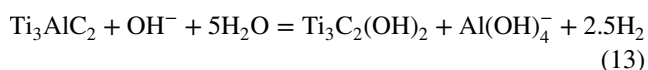


It is noteworthy that the intercalation of ammonium species and TMAOH can expand the interlayer spacing of $\text{Ti}_3\text{C}_2\text{T}_x$ MXene and expose more active sites, greatly promoting the etching of inner MAX phase and thus resulting in a relatively high etching yield of at least 60%. Later, a general strategy based on thermal-assisted electrochemical etching route was proposed by Hao's group to synthesize various MXene (Ti_2CT_x , Cr_2CT_x and V_2CT_x) [99]. In this approach, 1 M HCl solution is chosen as electrolyte and the heating facilitates

the etching of MAX precursor. Specifically, when the etching time and temperature is increased to 9 h and 50 °C, respectively, the obvious accordion-like morphology can be observed for Ti_2CT_x MXene. In general, the electrochemical etching enables the preparation of fluorine-free MXenes for the first time and is safer and milder than conventional HF etching method. However, over-etching and low etching yield are unavoidable issues, which greatly hinders the large-scale utilization of electrochemical etching method.

2.5 Alkali Etching

In addition to acids, alkalis can also be utilized to selectively etch MAX precursors. The earliest attempt to prepare MXenes via alkali etching was to immerse Ti_3AlC_2 MAX in dilute aqueous NaOH solution at 80 °C by Xie et al. in 2014 [100]. However, only the outermost MAX can be etched owing to the low NaOH concentration. Further, Zhang et al. proposed a NaOH-assisted hydrothermal process in 2018 to prepare $Ti_3C_2T_x$ MXene with a high yield of 92% (Fig. 5f) [101]. In this method, the OH^- anions attack Al-atom layers in Ti_3AlC_2 MAX to form Al (oxide) hydroxides, which can further dissolve in alkali solution as soluble $Al(OH)_4^-$ anions. It is noteworthy that high reaction temperature (270 °C) and NaOH concentration (27.5 M) can greatly speed up the whole process and promote complete etching of Ti_3AlC_2 MAX. The etching process can be described as follows:



It is worth mentioning that special attention should be paid to controlling reaction condition when MXene is prepared by alkali etching method. A recent work by our group found that $Ti_3C_2T_x$ MXene can be completely converted to $K_2Ti_8O_{17}$ nanowires after immersed in 5 M KOH solution at 50 °C for 10 days [102]. The reaction mechanism can be described as follows: The Ti-C bond in $Ti_3C_2T_x$ MXene is easily destroyed in the concentrated alkali environment and MXene is oxidized into titanium oxide nanoparticles, and the titanium oxide nanoparticles can then react with KOH to generate the final $K_2Ti_8O_{17}$ nanowires. Accordingly, the stability of various MXenes in concentrated alkali solution deserves further investigation. In general, although MXenes with abundant -O and -OH functional groups can be prepared via alkali etching route, harsh reaction condition

greatly increases the experimental risk, which makes alkali etching unsuitable for large-scale preparation of MXenes.

2.6 Common Molten Salts Etching

The above-mentioned methods for preparing MXenes are all based on the wet chemical etching route. However, Gogotsi et al. reported molten salts etching method to prepare $Ti_4N_3T_x$ MXene in 2016, which opens the door to the preparation of MXenes via dry chemical etching techniques [103]. In this method, a mixture of LiF, NaF and KF is used to selectively etch Al-atom layers from Ti_4AlN_3 MAX precursor at 550 °C under Ar atmosphere to synthesize $Ti_4N_3T_x$ MXene, and the few-layered nanoflakes can be obtained by TBAOH intercalation and subsequent ultrasonication. It is worth mentioning that since the discovery of MXenes, $Ti_4N_3T_x$ is the first nitride MXene that has been experimentally synthesized. In 2021, Zong et al. reported the synthesis of Ti_2NT_x MXene by etching Ti_2AlN MAX precursor with the mixture of fluoride salt (KF, LiF, and NaF) in a molar ratio of 1:3 at 550 °C [104]. Up to now, the family of nitride MXenes only contains Ti_2N , Mo_2N , V_2N and Ti_4N_3 [89, 103, 105], which is mainly due to the difficulty in preparation. Firstly, the number of nitride MAX precursor is relatively limited due to the high formation energy. Then, M-A bond in nitride MAX exhibits high strength compared with that of carbide MAX, indicating that larger exfoliation energy is needed for nitride MAX. Finally, nitride MXene is prone to dissolve in HF solution and exhibits poor structural stability owing to the low cohesive energy [38, 71]. Therefore, great efforts should be made to explore the suitable etching route for nitride MAX. In general, molten salts etching, as the first method to prepare nitride MXenes, is of great significance. However, this method is only applicable to the preparation of $Ti_4N_3T_x$ and Ti_2NT_x MXene at present, and the obtained MXene exhibits high content of -F surface group. The above two key points greatly limit the development of common molten salts etching method.

2.7 Other Etching Methods

In addition to the etching methods described above, there are other methods that can also be used to prepare MXenes. In 2017, Gogotsi's group presented an ammoniation strategy

to transform Mo_2C and V_2C MXene to corresponding Mo_2N and V_2N at 600 °C by using NH_3 as nitrogen source (Fig. 5g) [105], which further enriches the family of nitride MXenes. It is worth mentioning that the obtained Mo_2N and V_2N MXene demonstrate higher room temperature electronic conductivity than their carbide counterparts. In 2020, Sun et al. successfully prepared mesoporous Mo_2C MXene via ultraviolet-driven etching of $\text{Mo}_2\text{Ga}_2\text{C}$ precursor, which avoids the utilization of hazardous HF and greatly improves the experimental safety [106]. They also presented thermal reduction strategy to synthesize Ti_2C MXene from Ti_2SC MAX. In this method, reductive gas such as H_2 can react with weakly-bonded S atoms, continuously accelerating the etching process [107]. In 2021, iodine-assisted etching route was developed by Feng et al. to synthesize $\text{Ti}_3\text{C}_2\text{T}_x$ MXene rich in -O terminations in anhydrous acetonitrile at 100 °C (Fig. 5h) [108]. Owing to the water-free etching process, $\text{Ti}_3\text{C}_2\text{T}_x$ MXene with an average lateral size of 1.8 μm exhibits superior structural integrity and can be stored stably in water for more than 2 weeks. Further, Jawaid et al. successfully prepared halogenated $\text{Ti}_3\text{C}_2\text{T}_x$ MXene under anhydrous environment by using halogens (Br_2 , I_2 , ICl , IBr) as etchants, and the halogen terminations may endow MXenes with some new properties [109]. Besides, ionic liquids such as 1-butyl-3-methylimidazolium hexafluorophosphate (BMIMPF_6) was utilized as etchant to prepare Ti_2CT_x MXene at 80 °C for 20 h [110]. The ionic liquids can intercalate into interlayers, leading to expanded interlayer spacing and the separation of layers.

Compared with above-mentioned top-down methods, the bottom-up approaches are usually able to synthesize defect-free 2D materials, which can also be utilized to obtain high-quality MXenes. In 2015, Ren et al. developed chemical vapor deposition method to fabricate large-area high-quality ultrathin $\alpha\text{-Mo}_2\text{C}$ nanosheets, which possess a thickness of few nanometers and a lateral size of around 100 μm [111]. Moreover, the prepared $\alpha\text{-Mo}_2\text{C}$ MXene exhibits superior stability under various environments including water, HCl or annealing at 200 °C in air. More importantly, this method reveals excellent generality and can also be used to construct WC and TaC crystals. In conclusion, many various methods have been proposed to prepare MXenes until now. However, each etching route has its own shortcomings and is unlikely for large-scale utilization in the future. As we all know, exploring a safe, green, non-hazardous, low-cost and easily scalable preparation method is the biggest challenge for the

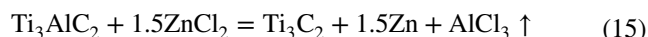
researchers in the fields of MXenes, which plays a crucial role in the development of MXenes in the next decades.

3 MXene Synthesis: Lewis Acidic Etching Method

In 2019, Huang's group proposed a brand-new, safe and green method, namely Lewis acidic molten salts etching, to prepare Cl-terminated MXene [66]. Owing to a series of advantages, Lewis acidic etching has attracted intensive attention since it was presented, greatly promoting the development of MXenes in the past three years. The introduction of Lewis acidic molten salts etching approach is mainly classified into following four aspects: etching mechanism, terminations regulation, in-situ formed metals and delamination of multi-layered MXenes.

3.1 Etching Mechanism

The mechanism of Lewis acidic molten salts etching method is based on the replacement reaction between Lewis acidic molten salts and A-site atoms in MAX precursor. Taking the etching of Ti_3AlC_2 MAX precursor by the firstly used Lewis acidic salt ZnCl_2 as an example, Huang et al. thoroughly mixed the Ti_3AlC_2 and ZnCl_2 with a molar ratio of 1:1.5 in a glovebox and the mixture was placed in alumina crucible, which is then heated at 550 °C for 5 h in a tube furnace under Ar atmosphere (Fig. 6a) [66]. It can be observed that main peaks of final product shift to lower angles relative to those of Ti_3AlC_2 MAX in the X-ray diffraction (XRD) patterns (Fig. 6b), revealing an enlarged lattice parameter. Additionally, the densely-packed structure can still be kept, and high-angle annular dark-field scanning transmission electron microscopy (HAADF-STEM) image in Fig. 6c suggests that interlayer element is brighter compared with other elements, thus proving that Ti_3ZnC_2 MAX has been successfully prepared. The specific formation mechanism can be described by Eqs. (15–16):



It is well-known that ZnCl_2 will exist in the form of molten state at 550 °C and is ionized into Zn^{2+} cations. Then, the Zn^{2+} with strong electron obtaining ability will react with Al atoms in Ti_3AlC_2 to generate Al^{3+} cations and Zn atoms. Al^{3+} cations are prone to combine with Cl^- anions to form AlCl_3 , which will evaporate at 178 °C. At the same time, Zn

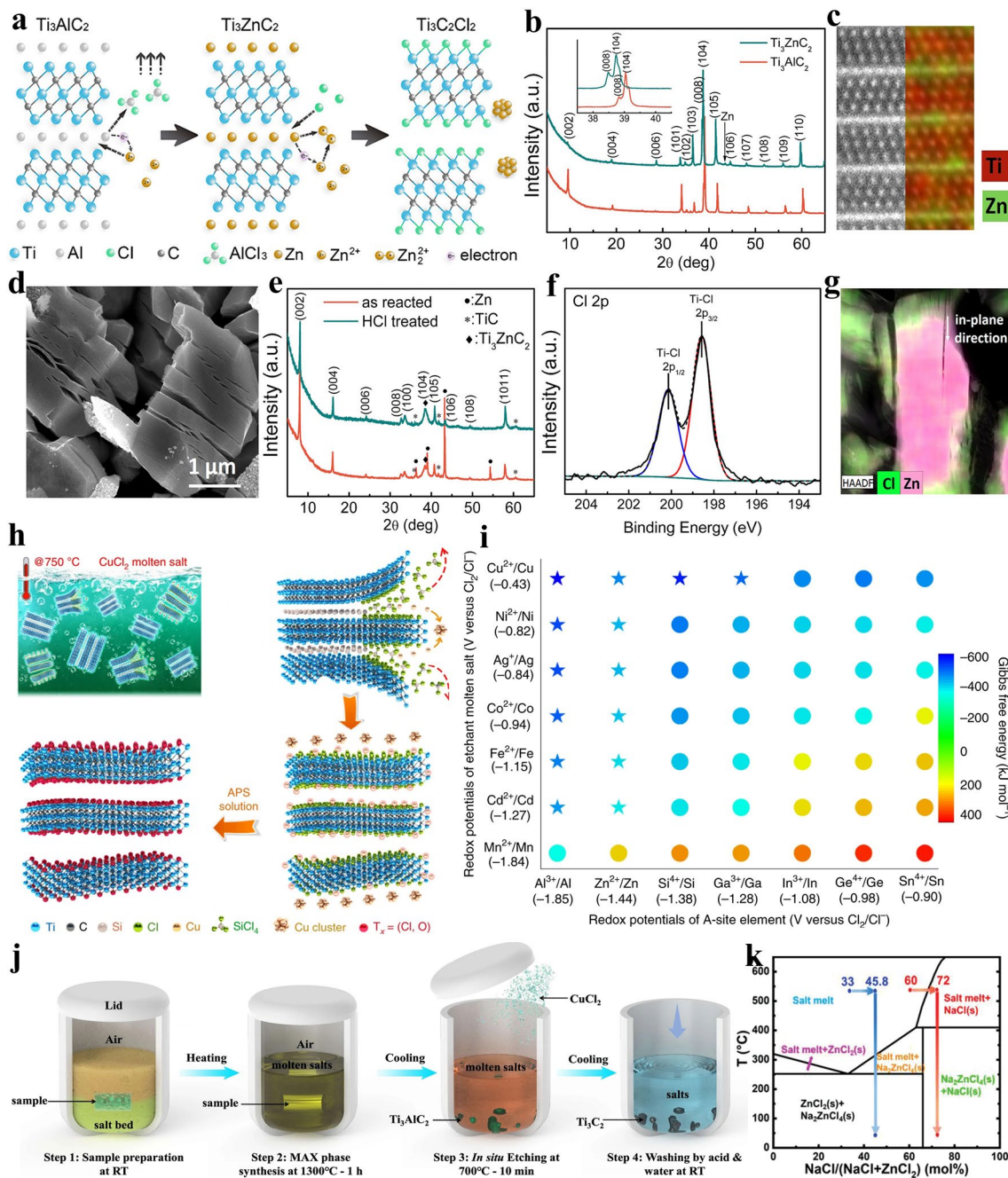
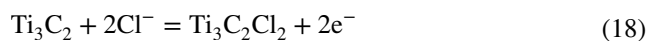
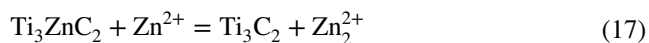


Fig. 6 **a** Schematic showing the preparation of $Ti_3C_2Cl_2$ MXene by $ZnCl_2$ Lewis acidic salt etching. **b** XRD patterns of Ti_3AlC_2 and Ti_3ZnC_2 MAX. **c** HAADF-STEM image of Ti_3ZnC_2 MAX and corresponding energy-dispersive spectroscopy (EDS) mapping. **d** SEM image of multi-layered $Ti_3C_2Cl_2$ MXene. **e** XRD patterns of $Ti_3C_2Cl_2$ MXene and $Ti_3C_2Cl_2/Zn$ hybrids. **f** Cl 2p XPS spectra of $Ti_3C_2Cl_2$ MXene. **g** EDS mapping analysis showing the Lewis acidic etching of Ti_3AlC_2 MAX. Reproduced with permission from [66] Copyright 2019, American Chemical Society. **h** Schematic demonstrating the preparation of $Ti_3C_2T_x$ MXene by $CuCl_2$ etching. **i** Schematic showing the relationship between redox potential of A-site elements, redox potential of Lewis acidic salts and Gibbs free energy. Reproduced with permission from [67] Copyright 2020, The Authors, published by Springer Nature. **j** Schematic illustration of the one-pot synthesis of $Ti_3C_2T_x$ MXene under air atmosphere. Reproduced with permission from [112] Copyright 2021, The Authors, published by Springer Nature. **k** Phase diagram of $NaCl/ZnCl_2$ mixture. Reproduced with permission from [113] Copyright 2021, Wiley-VCH

atoms can diffuse into the interlayer of Ti_3C_2 and occupy the position originally belonging to Al atoms, thereby leading to the generation of new MAX phase Ti_3ZnC_2 . It is worth mentioning that the removal of AlCl_3 from the system considerably accelerates the element replacement reaction.

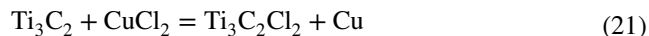
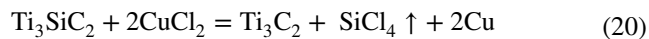
When the molar ratio of Ti_3AlC_2 and ZnCl_2 further increases to 1:6, Ti_3C_2 MXene with -Cl termination instead of Ti_3ZnC_2 MAX can be successfully obtained. Firstly, the classical multi-layered structure is observed for $\text{Ti}_3\text{C}_2\text{Cl}_2$ MXene (Fig. 6d). Then, the XRD pattern of as reacted product indicates that the strongest (104) peak at around 39° of Ti_3AlC_2 MAX almost vanishes and the (002) peak moves to a lower angle of 7.94° (Fig. 6e), suggesting an expanded interlayer spacing. Additionally, the characteristic XRD peaks of Zn metal can also be observed. Further, Ti-Cl chemical bond in $\text{Ti}_3\text{C}_2\text{Cl}_2$ MXene can be confirmed by Cl 2p X-ray photoelectron spectroscopy (XPS) spectra (Fig. 6f) [66]. Above discussions effectively confirm the formation of $\text{Ti}_3\text{C}_2\text{Cl}_2$ MXene and the reaction process can be described by following equations:



As exhibited in Fig. 6a, the formation of $\text{Ti}_3\text{C}_2\text{Cl}_2$ MXene can be divided into two stages including the initial formation of Ti_3ZnC_2 MAX shown in Eqs. (15–16) and the subsequent reaction of Ti_3ZnC_2 MAX with excessive ZnCl_2 to obtain $\text{Ti}_3\text{C}_2\text{Cl}_2$ exhibited in Eqs. (17–19). Specifically, the Zn atoms in Ti_3ZnC_2 MAX can be separated from interlayer and react with excessive Zn^{2+} to generate Zn_2^{2+} cations, and the Cl^- anions can easily intercalate into the interlayer of Ti_3C_2 , forming Ti-Cl chemical bond (Fig. 6g). Meanwhile, the Zn_2^{2+} cations gain electron to form Zn metal. In general, Zn^{2+} cations and Cl^- anions in ZnCl_2 act as H^+ and F^- in HF etchant, respectively.

Later in 2020, Prof. Huang and coworkers generalized the previously proposed Lewis acidic etching method, which greatly expands the family of Lewis acidic molten salts (FeCl_2 , CoCl_2 , NiCl_2 , CuCl_2 , CdCl_2 , CuI , CuBr_2 , etc.) and can prepare various MXenes from Al, Si and Ga-based MAX precursors [67]. They immersed Ti_3SiC_2 MAX in $\text{CuCl}_2/\text{NaCl}/\text{KCl}$ mixed molten salts at 750°C (Fig. 6h),

and NaCl and KCl play a role in providing molten salts environment. The etching process is illustrated as follows:



Specifically, the zero-valence Si atoms in the interlayer lose electrons to become Si^{4+} cations and then combine with Cl^- anions to form SiCl_4 , which can readily escape as gas at around 57°C . Subsequently, the Cu^{2+} cations can obtain electrons to transform into Cu metal. Finally, excessive Cl^- anions can be grafted onto exposed Ti atoms, resulting in the formation of $\text{Ti}_3\text{C}_2\text{Cl}_2$ MXene. It is worth mentioning that individual HF is difficult to etch Ti_3SiC_2 [85], while Lewis acidic salts can readily complete the above etching process, which reflects the superiority of Lewis acidic etching. After the etching process, NaCl, KCl and excessive CuCl_2 can be eliminated by washing the etching products with deionized water.

Further, Huang et al. proposed an effective criterion to determine whether the A-site atoms in MAX can react with metal ions in the Lewis acidic salts. They found that the metal ions in the Lewis acidic salts with high electrochemical redox potential can etch the MAX precursor with low redox potential A-site atoms. The relationship between redox potential of A-site elements, redox potential of Lewis acidic salts and Gibbs free energy is illustrated in Fig. 6i. For example, CuCl_2 molten salt can easily remove the Si atoms from Ti_3SiC_2 MAX as mentioned above, which is ascribed to the higher redox potential of Cu^{2+}/Cu pair (-0.43 V versus Cl_2/Cl^-) compared with that of Si^{4+}/Si pair (-1.38 V versus Cl_2/Cl^-). The general etching reaction between A-site elements in MAX phase and Lewis acidic molten salts MQ_y ($\text{Q}=\text{Cl}, \text{Br}$ or I) can be described as follows:



It can be inferred that the difficulty degree of etching $\text{M}_{n+1}\text{AX}_n$ precursors by Lewis acidic molten salts is independent of M, X and n values, and only depends on the redox potential of A-site element. Therefore, based on Lewis acidic etching criterion, a large number of MAX phases (Ti_3AlC_2 , Ti_3ZnC_2 , Ti_3SiC_2 , Ti_3AlCN , Ti_2GaC , Ti_2AlC , Ta_2AlC , Nb_2AlC , etc.) can be etched by using different Lewis acidic salts (FeCl_2 , CoCl_2 , NiCl_2 , CuCl_2 , CdCl_2 , AgCl , CuI , CuBr_2 , etc.).

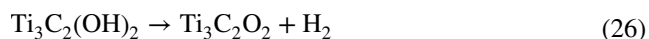
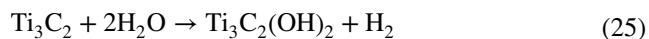
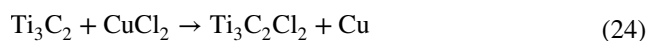
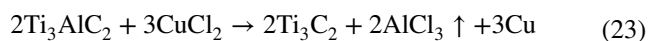
The reaction mechanism of Lewis acidic etching method is basically clear now, but the understanding of Lewis acidic

etching method can still be further deepened by optimizing etching parameters such as reaction atmosphere and etchant compositions. For example, in order to prevent the oxidation of the prepared MXenes, the inert gas such as Ar is generally used for protection in the process of Lewis acidic etching. However, Lin et al. proposed a simple one-pot synthesis method, containing molten salts shielded strategy for MAX preparation and subsequent in-situ Lewis acidic etching, to achieve the preparation of MXenes under air atmosphere (Fig. 6j) [112]. Specifically, they thoroughly mixed Ti, Al and C powders with NaCl and KCl salts, and the mixture was then pressed into a pellet. Subsequently, the pellet was further placed in a salt bed composed of NaCl and KCl which can melt at around 650 °C to insulate the air, and the Ti_3AlC_2 MAX can be obtained by heating at 1300 °C for 1 h in muffle furnace without Ar protection. Finally, CuCl_2 was introduced to the reaction system at 700 °C to achieve the in-situ etching of Ti_3AlC_2 MAX for 10 min, thus leading to the quick formation of Cl-terminated $\text{Ti}_3\text{C}_2\text{T}_x$ MXene. Therefore, with the assistance of the molten salts shielding strategy, Lewis acidic molten salts can directly etch MAX precursor in air atmosphere, which greatly promotes the development of Lewis acidic etching method. In addition, Zhang et al. demonstrated one-step eutectic etching strategy for the synthesis of in-plane porous $\text{Ti}_3\text{C}_2\text{Cl}_2$ MXene by regulating the etchant composition from ZnCl_2 to $\text{NaCl}/\text{ZnCl}_2$ mixture [113]. When ZnCl_2 is used to etch the MAX phase, the volatilization of generated AlCl_3 at high temperature will cause structural/crystal defects in the precursor, which will then evolve into void space. However, the generated pores will gradually collapse owing to the absence of temporary physical support during cooling process. Further, they found that when the etchant is changed into a mixture of ZnCl_2 and NaCl in a molar ratio of 4:6, the NaCl mole percent will gradually increase to 72% with the progress of etching process, which makes the salt melt shift across the phase boundary and leads to the precipitation of NaCl particles at 550 °C based on the phase diagram (Fig. 6k). The formation of NaCl particles can occupy void space to prevent the shrinkage and collapse of pores, finally resulting in a large increase in mesoporous volume and specific surface area. Therefore, the pore structure of the prepared MXenes can be greatly adjusted by the manipulation of etchant composition. The above-mentioned two works indicate that the Lewis acidic etching method still possesses broad development space and can be further improved from different aspects in the future.

3.2 Terminations Regulation

A large number of theoretical calculations and experiments have proved that the composition of surface groups can considerably influence the physical and chemical properties of MXenes, such as electronic property, mechanical property, magnetic property, optical property, chemical stability, dispersibility and redox activity [15, 26, 55, 61, 63, 114–116]. Therefore, in order to accurately explore that how surface functional groups affect the properties of MXenes, it is pretty important to synthesize MXenes with controllable surface chemistry. However, preparing MXenes with single and uniform surface groups has been a huge challenge for researchers. Taking HF etching as an example, MXenes exhibits mixed surface terminations including –O, –OH and –F [31, 43]. Firstly, the complex and uncontrollable surface termination greatly affect the properties of MXenes, which is not conducive to the management of experimental variables and the large-scale preparation of MXenes. Additionally, functional groups like –F can irreversibly react with Li^+ or Na^+ cations and block their transport, which negatively affects the electrochemical performance of MXenes electrodes [117, 118]. Therefore, preparing MXenes with fluorine-free surface groups should be the best choice for researchers in the fields of lithium-ion batteries (LIBs) or sodium-ion batteries (SIBs). However, it is difficult to obtain MXenes with homogeneous and fluorine-free terminations before 2019. Fortunately, the fabrication of MXenes with totally controllable surface chemistry is realized by the propose of Lewis acidic molten salts etching strategy. The functional groups of MXenes prepared by Lewis acidic etching mainly depends on the Lewis acidic salts anions. For example, Ti_3C_2 MXene terminated by –Cl functional group can be synthesized by Cl^- anions-containing Lewis acidic salts etching. However, a small part of –Cl terminations may be replaced by –O groups during the washing process, and the content of –O surface group mainly depends on the competition between –O and –Cl terminations [67, 119]. Lin et al. proved that –O surface group in Nb_2C MXene prepared by CuCl_2 etching demonstrates stronger competitiveness compared with –Cl surface groups, thus leading to Nb_2CT_x MXene rich in –O termination, while the competition between –O and –Cl for Ti_3C_2 MXene is relatively weak [119]. Since the –O functional groups are conducive to the electrochemical process of metal-ion batteries and SCs [120, 121], it is necessary to further increase the content

of –O termination in $\text{Ti}_3\text{C}_2\text{T}_x$ MXene. Pang et al. etched Ti_3AlC_2 by $\text{CuCl}_2 \cdot 2\text{H}_2\text{O}$ or $\text{CoCl}_2 \cdot 6\text{H}_2\text{O}$ Lewis acidic salts [122], the additional introduction of six water molecules can effectively raise the number of –O functional groups and the etching process can be described as follows:



Due to the wide variety of halogen elements in the Lewis acidic molten salts, MXene can also be terminated by other halogen anions. For example, Ti_3C_2 MXene with –Br or –I functional groups can be obtained via CuBr_2 or CuI etching, respectively (Fig. 7a–b). Further, Ti_3C_2 MXene can be endowed with –BrI, –ClI and –ClBr binary terminals as well as –ClBrI ternary halogen terminations. It is gratifying to note that Ti_3C_2 MXene with –Cl, –Br or –I functional groups all exhibit metallic-level conductivity (Fig. 7c), while F or OH-terminated Ti_3C_2 MXene often demonstrates semiconductor behavior [11, 66, 123, 124]. More importantly, due to the strong electrochemical reactivity, Br or I-terminated Ti_3C_2 MXene demonstrates excellent zinc storage performance. However, Ti_3C_2 MXene with –O, –F, –OH and –Cl functional groups exhibit low discharge specific capacity and oblique charge discharge curve when used as cathode for zinc-ion batteries (ZIBs) [123]. The above discussion reveals that the electrochemical performance of MXene electrodes can be greatly enhanced by adjusting the type of functional groups. Additionally, the halogen terminations of MXenes can be used as halogen sources and nucleation sites to prepare MXene/halide heterostructures. For example, Cui et al. synthesized intimate contact $\text{Bi}_{12}\text{O}_{17}\text{Cl}_2/\text{Ti}_3\text{C}_2$ MXene 2D/2D heterojunctions by the in-situ growth of $\text{Bi}_{12}\text{O}_{17}\text{Cl}_2$ nanosheets on the surface of Cl-terminated Ti_3C_2 MXene that was obtained via CuCl_2 etching [125].

Since the bond dissociation energies of Ti–Br and Ti–Cl bond are smaller than that of Ti–O, Ti–OH and Ti–F bonds [126], it is possible to chemically modify the surface of MXenes originally terminated with –Br or –Cl functional groups at a relatively low temperature. Based on this point, Kamysbayev et al. proposed a universal strategy to successfully prepare O, S, Se, Te and NH-terminated

Ti_3C_2 MXene and non-terminated Ti_3C_2 via Lewis acidic etching and subsequent termination substitution/elimination reactions in molten inorganic salts (Fig. 7d) [42]. Firstly, $\text{Ti}_3\text{C}_2\text{Br}_2$ MXene was prepared by mixing Ti_3AlC_2 MAX with CdBr_2 Lewis acidic salt. As followed, $\text{Ti}_3\text{C}_2\text{Br}_2$ MXene was dispersed in CsBr/KBr/LiBr eutectic salt at 300 °C and then reacted with NaNH_2 , Li_2O , Li_2S , Li_2Se or Li_2Te at around 500–600 °C in an Ar-filled glove box to synthesize $\text{Ti}_3\text{C}_2(\text{NH})$, $\text{Ti}_3\text{C}_2\text{O}$, $\text{Ti}_3\text{C}_2\text{S}$, $\text{Ti}_3\text{C}_2\text{Se}$, $\text{Ti}_3\text{C}_2\text{Te}$ MXene, respectively. Moreover, when treated with LiH at 300 °C, the surface groups of $\text{Ti}_3\text{C}_2\text{Br}_2$ MXene can be completely eliminated, thus leading to the formation of bare Ti_3C_2 MXene. This strategy realizes the controllable chemical transformation of functional groups for the first time. The surface groups can significantly regulate the interatomic spacings of MXenes lattice and their electronic properties. For example, the $\text{Ti}_3\text{C}_2\text{Te}$ lattice exhibits a greater in-plane lattice expansion (18%) (Fig. 7e). More importantly, Cl, S and Se-terminated Nb_2C MXene prepared by the above-mentioned strategy exhibits unprecedented superconductivity behavior (Fig. 7f), while Nb_2C MXene with –F and –O terminations synthesized by HF etching fails to demonstrate superconducting state, which is also proved by theoretical calculations [62]. The discovery of superconductivity phenomenon is mainly attributed to the influence of functional groups including –Cl, –S and –Se on MXenes structure, such as lattice strain, carrier localization, phonon frequency, and electron–phonon coupling [127], which greatly promotes the research of MXenes in the field of physics.

Very recently, Zhang et al. reported the synthesis of $\text{Ti}_3\text{C}_2\text{Br}_x$ MXene through CuCl_2 etching of Ti_3AlC_2 precursor and subsequent termination substitution in $\text{AlBr}_3/\text{NaBr}/\text{KBr}$ eutectic molten salts [128]. When the molar ratio of AlBr_3 is lower than 50%, the $\text{AlBr}_3/\text{NaBr}/\text{KBr}$ molten system with plenty of naked Na^+ , K^+ and Br^- demonstrates strong Lewis basicity. The Na^+ and K^+ cations can intercalate into the interlayer of MXene and the previous –Cl termination can be replaced by the Br^- anions via nucleophilic reaction, which simultaneously achieves the increase of interlayer spacing and the substitution of surface groups. The enlarged interlayer spacing leads to an expanded multi-layered morphology of $\text{Ti}_3\text{C}_2\text{Br}_x$ MXene, which may be conducive to the following delamination process to obtain few-layered nanosheets. In addition, Liu et al. synthesized N-containing $\text{Ti}_3\text{C}_2\text{T}_x$ MXene via FeCl_2

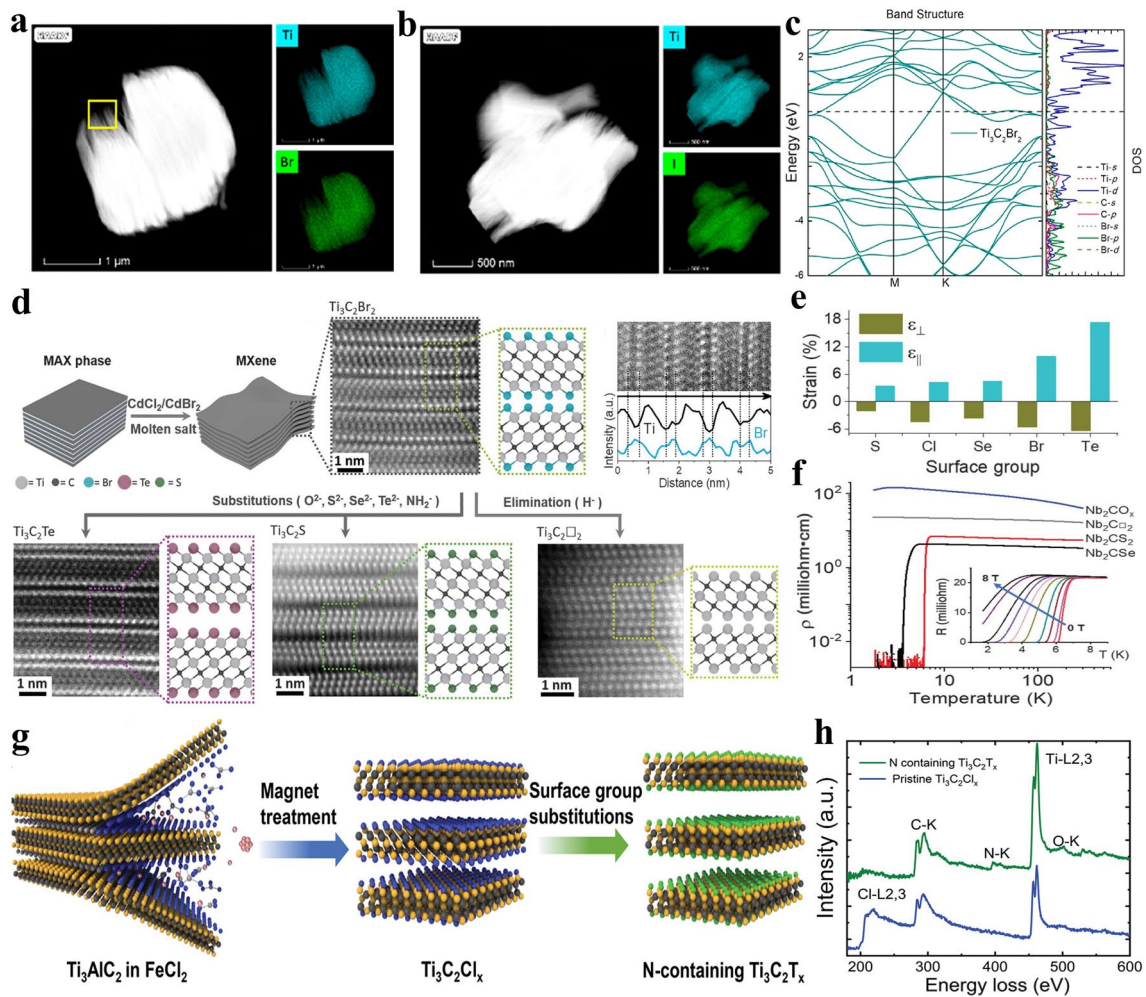


Fig. 7 **a–b** HAADF-STEM images and corresponding EDS mapping of $\text{Ti}_3\text{C}_2\text{Br}_2$ and $\text{Ti}_3\text{C}_2\text{I}_2$ MXene, respectively. **c** Electronic structure of $\text{Ti}_3\text{C}_2\text{Br}_2$ MXene. Reproduced with permission from [123] Copyright 2021, American Chemical Society. **d** Schematic showing the preparation of $\text{Ti}_3\text{C}_2\text{Tx}$ MXene via Lewis acidic etching and subsequent termination substitution in molten inorganic salts as well as corresponding HAADF-STEM images and EDS analysis. **e** Biaxial straining of $\text{Ti}_3\text{C}_2\text{Tx}$ MXene lattice induced by the terminations. **f** Temperature-dependent resistivity of Nb_2CT_x MXenes. Reproduced with permission from [42] Copyright 2020, The American Association for the Advancement of Science. **g** Schematic of the preparation of N-containing $\text{Ti}_3\text{C}_2\text{Tx}$ MXene via FeCl_2 Lewis acidic salt etching. **h** EELS analysis of pristine $\text{Ti}_3\text{C}_2\text{Tx}$ and N-containing $\text{Ti}_3\text{C}_2\text{Tx}$ MXene. Reproduced with permission from [126] Copyright 2022, The Authors, published by Wiley-VCH

Lewis acidic etching, subsequent magnet cleaning and final thermal treatment in $\text{Li}_3\text{N}/\text{LiCl}/\text{KCl}$ molten salts (Fig. 7g) [126]. The magnet cleaning process can not only effectively remove Fe nanoparticles, but also prevent the $-\text{Cl}$ surface group from being largely replaced by $-\text{O}$, which is beneficial for following termination substitution reaction. The dramatic decrease in Cl L2,3-edge intensity and appearance of N-K edge in electron energy-loss spectroscopy (EELS) confirm that the $-\text{Cl}$ functional groups can be transformed to $-\text{N}$ terminations in $\text{Li}_3\text{N}/\text{LiCl}/\text{KCl}$ Lewis basic molten salts (Fig. 7h), thus leading to the N-containing $\text{Ti}_3\text{C}_2\text{Tx}$ MXene.

In short, combined with Lewis acidic etching, termination exchange reactions in Lewis basic molten salts medium can endow MXenes with unconventional terminations, which have never appeared before and are hard to be directly obtained by individual Lewis acidic etching. By selecting various Lewis bases with different anions such as S^{2-} , Se^{2-} , Te^{2-} , N^{3-} and NH_2^- , researchers can obtain the desired surface groups-terminated MXenes. The above discussions fully reveal the great potential of the halogenated MXenes synthesized by Lewis acidic etching method in various fields. Taking consideration of the rich selection of M and

X elements as well as various surface groups mentioned above, there are a large number of new MXenes that can be explored, which may show some excellent properties. Up to now, the regulation of MXene surface groups through chemical transformation is still in its infancy and plenty of theoretical calculations and experiments are required to further explore the effect of these new functional groups on the properties of different MXenes, such as electrical conductivity, ion diffusion kinetics, thermal conductivity, work function, optical conductivity, mechanical property, hydrophilicity, chemical and thermal stability.

3.3 In-Situ Formed Metals

According to the etching mechanism shown in Eq. (22), metal ions in the Lewis acidic molten salts can be in-situ reduced to various metals during the etching process of MAX precursors, thus leading to the formation of MXenes/metals composites. Taking CuCl_2 etching of Ti_3SiC_2 MAX as an example, Cu nanoparticles can be uniformly anchored among the multi-layered $\text{Ti}_3\text{C}_2\text{T}_x$ MXene matrix and the $\text{Ti}_3\text{C}_2\text{T}_x/\text{Cu}$ hybrids can be successfully obtained [67]. It is worth mentioning that Cu nanoparticles are able to be loaded in the $\text{Ti}_3\text{C}_2\text{T}_x$ MXene matrix through one-step in-situ growth process, so the interaction between them is stronger than that of $\text{Ti}_3\text{C}_2\text{T}_x/\text{Cu}$ composites prepared by mechanical mixing, which is another key advantage of Lewis acidic etching method relative to traditional etching route. Recently, it has been reported that when the Ti_3AlC_2 MAX precursor is etched by $\text{CuCl}_2 \cdot 2\text{H}_2\text{O}$ or $\text{CoCl}_2 \cdot 6\text{H}_2\text{O}$, the obtained $\text{Ti}_3\text{C}_2\text{T}_x$ MXene can be decorated with Cu or Co nanoparticles (Fig. 8a), respectively [122]. The strong interaction between Cu nanoparticles and $-\text{O}$ surface group of $\text{Ti}_3\text{C}_2\text{T}_x$ MXene can be proved by X-ray absorption (XAS) spectrum (Fig. 8b), effectively preventing the detachment of Cu from the $\text{Ti}_3\text{C}_2\text{T}_x$ MXene matrix. Furthermore, owing to the diversity of MXene compositions and the large family of Lewis acidic molten salts, various metal nanoparticles (Fe, Co, Ni, Zn, Ag, Cd, Sn, etc.) can be distributed among the different MXenes (Ti_3C_2 , Ti_3CN , Ti_2C , Ta_2C , Nb_2C , etc.), which greatly enriches the choice of researchers.

In the early development stage of the Lewis acidic etching strategy, researchers generally remove the in-situ generated metal nanoparticles from MXenes/metals composites in order to obtain pure MXenes, which almost becomes a

custom. However, metal or metal compounds have been intensively investigated in energy storage and conversion, electromagnetic interference shielding and other fields in the past few decades [129–133]. Consequently, rational and effective application of various metals in MXenes/metals composites obtained by Lewis acidic etching is worth investigating. Additionally, MXenes have been widely utilized to support metal or metal compounds. Based on the excellent synergistic effect between MXenes and metals or metal compounds, MXenes/metals hybrids and MXenes/metal compounds composites exhibit better performance than their individual components and have been widely investigated in various fields [54, 73, 134–138]. Nevertheless, the traditional fabrication process of MXenes/metals hybrids or MXenes/metal compounds composites usually requires the synthesis of MXenes and the subsequent introduction of additional metal sources, which makes the preparation process complicated [117, 139–144]. As mentioned above, Lewis acidic salts can achieve the etching of MAX precursor and the introduction of metal sources simultaneously. Therefore, if Lewis acidic molten salts are used to etch MAX phases, the obtained MXenes/metals composites can be applied directly, and then the MXenes/metal compounds composites can be prepared by one-step sulfurization, phosphorization, tellurization or selenization treatment of MXenes/metals composites, which opens a new window for the universal construction of MXene-based hybrids through Lewis acidic etching route, showing great research potential.

In general, MXenes/metals or MXenes/metal compounds composites can be obtained quickly and easily by taking full advantage of Lewis acidic etching products. As expected, the MXenes/metals and MXenes/metal compounds composites prepared by Lewis acidic etching route have been rationally applied in some fields due to the superior structural stability. For example, the reported $\text{Ti}_3\text{C}_2-\text{Cu}$ composites via $\text{CuCl}_2 \cdot 2\text{H}_2\text{O}$ molten salts etching exhibit superior electrochemical performance in SCs when used as electrode material [122]. Additionally, Sn-nanoconfined $\text{Ti}_3\text{C}_2\text{T}_x$ MXene was synthesized by one-step SnCl_2 molten salt etching (Fig. 8c–d), and demonstrated excellent cyclic stability as anode for LIBs [145]. Further, CoCl_2 etching and in-situ sulfidation process were used to prepare strongly coupled N-doped MXene- CoS_2 composites, which can effectively alleviate the shuttle effect of lithium polysulfides (LiPSs) in lithium-sulfur

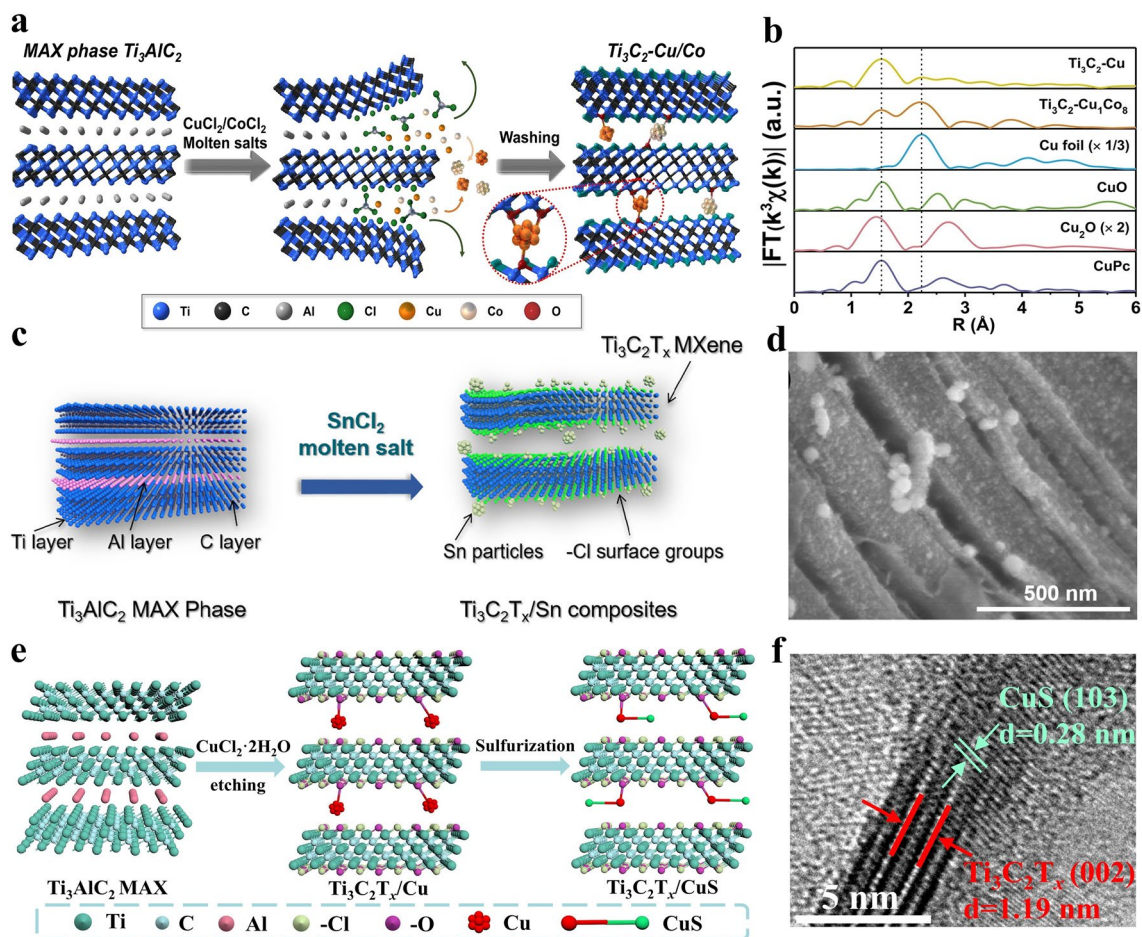


Fig. 8 **a** Schematic illustration of the synthesis of Ti_3C_2 -Cu/Co composites. **b** XAS spectra of Ti_3C_2 -Cu hybrids. Reproduced with permission from [122] Copyright 2021, Wiley–VCH. **c** Schematic showing the preparation of $Ti_3C_2T_x$ /Sn composites by $SnCl_2$ Lewis acidic salt etching. **d** SEM image of $Ti_3C_2T_x$ /Sn hybrids. Reproduced with permission from [145] Copyright 2022, Elsevier. **e** Schematic diagram of the preparation of $Ti_3C_2T_x$ /CuS composites. **f** High-resolution transmission electron microscope (HRTEM) image of $Ti_3C_2T_x$ /CuS. Reproduced with permission from [148] Copyright 2022, Royal Society of Chemistry

(Li–S) batteries [146]. Recently, our group presented a general method to fabricate a series of $Ti_3C_2T_x$ MXene/transition metal sulfides (MS_y , $M = Fe, Co, Ni$ or Cu) composites via Lewis acidic etching and subsequent sulfurization treatment (Fig. 8e–f) [147, 148]. When served as anodes for SIBs, the readily produced hybrids can show greatly boosted sodium storage performance owing to the interfacial electronic coupling. Until now, the applications of Lewis acidic molten salts etching products, especially the in-situ formed metals, have been relatively rare and concentrated in the field of energy storage. More rational utilization of etching products in other fields, such as electromagnetic interference shielding, demonstrates great potential and deserves further exploration.

3.4 Delamination of Multi-Layered MXenes

The MXenes prepared by Lewis acidic etching strategy exhibit obvious multi-layered accordion morphology. In order to demonstrate true 2D morphology, it is necessary to implement intercalation and delamination process to obtain single-layered or few-layered MXene nanosheets, which can expose more active sites and possess higher surface area [71]. In general, MXenes prepared by HF etching are terminated with $-O$ and $-OH$ functional groups and therefore show excellent hydrophilicity [81], which makes it easy to disperse MXenes in water. The well-dispersed MXenes can then be intercalated by organic molecules (urea, amine, DMSO, TMAOH, TBAOH, IPA, etc.) and inorganic

substances (LiCl, NaCl, KCl), which increases the gallery spacing and weakens the van der Waals force and hydrogen bond between MXene layers [43, 78–80, 149, 150]. Finally, the few-layered MXenes nanosheets can be obtained by ultrasonic and centrifugation processing [151, 152]. Nevertheless, MXenes prepared by Lewis acidic etching method fail to be terminated by –OH functional group, which greatly decreases their hydrophilicity [153–155]. Therefore, it is difficult to uniformly disperse the obtained MXenes in water to form stable colloidal solution, which greatly reduces the delamination efficiency, thus exhibiting a low yield of few-layered and single-layered nanosheets. In order to enhance the delamination efficiency, researchers often considerably extend the sonication time, which tends to endow MXenes with small lateral size and poor quality. In general, most of the MXenes synthesized by Lewis acidic etching is at the multi-layered state according to the published articles, and only a few of them are at the few-layered state.

For example, $\text{Ti}_3\text{C}_2\text{Cl}_x$ nanosheets with lateral dimensions of 0.4–2.0 μm were prepared by 10 h ultrasonication treatment of multi-layered MXene obtained by ZnCl_2 etching [156]. Yang et al. synthesized $\text{Ti}_3\text{C}_2\text{T}_x$ nanosheets through ZnCl_2 etching and IPA intercalation assisted by ultrasonication treatment for 20 h [157]. Additionally, Zhao et al. successfully produced $\text{Ti}_3\text{C}_2\text{Cl}_x$ nanosheets via ZnCl_2 etching and subsequent ultrasonication process lasting 20 h [158]. Further, Zhou et al. prepared Cl-terminated Ti_3C_2 MXene by CdCl_2 molten salt etching, and the multi-layered MXene was intercalated by IPA molecule followed by 25 h ultrasonication process to obtain few-layered nanosheets with lateral size of hundreds of nanometers [159]. Furthermore, Liu et al. used large organic base molecule TBAOH to intercalate into $\text{Ti}_3\text{C}_2\text{T}_x$ MXene produced by CuCl_2 etching, followed by ultrasonication bath for 6 h at low temperature to separate the layers, leading to the few-layered nanosheets with a lateral size of around 600 nm [153]. It is worth mentioning that TMAOH intercalated Lewis acidic salts etched- $\text{Ti}_3\text{C}_2\text{T}_x$ MXene suspension can be stably stored for 2 weeks without obvious precipitation. Finally, DMSO molecule intercalation and ultrasonication process can also be used to delaminate the Cl-terminated Ti_3C_2 MXene prepared by CuCl_2 etching to obtain few-layered samples [125]. To sum up, due to the poor hydrophilicity of MXenes prepared by Lewis acidic etching, the delamination usually requires large organic molecules and long-time sonication,

which leads to low yields of few-layered MXenes and small lateral sizes of nanosheets.

In order to solve the above-mentioned issues, two viable and effective methods have been proposed. The first method is to enhance the hydrophilicity of MXenes, and the other method is to disperse MXenes in organic solvents instead of water for intercalation and delamination. For example, Arole et al. presented a method to produce water-dispersible $\text{Ti}_3\text{C}_2\text{T}_x$ nanosheets via SnF_2 molten salt etching, KOH washing, DMSO intercalation and bath sonication for 1 h (Fig. 9a) [154]. The KOH washing facilitates the introduction of –OH terminal groups on $\text{Ti}_3\text{C}_2\text{T}_x$ MXene and thus greatly boosts the formation of stable $\text{Ti}_3\text{C}_2\text{T}_x$ suspension with a zeta potential of –31.7 mV. The few-layered or single-layered $\text{Ti}_3\text{C}_2\text{T}_x$ nanosheets can be prepared by DMSO intercalation and sonication for only 1 h (Fig. 9b), which is conducive to reduce the required energy during the sonication process. Finally, the $\text{Ti}_3\text{C}_2\text{T}_x$ film produced by vacuum filtration exhibits an electronic conductivity of 706 S cm^{-1} . In addition, Kamysbayev et al. immersed multi-layered $\text{Ti}_3\text{C}_2\text{T}_x$ ($\text{T} = -\text{Cl}, -\text{S}$ or $-\text{NH}$) MXene obtained by Lewis acidic etching and surface functionalization in *n*-butyllithium (*n*-BuLi) hexanes solution to complete the Li^+ intercalation process (Fig. 9c). Then, the lithium-intercalated $\text{Ti}_3\text{C}_2\text{T}_x$ MXene was added to the polar organic solvent *N*-methyl formamide (NMF) rather than water, leading to the stable colloidal solution with a zeta potential of –29.3 mV after bath sonication for 1 h (Fig. 9d) [42]. The as-prepared $\text{Ti}_3\text{C}_2\text{T}_x$ suspension of single-layered nanosheets exhibit obvious Tyndall effect and superior crystallinity (Fig. 9e–g), showing the advantage and potential of delamination in polar organic solvents. However, *n*-BuLi is difficult to be widely used as intercalator due to its high risk. In conclusion, although some progress has been made in the delamination of multi-layered MXenes obtained by Lewis acidic etching, there is still no simple, safe and effective method to prepare MXene nanosheets with high yield and large lateral size.

Table 1 compares non-Lewis acidic etching strategies with Lewis acidic etching in terms of some key indicators such as universality, scalability, safety and terminations.

It can be concluded that Lewis acidic etching exhibits good universality, scalability and safety relative to other methods. Table 2 comprehensively summarizes the parameters for the preparation of various MXenes by Lewis acidic etching, which includes the molar ratio of MAX precursor and Lewis acidic salts, reaction temperature, time and

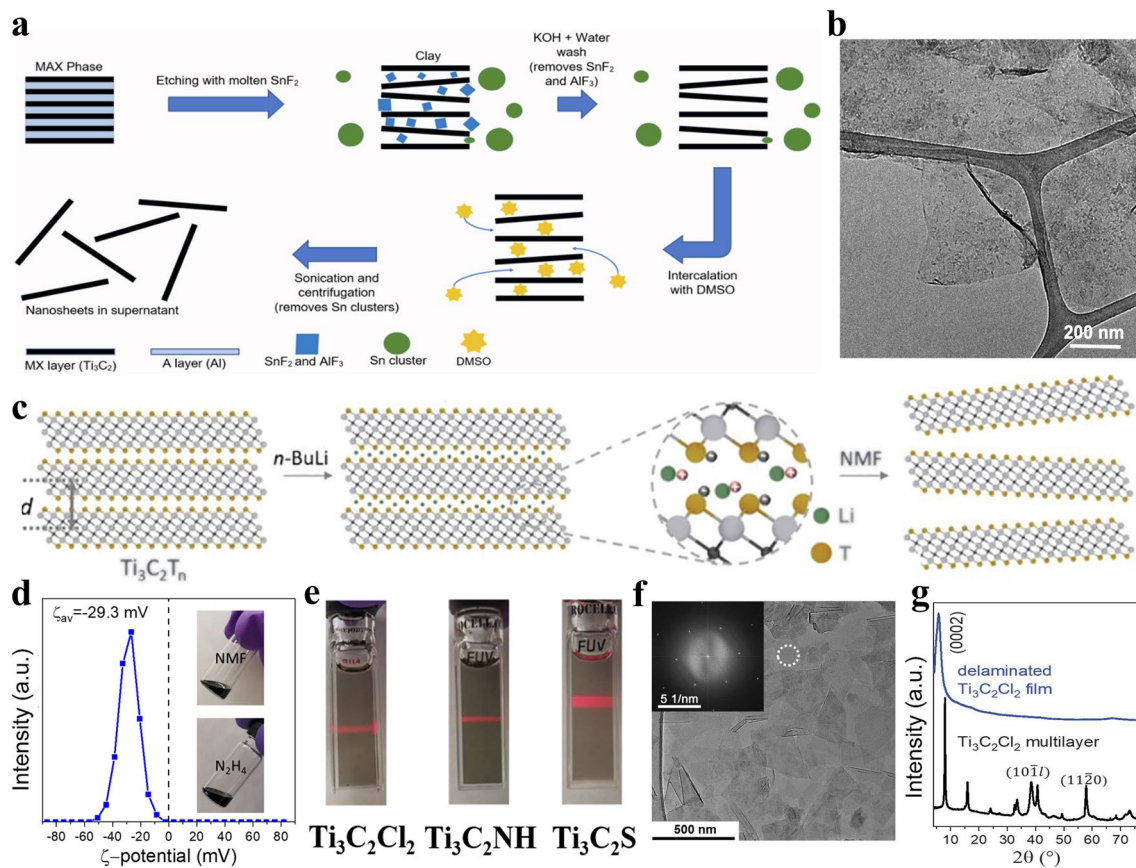


Fig. 9 **a** Schematic of the synthesis of KOH-treated few-layered $Ti_3C_2T_x$ MXene nanosheets. **b** Transmission electron microscope (TEM) image of $Ti_3C_2T_x$ nanosheets. Reproduced with permission from [154] Copyright 2021, The Authors. **c** Schematic of the intercalation and delamination process. **d** Zeta potential of $Ti_3C_2Cl_2$ MXene in NMF and inset representing the high concentrated MXene inks in NMF and N_2H_4 . **e** Digital photographs of stable colloidal solutions of $Ti_3C_2T_x$ MXenes ($T = -Cl, -NH$ and $-S$) in NMF showing Tyndall effect. **f** TEM image of $Ti_3C_2Cl_2$ MXene nanosheets and inset showing its selected area electron diffraction (SAED) pattern. **g** XRD patterns of multi-layered and delaminated $Ti_3C_2Cl_2$ MXene. Reproduced with permission from [42] Copyright 2020, The American Association for the Advancement of Science

atmosphere. Additionally, delamination parameters such as the type of intercalators and sonication time are also presented.

4 Applications

Benefiting from the unique layered structure, superior electronic conductivity, low ion diffusion barrier, uniform and

Table 1 Comparison of non-Lewis acidic etching techniques and Lewis acidic etching routes

Methods	Universality	Scalability	Safety	Terminations
HF etching	Good	Good	Poor	-O, -OH and -F
In-situ HF etching	Good	Good	Medium	-O, -OH and -F
Alkali etching	Poor	Poor	Poor	-O and -OH
Electrochemical etching	Medium	Poor	Good	-O, -OH and -Cl
Bifluoride salts etching	Poor	Medium	Medium	-O, -OH and -F
Common molten salts etching	Poor	Medium	Good	-O and -F
Lewis acidic etching	Good	Good	Good	-Cl, -Br or -I

Table 2 The specific parameters for the preparation of various MXenes via Lewis acidic etching

MXenes	MAX: Lewis acidic salt (molar ratio)	Reaction condition	Intercalator	Sonication time	Refs.
Ti ₃ C ₂ Cl ₂	Ti ₃ AlC ₂ :ZnCl ₂ = 1:6	550 °C, 5 h, Ar	/	/	[66]
Ti ₃ C ₂ Cl ₂	Ti ₃ AlC ₂ :ZnCl ₂ = 1:6	550 °C, 7 h, Ar	/	/	[246]
Ti ₃ C ₂ Cl ₂	Ti ₃ AlC ₂ :ZnCl ₂ = 1:2.4	650 °C, 5 h, Ar	/	/	[211]
Ti ₃ C ₂ Cl ₂	Ti ₃ AlC ₂ :ZnCl ₂ = 1:6	550 °C, 7 h, Ar	/	/	[247]
Ti ₃ C ₂ Cl ₂	Ti ₃ AlC ₂ :ZnCl ₂ = 1:6	550 °C, 5 h, Ar	/	/	[113]
Ti ₃ C ₂ Cl ₂	Ti ₃ AlC ₂ :CuCl ₂ = 1:6	550 °C, 5 h, Ar	/	/	[237]
Ti ₃ C ₂ Cl ₂	Ti ₃ AlC ₂ :CuCl ₂ = 1:3	700 °C, 7 h, Ar	/	/	[212]
Ti ₃ C ₂ Cl ₂	Ti ₃ AlC ₂ :CuCl ₂ = 1:3	700 °C, 10 h, Ar	/	/	[218]
Ti ₃ C ₂ Cl ₂	Ti ₃ AlC ₂ :CdCl ₂ = 1:8	610 °C, 6 h, Ar	NaCl	72 h	[219]
Ti ₃ C ₂ Cl ₂	Ti ₃ AlC ₂ :CdCl ₂ = 1:8	610 °C, 6 h, Ar	CTAB	72 h	[219]
Ti ₃ C ₂ Cl ₂	Ti ₃ AlC ₂ :CdCl ₂ = 1:8	600 °C, 6 h, /	/	/	[222]
Ti ₃ C ₂ Cl _x	Ti ₃ AlC ₂ :ZnCl ₂ = 1:5.7	550 °C, 10 h, Ar	/	10 h	[156]
Ti ₃ C ₂ Cl _x	Ti ₃ (Al _{1-x} Cu _x)C ₂ :ZnCl ₂ = 1:7	600 °C, 5 h, Ar	/	20 h	[158]
Ti ₃ C ₂ Cl _x	Ti ₃ AlC ₂ :CdCl ₂ = 1:8	610 °C, 7 h, N ₂	IPA	25 h	[159]
Ti ₃ C ₂ Cl _x	Ti ₃ AlC ₂ :NiCl ₂ = 1:6	750 °C, 0.3 h, Air	/	/	[177]
Ti ₃ C ₂ Cl _x	Ti ₃ AlC ₂ :CuCl ₂ = 1:3	700 °C, 7 h, Ar	DMSO	/	[125]
Ti ₃ C ₂ Cl _x	Ti ₃ AlC ₂ :CuCl ₂ = 1:3	700 °C, 24 h, Ar	/	/	[128]
Ti ₃ C ₂ Cl _x	Ti ₃ AlC ₂ :FeCl ₂ = 1:3	700 °C, 7 h, Ar	/	/	[126]
Ti ₃ C ₂ Br ₂	Ti ₃ AlC ₂ :CdBr ₂ = 1:8	610 °C, 6 h, Ar	<i>n</i> -BuLi	1 h	[42]
Ti ₃ C ₂ Br _x	Ti ₃ AlC ₂ :NiBr ₂ = 1:6	750 °C, 0.3 h, Air	/	/	[178]
Ti ₃ C ₂ I ₂	Ti ₃ AlC ₂ :CuI = 1:6	700 °C, 7 h, Ar	/	/	[123]
Ti ₃ C ₂ I ₂	Ti ₃ AlC ₂ :CuI = 1:6	700 °C, 7 h, Ar	/	/	[194]
Ti ₃ C ₂ I _x	Ti ₃ AlC ₂ :CuI = 1:6	700 °C, 7 h, Ar	/	/	[234]
Ti ₃ C ₂ T _x	Ti ₃ SiC ₂ :CuCl ₂ = 1:3	750 °C, 24 h, Ar	/	/	[67]
Ti ₃ C ₂ T _x	Ti ₃ AlC ₂ :CuCl ₂ = 1:3	680 °C, 24 h, Ar	TBAOH	6 h	[153]
Ti ₃ C ₂ T _x	Ti ₃ AlC ₂ :CuCl ₂ = 1:6	700 °C, 0.7 h, Air	/	/	[175]
Ti ₃ C ₂ T _x	Ti ₃ AlC ₂ :CuCl ₂ = 1:3	700 °C, 8 h, Ar	/	/	[180]
Ti ₃ C ₂ T _x	Ti ₃ AlC ₂ :CuCl ₂ ·2H ₂ O = 1:3	750 °C, 24 h, Ar	/	/	[122]
Ti ₃ C ₂ T _x	Ti ₃ AlC ₂ :CuCl ₂ ·2H ₂ O = 1:3	750 °C, 20 h, Ar	/	/	[148]
Ti ₃ C ₂ T _x	Ti ₃ AlC ₂ :ZnCl ₂ = 1:8.8	600 °C, 5 h, Ar	IPA	20 h	[157]
Ti ₃ C ₂ T _x	Ti ₃ AlC ₂ :CoCl ₂ = 1:3	750 °C, 15 h, Ar	/	/	[232]
Ti ₃ C ₂ T _x	Ti ₃ AlC ₂ :CoCl ₂ = 1:3	700 °C, 24 h, Ar	/	/	[146]
Ti ₃ C ₂ T _x	Ti ₃ AlC ₂ :CoCl ₂ = 1:3	750 °C, 2 h, N ₂	/	/	[251]
Ti ₃ C ₂ T _x	Ti ₃ AlC ₂ :FeCl ₂ = 1:5	700 °C, 6 h, Ar	/	/	[244]
Ti ₃ C ₂ T _x	Ti ₃ AlC ₂ :FeCl ₂ ·4H ₂ O = 1:3	750 °C, 24 h, Ar	/	/	[147]
Ti ₃ C ₂ T _x	Ti ₃ AlC ₂ :SnCl ₂ = 1:3	600 °C, 8 h, Ar	/	/	[145]
Ti ₃ C ₂ T _x	Ti ₃ AlC ₂ :SnF ₂ = 1:6	550 °C, 6 h, Ar	DMSO	1 h	[154]
Ti ₃ CNCl ₂	Ti ₃ AlCN:CoCl ₂ = 1:6	750 °C, 24 h, Ar	/	1 h	[250]
Ti ₃ CNCl ₂	Ti ₃ AlCN:NiCl ₂ = 1:4.6	750 °C, 4 h, Ar	/	/	[233]
Ti ₃ CNT _x	Ti ₃ AlCN:CuCl ₂ = 1:3	700 °C, 24 h, Ar	/	/	[240]
Ti ₂ NT _x	Ti ₂ AlN:CuCl ₂ = 1:3	450 °C, 1 h, Ar	/	/	[176]
Nb ₂ CCl _x	Nb ₂ AlC:CdCl ₂ = 1:10	750 °C, 36 h, Ar	/	/	[62]
Nb ₂ CT _x	Nb ₂ AlC:CuCl ₂ = 1:3	750 °C, 5 h, Ar	/	/	[119]
Nb ₂ CT _x	Nb ₂ AlC:SnF ₂ = 1:6	750 °C, 36 h, Ar	i-PrA	1 h	[155]

tunable surface functional groups and large interlayer spacing, the obtained MXenes and MXene-based composites via Lewis acidic molten salts etching route have been intensively investigated in various fields, such as energy storage, energy conversion, sensors and microwave absorption.

4.1 Energy Storage

Due to the rapid consumption of fossil fuels and gradually serious environmental pollution, the development of clean renewable energy has become more and more important [160, 161]. However, the intermittency and instability of renewable energy makes it necessary to store the generated electricity [162]. In recent years, electrochemical energy storage devices have received increasing research interests because of their fast response speed, versatility and application flexibility [163]. Among the various electrochemical energy storage devices, LIBs currently occupy an absolute dominant position. Other technologies such as SIBs, ZIBs, Li-S batteries and SCs are in a rapid development period [164]. In particular, SIBs are promising for large-scale energy storage in the following few years owing to the low price and abundant sodium resources [165].

4.1.1 Lithium-Ion Batteries

In the past three decades, significant progress has been made in the development of LIBs technology. Derived from the high power and energy density, long cycle life, high energy conversion efficiency and low discharge rate, LIBs system has now been widely used in consumer devices, electric vehicles and large-scale energy storage [166, 167]. Layered materials have been intensively studied as electrode materials for LIBs due to their unique structural stability. As early as 2012, Tang et al. confirmed that Ti_3C_2 MXene possesses low Li^+ diffusion barrier, superior electronic conductivity, low discharge voltage and high lithium storage capacity via theoretical computation, making it a promising LIBs anode [59]. Since then, a large number of works have experimentally proved that MXene-based anodes can deliver relatively high discharge capacity, stable long-term cyclic performance and outstanding rate performance [72, 168–171]. The theoretical capacities of MXene electrodes depends on formula weight, interlayer spacing as well as the type of transition metals and surface groups. MXenes

with low formula weights such as V_2C and Ti_2C can afford large gravimetric capacities [88, 172, 173]. In addition, large interlayer spacing can allow more Li^+ ions to intercalate into the MXenes, accordingly leading to higher specific capacities [30, 174]. Surface functional groups such as $-\text{F}$ and $-\text{OH}$ has been proved to impede Li^+ transportation via theoretical calculations, which is unfavorable for realization of theoretical specific capacity [59, 172]. However, O-terminated Ti_3C_2 MXene can absorb two Li layers, confirming the lithium affinity of $-\text{O}$ functional groups and thus contributing to the enhanced lithium storage capacity (Fig. 10a) [120].

It is worth mentioning MXenes obtained by Lewis acidic etching method may exhibit better electrochemical performance due to the absence of $-\text{F}$ and $-\text{OH}$ surface groups and the introduction of $-\text{O}$ termination. In 2020, Li et al. prepared multi-layered $\text{Ti}_3\text{C}_2\text{T}_x$ MXene ($\text{T} = -\text{O}$ and $-\text{Cl}$) via CuCl_2 etching of Ti_3SiC_2 precursor [67]. When used as anode for LIBs, the obtained $\text{Ti}_3\text{C}_2\text{T}_x$ MXene exhibit a distinct pseudocapacitive-shaped cyclic voltammetry (CV) curves without redox peaks in organic electrolyte. In comparison, MXene anodes synthesized by HF etching generally show obvious redox peaks in CV profiles [168, 171]. In addition, $\text{Ti}_3\text{C}_2\text{T}_x$ MXene delivers a discharge capacity of 205 mAh g^{-1} at 0.6C rate, corresponding to the fact that per Ti atom can transfer around 0.4 electrons. Further, superior long-term cyclic stability up to 2400 cycles can be obtained for multi-layered $\text{Ti}_3\text{C}_2\text{T}_x$ MXene electrode. The superior lithium storage performance can be attributed to the strong adsorption ability of $-\text{O}$ surface group on Li^+ cations [120]. Moreover, the Li^+ insertion/deinsertion storage mechanism can be confirmed by the enlarged/decreased interlayer spacing through in-situ XRD measurement. In 2021, the Nb_2CT_x MXene ($\text{T} = -\text{O}$ and $-\text{Cl}$) with obvious accordion-like morphology was prepared by CuCl_2 molten salt etching of Nb_2AlC precursor [119]. The theoretical calculations indicate that $-\text{O}$ surface groups can obtain more electrons from Nb atoms than $-\text{Cl}$ termination for Nb_2CT_x MXene, thus resulting in the substitution of $-\text{O}$ for $-\text{Cl}$ functional groups during ammonium persulfate solution washing process, which is conducive to its lithium storage performance. Nb_2CT_x MXene anode delivers a high discharge capacity of 330 mAh g^{-1} at 50 mA g^{-1} (Fig. 10b), which is larger than the theoretical specific capacities of Nb_2C (305 mAh g^{-1}) and Nb_2CO_2 (292 mAh g^{-1}). Additionally, capacity rising phenomenon can be clearly observed for Nb_2CT_x MXene

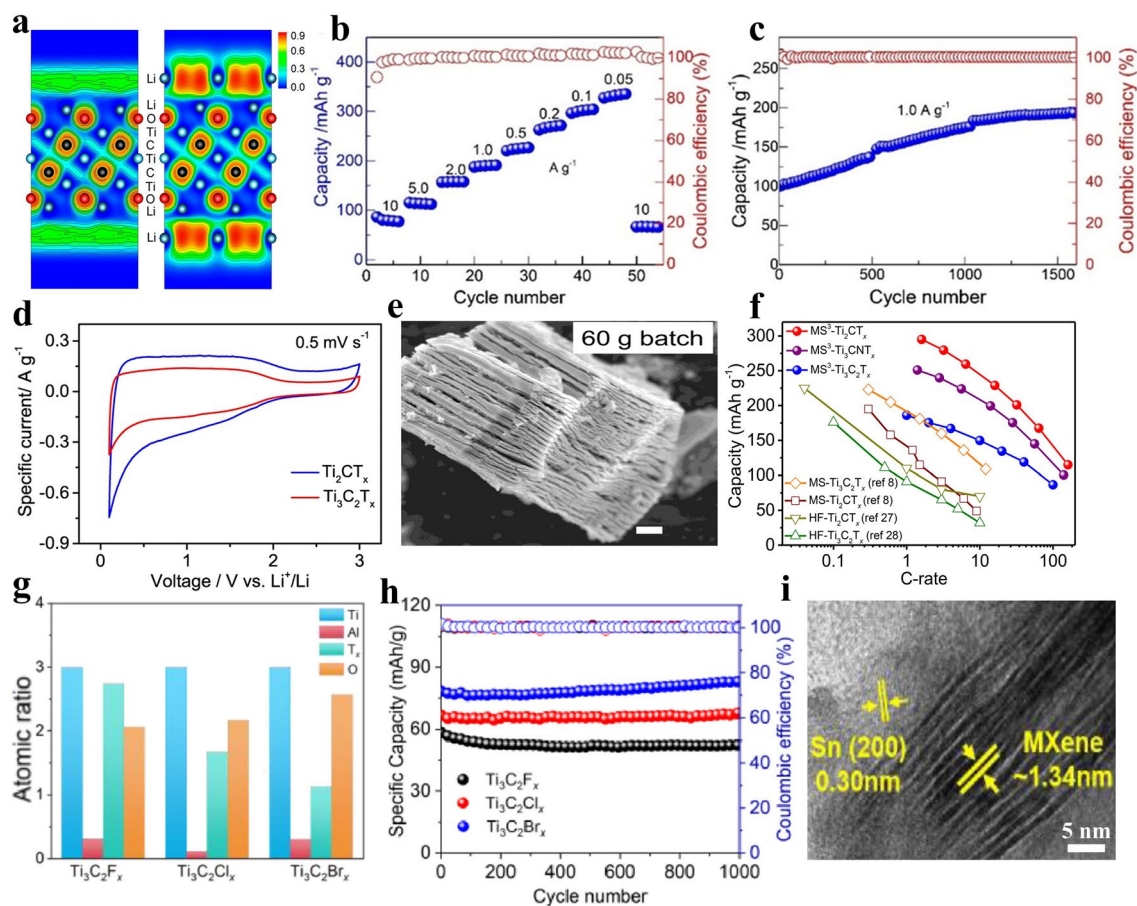


Fig. 10 **a** Valence electron localization function of $\text{Ti}_3\text{C}_2\text{O}_2\text{Li}_2$ with or without an extra Li layer. Reproduced with permission from [120] Copyright 2014, American Chemical Society. **b** Rate performance of Nb_2CT_x MXene. **c** Long-term cyclic performance of Nb_2CT_x MXene. Reproduced with permission from [119] Copyright 2021, Wiley-VCH. **d** CV curves of Ti_2CT_x and $\text{Ti}_3\text{C}_2\text{T}_x$ MXene. Reproduced with permission from [112] Copyright 2021, The Authors, published by Springer Nature. **e** SEM image of $\text{Ti}_3\text{C}_2\text{T}_x$ MXene prepared from 60 batch of Ti_3AlC_2 MAX. **f** Specific capacities of $\text{Ti}_3\text{C}_2\text{T}_x$, Ti_2CT_x and Ti_3CNT_x MXene at various C-rates. Reproduced with permission from [175] Copyright 2022, Zhengzhou University. **g** Elemental composition comparison of $\text{Ti}_3\text{C}_2\text{F}_x$, $\text{Ti}_3\text{C}_2\text{Cl}_x$ and $\text{Ti}_3\text{C}_2\text{Br}_x$ MXenes. **h** Long-term cyclic performance of $\text{Ti}_3\text{C}_2\text{F}_x$, $\text{Ti}_3\text{C}_2\text{Cl}_x$ and $\text{Ti}_3\text{C}_2\text{Br}_x$ MXenes at 1 A g^{-1} . Reproduced with permission from [178] Copyright 2022, Elsevier. **i** TEM image of $\text{Ti}_3\text{C}_2\text{T}_x/\text{Sn}$ anode after 2200 cycles. Reproduced with permission from [145] Copyright 2022, Elsevier

at 1000 mA g^{-1} (Fig. 10c), which can be attributed to the electrochemical activation and common pillaring effect.

In 2022, Lin et al. prepared Ti_2CT_x and $\text{Ti}_3\text{C}_2\text{T}_x$ MXene by one-pot method in an air atmosphere with Ti, C, and Al powders as precursor, simultaneously achieving the synthesis of MAX and in-situ CuCl_2 etching in molten salts system [112]. When served as anodes for LIBs, Ti_2CT_x and $\text{Ti}_3\text{C}_2\text{T}_x$ electrode both exhibit rectangular and symmetric CV curves in a voltage range of 0.1–2 V (Fig. 10d), which is similar to those of previously reported MXene electrodes prepared by Lewis acidic etching [67]. Furthermore, Ti_2CT_x anode shows discharge capacities of 256 and 164 mAh g^{-1} at 0.5 and 10 mV s^{-1} , respectively. In comparison, specific capacities

of 164 and 113 mAh g^{-1} can be obtained for $\text{Ti}_3\text{C}_2\text{T}_x$ electrode at the same scan rate. The superior rate performance of these two MXene electrodes is mainly due to the pseudocapacitive-controlled charge storage mechanism. Later, Chen et al. reported the synthesis of $\text{Ti}_3\text{C}_2\text{T}_x$, Ti_2CT_x , Ti_3CNT_x and $\text{Ti}_4\text{N}_3\text{T}_x$ MXene via molten salts-shielded synthesis strategy in air atmosphere with MAX phases as precursor and CuCl_2 molten salt as etchant [175]. The low-melting eutectic salt reaction medium can effectively restrain the oxidation of MXenes at high temperature. More importantly, the proposed method can be used to prepare $\text{Ti}_3\text{C}_2\text{T}_x$ MXene on a relatively large scale. The distinct accordion-like structure can still be obtained for $\text{Ti}_3\text{C}_2\text{T}_x$ MXene prepared from

60 g batch of Ti_3AlC_2 MAX (Fig. 10e), demonstrating superior scalability. Among the $\text{Ti}_3\text{C}_2\text{T}_x$, Ti_2CT_x and Ti_3CNT_x MXene electrodes, Ti_2CT_x anode delivers the largest discharge capacity, and the three electrodes all exhibit excellent rate performance (Fig. 10f).

Recently, Cao et al. demonstrated the successful preparation of multi-layered Ti_2NT_x MXene ($\text{T} = -\text{O}$ and vCl) via CuCl_2 etching at 450°C for 1 h [176]. The existence of Ti-Cl and Ti-O bonds can be confirmed by XPS and XAS measurement. Theoretical calculations indicate that the Gibbs energy change of $-\text{O}$ substituting $-\text{Cl}$ termination is -2.3 eV, while the value of $-\text{O}$ replacing $-\text{F}$ surface group is 0.07 eV, demonstrating that $-\text{Cl}$ can be readily substituted by $-\text{O}$. The obtained Ti_2NT_x MXene can deliver high discharge capacities of 303.4 and 158.4 mAh g^{-1} at 0.1 and 5 A g^{-1} , respectively. More importantly, a large capacity of 350 mAh g^{-1} after 1,200 cycles at 1 A g^{-1} can be obtained for Ti_2NT_x electrode, revealing outstanding cycling stability. A hybrid capacitor by pairing Ti_2NT_x anode and super activated carbon cathode can demonstrate an energy density of 45.36 Wh kg^{-1} at 123.32 W kg^{-1} . It is noteworthy that the MXene electrodes mentioned above are all at multi-layered state, and few-layered MXene electrodes may show better electrochemical performance. Liu et al. reported the synthesis of exfoliated $\text{Ti}_3\text{C}_2\text{T}_x$ MXene (termed as e-MS- $\text{Ti}_3\text{C}_2\text{T}_x$) via CuCl_2 molten salts etching and subsequent TBAOH intercalation [153]. The e-MS- $\text{Ti}_3\text{C}_2\text{T}_x$ electrode delivers discharge capacities of 225 and 95 mAh g^{-1} at 0.2 and 16 A g^{-1} , respectively, which is higher than that of unexfoliated $\text{Ti}_3\text{C}_2\text{T}_x$ anode. The boosted rate performance of e-MS- $\text{Ti}_3\text{C}_2\text{T}_x$ electrode is mainly assigned to the enhanced contact area between electrode and electrolyte after exfoliation. Additionally, the increased content of $-\text{O}$ termination after TBAOH treatment will also benefit the lithium storage performance [177].

The type of halogen terminations may have an influence on the electrochemical performance of MXene. Liu et al. synthesized $\text{Ti}_3\text{C}_2\text{T}_x$ MXene with $-\text{F}$, $-\text{Cl}$ or $-\text{Br}$ functional groups via HF , NiCl_2 or NiBr_2 etching, respectively [178]. The typical accordion morphology can be afforded for three halogenated MXenes. The element composition analysis shows that $\text{Ti}_3\text{C}_2\text{Br}_x$ MXene possesses the highest content of $-\text{O}$ surface group among the $\text{Ti}_3\text{C}_2\text{F}_x$, $\text{Ti}_3\text{C}_2\text{Cl}_x$ and $\text{Ti}_3\text{C}_2\text{Br}_x$ MXene (Fig. 10g). This phenomenon is mainly assigned to the fact that the formation energy of Ti-Br bond is the lowest compared with that of Ti-Cl and Ti-F bonds

according to theoretical calculations. Consequently, $-\text{O}$ can easily replace the $-\text{Br}$ surface group when the prepared $\text{Ti}_3\text{C}_2\text{Br}_x$ MXene is exposed to air, and the highest content of $-\text{O}$ functional group contributes to the largest discharge capacity of 189 mAh g^{-1} for $\text{Ti}_3\text{C}_2\text{Br}_x$ anode. Finally, the $\text{Ti}_3\text{C}_2\text{Br}_x$ electrode exhibits the best rate performance and cyclic performance relative to $\text{Ti}_3\text{C}_2\text{F}_x$ and $\text{Ti}_3\text{C}_2\text{Cl}_x$ anode (Fig. 10h). The electrode materials mentioned above are all individual MXenes, while the MXene/active metal composites can also be utilized as anodes for LIBs. Wu et al. reported the preparation of Sn-nanoconfined $\text{Ti}_3\text{C}_2\text{T}_x$ MXene hybrids via SnCl_2 molten salt etching of Ti_3AlC_2 [145]. The Sn nanoparticles are in-situ grown and confined between the $\text{Ti}_3\text{C}_2\text{T}_x$ MXene during the etching process. It is noteworthy that the confined effect of MXene can effectively prevent the aggregation of Sn nanoparticles at high temperature and accommodate its large volume variation upon cycling. As a result, $\text{Ti}_3\text{C}_2\text{T}_x/\text{Sn}$ anode remains a reversible capacity of 226.2 mAh g^{-1} after 1000 cycles at 0.2 A g^{-1} , which is higher than that of pure $\text{Ti}_3\text{C}_2\text{T}_x$ and Sn electrode. The volume expansion of Sn nanoparticles can gradually enlarge the interlayer spacing of MXene from 1.17 to 1.34 nm after 2200 cycles (Fig. 10i), which greatly exposes more active sites upon cycling and contributes to the obvious capacity rising phenomenon.

4.1.2 Sodium-Ion Batteries

SIBs possess a similar working mechanism to LIBs. It is well known that the working voltage of SIBs is lower than that of LIBs, thus resulting in a relatively low energy density of SIBs [179, 180]. However, due to the abundance of sodium resources and attractive cost-effectiveness [181], SIBs are promising to be utilized in some fields that do not require high energy density, such as large-scale energy storage [182, 183]. As a type of negative electrode for SIBs, transition metal sulfides exhibit high theoretical specific capacities and safe discharge voltage [184]. Nevertheless, large volume expansion and inferior charge transfer kinetics of transition metal sulfides greatly deteriorate their sodium storage performance [185]. Our group has been working on improving the electrochemical performance of transition metal compounds in the past few years [73, 117]. Recently, we proposed a general strategy for constructing $\text{Ti}_3\text{C}_2\text{T}_x$ MXene/transition metal sulfides ($\text{Ti}_3\text{C}_2\text{T}_x/\text{MS}_y$, $\text{T} = -\text{O}$ and $-\text{Cl}$, $\text{M} = \text{Fe}$, Co and Ni)

heterostructures as SIBs anodes through directly sulfurizing Lewis acidic etching products (MXenes/metal composites) (Fig. 11a–b) [147]. Different from the traditional construction process of preparing MXene first, then adsorbing transition metal ions and finally vulcanizing, this strategy simplifies the preparation procedure of MXene/transition metal sulfides hybrids via rationally utilizing Lewis acidic etching products. Additionally, this fabrication process avoids the use of HF as etchant and water as reaction medium, which effectively improves the experimental safety and alleviates the oxidation of MXene, respectively. For the fabricated $\text{Ti}_3\text{C}_2\text{T}_x/\text{FeS}_2$ heterostructures, FeS_2 nanoparticles are in-situ grown and tightly fixed on the $\text{Ti}_3\text{C}_2\text{T}_x$ MXene substrate (Fig. 11c–d), demonstrating a stable framework for continuous Na^+ insertion/extraction. Furthermore, $\text{O} 1s$ XPS spectrum and theoretical calculations confirm that $\text{Ti}_3\text{C}_2\text{T}_x$ MXene and FeS_2 nanoparticles demonstrate interfacial electronic coupling

effect via $\text{Ti}-\text{O}-\text{Fe}$ bonds (Fig. 11e–f), facilitating the rapid interfacial electron transfer from MXene to FeS_2 . Additionally, $\text{Ti}_3\text{C}_2\text{T}_x/\text{FeS}_2$ hybrids also exhibit rapid Na^+ diffusion kinetics and mechanical strain release channels. Consequently, derived from the above advantages, the $\text{Ti}_3\text{C}_2\text{T}_x/\text{FeS}_2$ anode delivers a reversible capacity of 474.9 mAh g^{-1} after 600 cycles at 5 A g^{-1} (Fig. 11g), and reveals a high capacity of 456.6 mAh g^{-1} at 10 A g^{-1} , suggesting outstanding long-term cyclic performance and rate capability. In addition, the full-cell device assembled with $\text{Ti}_3\text{C}_2\text{T}_x/\text{FeS}_2$ anode and $\text{Na}_3\text{V}_2(\text{PO}_4)_3$ cathode can demonstrate a discharge capacity of 431.6 mAh g^{-1} after 1000 cycles at 3 A g^{-1} and an energy density of around 130 Wh kg^{-1} at a power density of 415 W kg^{-1} , indicating superior application prospect of $\text{Ti}_3\text{C}_2\text{T}_x/\text{FeS}_2$ heterostructures.

Copper sulfide (CuS), as another common transition metal sulfide, also possesses high theoretical capacity and low

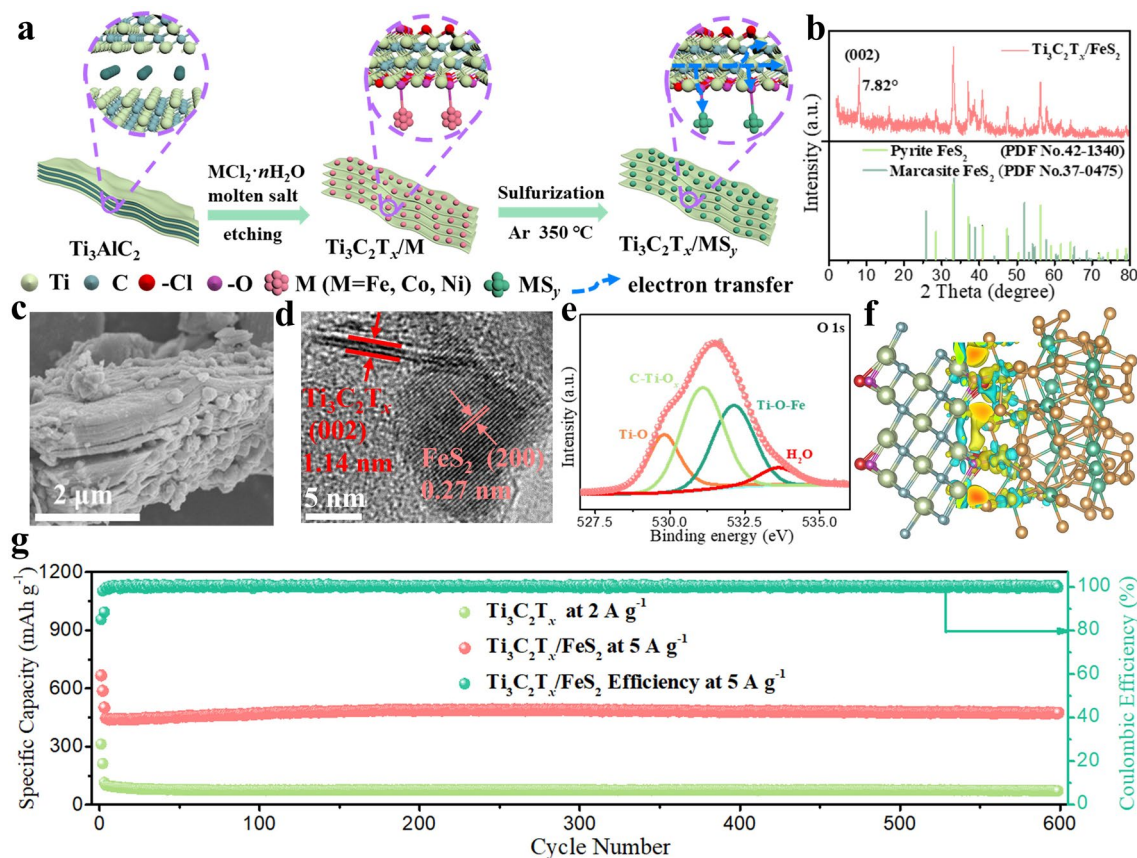


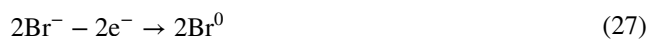
Fig. 11 a Schematic of the fabrication process of $\text{Ti}_3\text{C}_2\text{T}_x/\text{MS}_y$ hybrids. b XRD pattern of $\text{Ti}_3\text{C}_2\text{T}_x/\text{FeS}_2$ composites. c SEM image of $\text{Ti}_3\text{C}_2\text{T}_x/\text{FeS}_2$ hybrids. d HRTEM image of $\text{Ti}_3\text{C}_2\text{T}_x/\text{FeS}_2$. e $\text{O} 1s$ XPS spectra of $\text{Ti}_3\text{C}_2\text{T}_x/\text{FeS}_2$. f Charge density difference of $\text{Ti}_3\text{C}_2\text{T}_x/\text{FeS}_2$ composites. g Cyclic performance of $\text{Ti}_3\text{C}_2\text{T}_x$ MXene and $\text{Ti}_3\text{C}_2\text{T}_x/\text{FeS}_2$ hybrids at various current densities. Reproduced with permission from [147] Copyright 2022, Wiley–VCH

price, and has been widely studied as anode for SIBs. However, electrode pulverization and inferior electrochemical reaction kinetics have an adverse effect on its performance [186]. In order to improve the sodium storage performance of CuS, our group readily fabricated $\text{Ti}_3\text{C}_2\text{T}_x/\text{CuS}$ hybrids ($T = -\text{O}$ and $-\text{Cl}$) via $\text{CuCl}_2 \cdot 2\text{H}_2\text{O}$ etching and following in-situ sulfurization treatment [148]. The construction process also achieves the effective application of Lewis acidic molten salts etching products. Plenty of CuS nanoparticles are distributed among the $\text{Ti}_3\text{C}_2\text{T}_x$ MXene substrate, and they are connected by Ti–O–Cu covalent bonds. Benefiting from the extremely boosted electron transfer and Na^+ migration, enhanced sodium adsorption and structural integrity, the obtained $\text{Ti}_3\text{C}_2\text{T}_x/\text{CuS}$ anode delivers stable long-term cyclic performance with a discharge capacity of 347 mAh g^{-1} after 800 cycles at 3 A g^{-1} and wonderful rate performance with a high capacity of 346.3 mAh g^{-1} at 8 A g^{-1} . More importantly, the constructed SIBs full cell with $\text{Na}_3\text{V}_2(\text{PO}_4)_3$ cathode and $\text{Ti}_3\text{C}_2\text{T}_x/\text{CuS}$ anode reveals a capacity of 189.6 mAh g^{-1} after 800 cycles at 2 A g^{-1} . In the above-mentioned two works, MXene/transition metal sulfide heterostructures are efficiently constructed by rationally utilizing Lewis acidic etching products, namely MXenes/metal composites, which fully reflects the great advantages of Lewis acidic etching relative to other etching methods.

4.1.3 Zinc-Ion Batteries

Due to the flammability of organic electrolyte, LIBs and SIBs systems possess inevitable potential safety hazards, resulting in the combustion of electric vehicles and large-scale energy storage devices from time to time in the past few years [187]. Therefore, ZIBs system has recently attracted considerable attention owing to the use of aqueous electrolyte, which possesses high safety and low price [188, 189]. Additionally, ZIBs also demonstrate other important merits, such as high eco-efficiency and ionic conductivity of approximately 1 S cm^{-1} [190]. The halogen electrodes including Br_2 and I_2 exhibit conversion reaction mechanism and high theoretical specific capacities, and have been widely investigated as cathode materials for ZIBs [191–193]. Fortunately, the MXenes obtained by Lewis acidic etching can be endowed with $-\text{Br}$ or $-\text{I}$ functional groups, so it is necessary to investigate their zinc storage performance (Fig. 12a). In 2021, Li et al. prepared Ti_3C_2 MXene with

$-\text{Cl}$, $-\text{Br}$ and $-\text{I}$ functional groups through CuCl_2 , CuBr_2 and CuI etching, respectively [123]. When applied as cathodes for ZIBs, the $\text{Ti}_3\text{C}_2\text{Br}_2$ and $\text{Ti}_3\text{C}_2\text{I}_2$ MXenes exhibit obvious redox peaks in CV profiles and flat discharge–charge plateaus in galvanostatic charge–discharge curves, while $\text{Ti}_3\text{C}_2\text{Cl}_2$ MXene shows no redox peaks and oblique charge–discharge curves. The conversion reaction process of $\text{Ti}_3\text{C}_2\text{Br}_2$ and $\text{Ti}_3\text{C}_2\text{I}_2$ MXene is illustrated as follows:



In contrast, the Cl^- anions in $\text{Ti}_3\text{C}_2\text{Cl}_2$ MXene will lose electrons and turn into Cl_2 gas, which may escape from the MXene interlayer, making this conversion reaction irreversible. Consequently, $\text{Ti}_3\text{C}_2\text{Br}_2$ and $\text{Ti}_3\text{C}_2\text{I}_2$ MXene demonstrate energy densities of 129 and 135.6 Wh kg^{-1} , respectively, which is significantly higher than that of $\text{Ti}_3\text{C}_2\text{Cl}_2$ MXene. This work realizes the application of halogen terminations for the first time, and also suggests that the electrochemical performance of MXenes can be greatly improved by regulating the surface groups.

It is worth mentioning that the reaction mechanism of above-mentioned $\text{Ti}_3\text{C}_2\text{I}_2$ MXene is still stopping at individual I^-/I^0 redox pair, thus resulting in a low discharge voltage of around 1.3 V when used as ZIBs cathode. If the I^0/I^+ redox pair can be activated, the discharge voltage can be further increased. However, I^+ cations are unstable in common electrolytes such as ZnSO_4 solution. In order to solve this issue, Li et al. first synthesized $\text{Ti}_3\text{C}_2\text{I}_2$ MXene via CuI etching and then chose electrolyte system that contains electronegative F^- or Cl^- anions, which can considerably stabilize the I^+ cations during the cycling process [194]. Specifically, once I^+ cations are generated, F^- or Cl^- anions can combine with them, making I^+ cations exist stably, which can be effectively confirmed by the peak at 200 cm^{-1} in the in-situ Raman spectra of the $\text{Ti}_3\text{C}_2\text{I}_2$ MXene (Fig. 12b). Therefore, the I^0/I^+ redox pair are successfully activated in $\text{ZnCl}_2 + \text{KCl}$ electrolyte and a higher reduction peak at 1.66 V can be observed (Fig. 12c). As expected, $\text{Ti}_3\text{C}_2\text{I}_2$ MXene in $\text{ZnCl}_2 + \text{KCl}$ electrolyte affords a large discharge capacity of 207 and 126 mAh g^{-1} at a current density of 0.5 and 5 A g^{-1} , respectively, showing superior rate performance. Additionally, outstanding cyclic stability can be delivered for $\text{Ti}_3\text{C}_2\text{I}_2$ MXene with

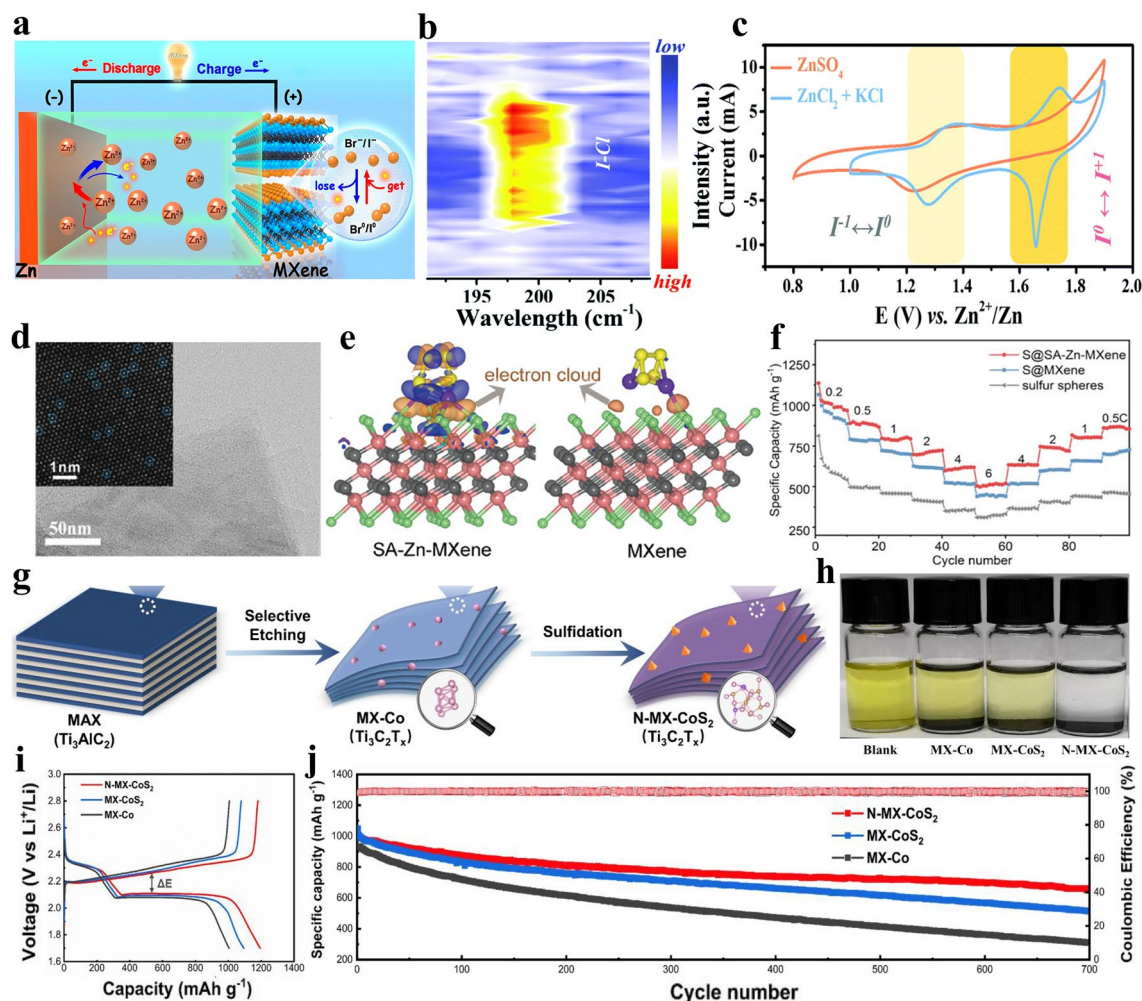


Fig. 12 **a** Schematic diagram of the working mechanism of Zn/halogenated Ti_3C_2 MXene cells. Reproduced with permission from [123] Copyright 2021, American Chemical Society. **b** In-situ Raman spectra of the $\text{Ti}_3\text{C}_2\text{I}_2$ cathode around 200 cm^{-1} . **c** CV curves of $\text{Ti}_3\text{C}_2\text{I}_2$ cathode in $\text{ZnCl}_2 + \text{KCl}$ electrolyte or conventional ZnSO_4 electrolyte. Reproduced with permission from [194] Copyright 2021, Royal Society of Chemistry. **d** HAADF-STEM image of SA-Zn-MXene. **e** Charge density difference for Li_2S_4 polysulfides adsorbed on SA-Zn-MXene and MXene. **f** Rate capabilities of S, S@MXene and S@SA-Zn-MXene. Reproduced with permission from [157] Copyright 2020, Wiley-VCH. **g** Schematic of the preparation process of N-MX- CoS_2 hybrids. **h** Adsorption test of MX-Co, MX- CoS_2 and N-MX- CoS_2 . **i** Galvanostatic charge-discharge curves of Li-S batteries with various materials-modified separator at 0.2C. **j** Long-term cyclic stability of Li-S batteries with various materials-treated separators at 1 C. Reproduced with permission from [146] Copyright 2021, Elsevier

approximately 80% capacity retention after 2800 cycles. The excellent zinc storage performance is attributed to the rapid electron/ Zn^{2+} transfer kinetics and strong confinement effect of MXene that prevents interlayer iodine active species from escaping to the outside. In short, the additional high discharge plateau at 1.65 V endows $\text{Ti}_3\text{C}_2\text{I}_2$ MXene with a large energy density of 280 Wh kg^{-1} . The above two works indicate that MXenes prepared by Lewis acidic molten salts etching has broad development space in aqueous ZIBs.

4.1.4 Lithium-Sulfur Batteries

Li-S batteries have received extensive attention since its birth in 1962. Compared with LIBs, SIBs and ZIBs systems, Li-S batteries demonstrate a very high theoretical energy density of 2600 Wh kg^{-1} and have been regarded as one of the most promising energy storage devices in the future [195, 196]. However, ultralow electronic conductivity of sulfur ($10^{-30}\text{ S cm}^{-1}$) and Li_2S , sluggish reaction kinetics, severe shuttle effect of LiPSs and low utilization rate of sulfur

result in inferior rate performance and cyclic durability [197]. Luckily, MXenes are expected to improve the electrochemical performance of Li–S batteries owing to their metallic conductivity, chemical adsorption ability, catalytic effect and structural diversity [198, 199]. In 2020, single atom zinc implanted $\text{Ti}_3\text{C}_2\text{T}_x$ MXene (SA-Zn-MXene) as sulfur host was successfully fabricated via ZnCl_2 etching of Ti_3AlC_2 MAX [157]. They found that Zn^{2+} cations in ZnCl_2 molten salt can not only react with the interlayer Al atoms, but also replace a few Ti species in MXene lattice during the etching process, which can be further confirmed by the bright dots corresponding to Zn atoms in HAADF-STEM image (Fig. 12d). On one hand, the SA-Zn-MXene exhibits strong interaction with Li_2S_4 polysulfides (Fig. 12e), and can catalyze the polysulfides transformation by decreasing the reaction barriers. On the other hand, the nucleation of $\text{Li}_2\text{S}_2/\text{Li}_2\text{S}$ can be significantly boosted by Zn atoms in MXene lattice. Additionally, the large volume variation of sulfur upon cycling can be accommodated by flexible $\text{Ti}_3\text{C}_2\text{T}_x$ MXene. Consequently, the S@SA-Zn-MXene electrode exhibits the lowest overpotential of 23 mV and superior rate performance with a high capacity of 517 mAh g^{-1} at 6C (Fig. 12f). More importantly, the enhanced cyclic stability can be obtained for S@SA-Zn-MXene, which delivers a discharge capacity of 706 mAh g^{-1} after 400 cycles at 1C.

Polar metal compounds including metal oxides, metal sulfides, metal selenides, metal nitrides, metal borides and metal phosphides have been considered as effective electrocatalysts to accelerate reaction kinetics of LiPSs [200–202]. In 2022, Yang et al. obtained N-doped $\text{Ti}_3\text{C}_2\text{T}_x$ MXene- CoS_2 heterostructure (N-MX- CoS_2) via CoCl_2 etching and subsequent in-situ sulfidation treatment with thiourea as sulfur source (Fig. 12g), and then utilized N-MX- CoS_2 as a bifunctional catalyst to modify the commercial separator [146]. The N element can be doped into the hybrids during the process of thiourea pyrolysis, which can be proved by the existence of N–C and Ti–N peaks in XPS spectra. This strategy enables CoS_2 nanoparticles to be tightly anchored among the MXene substrate. In the N-MX- CoS_2 hybrids, the N atoms and polar CoS_2 nanoparticles can form strong chemical interaction with LiPSs and provide rich catalytic sites to facilitate LiPSs conversion reaction. The $\text{Ti}_3\text{C}_2\text{T}_x$ MXene with metallic-level conductivity can further promote sulfur redox reaction kinetics. Since N-MX- CoS_2 heterostructure possesses dual functions of adsorption and catalysis, the shuttle effect of LiPSs can be effectively inhibited

and polarization can be greatly decreased (Fig. 12h–i). Finally, the batteries with modified separator deliver superior rate performance (775 mAh g^{-1} at 4C) and excellent long-term cycling stability with a low decay rate of 0.052% per cycle (651 mAh g^{-1} after 700 cycles at 1C and 721.6 mAh g^{-1} after 400 cycles at 2C) (Fig. 12j). To our relief, a series of MXenes/metal compound composites with strong binding energy can also be synthesized via Lewis acidic etching route, which is worthy of in-depth exploration and may provide new inspiration to the further development of Li–S batteries.

4.1.5 Metal Anodes-Based Batteries

Metal anodes including Li, Na, K, Al, Mg and Zn have been intensively investigated in high-performance secondary metal batteries in the past few decades owing to their low plating/stripping potentials and high theoretical specific capacities, thus leading to high energy densities [203–206]. Nevertheless, there are some key factors that deteriorate the electrochemical performance of metal anodes. First, the uneven deposition of metals during the discharge process will contribute to the uncontrolled growth of dendrites, which can pierce the separator and result in the short-circuit of cells. Then, the nearly infinite volume expansion leads to the rupture of solid electrolyte interphase (SEI) layer. In addition, the side reactions and the formation of “dead metal” will continuously consume the electrolyte and metal sources. Consequently, metal anodes generally demonstrate low coulombic efficiency, short cycle life and serious safety hazards [207, 208]. Some common strategies such as optimizing electrolyte composition, building artificial SEI film and fabricating three-dimensional robust frameworks have been utilized to enhance the performance of metal anodes [209]. Fortunately, MXenes with high electronic conductivity, low ion migration barrier, unique layered structure and sufficient functional groups can greatly facilitate the plating/stripping kinetics, effectively preventing the dendrite growth [15, 210].

For example, single zinc atoms immobilized $\text{Ti}_3\text{C}_2\text{Cl}_x$ MXene (Zn-MXene) as a host for lithium metal was reported through ZnCl_2 molten salts etching (Fig. 13a–b), and the content of Zn monoatoms is around 0.87 at% [156]. It is worth mentioning that sufficient reaction time is conducive to the substitution of Zn for Ti. Due to the lithiophilic

nature of Zn, the lithium metal can preferentially nucleate around the single atom Zn sites on the surface of $\text{Ti}_3\text{C}_2\text{Cl}_x$ MXene. When the plating level increases to $5 \mu\text{Ah cm}^{-2}$, a flat and smooth morphology can be obtained (Fig. 13c). Furthermore, Li metal grows vertically along the nucleation site to form a bowl-shaped lithium at higher deposition amounts (Fig. 13d–e), finally achieving dendrite-free Li metal anode. Therefore, Zn-MXene films can exhibit a low nucleation overpotential of 11.3 mV for half battery and a long cycle life of 1200 h for symmetric cells at 1 mA cm^{-2} with a fixed capacity of 1 mAh cm^{-2} . In addition, the Zn-MXene//LiFePO₄ full cell delivers a high capacity of 150

mAh g^{-1} at 0.5C and superior cyclic stability with a capacity of about 100 mAh g^{-1} after 500 cycles at 10C.

In recent years, MXenes have attracted extensive attention in inhibiting the growth of Zn dendrites due to their superior lattice matching [211]. More importantly, the surface groups of MXenes are considered to affect the adsorption energy and migration kinetics of Zn^{2+} ions. Based on this point, Li et al. reported the synthesis of various halogenated MXenes including $\text{Ti}_3\text{C}_2\text{Cl}_2$, $\text{Ti}_3\text{C}_2\text{Br}_2$ and $\text{Ti}_3\text{C}_2\text{I}_2$ MXene as interface layers via corresponding Lewis acidic molten salts etching to regulate the Zn deposition [212]. They found that above-mentioned halogenated MXenes possess

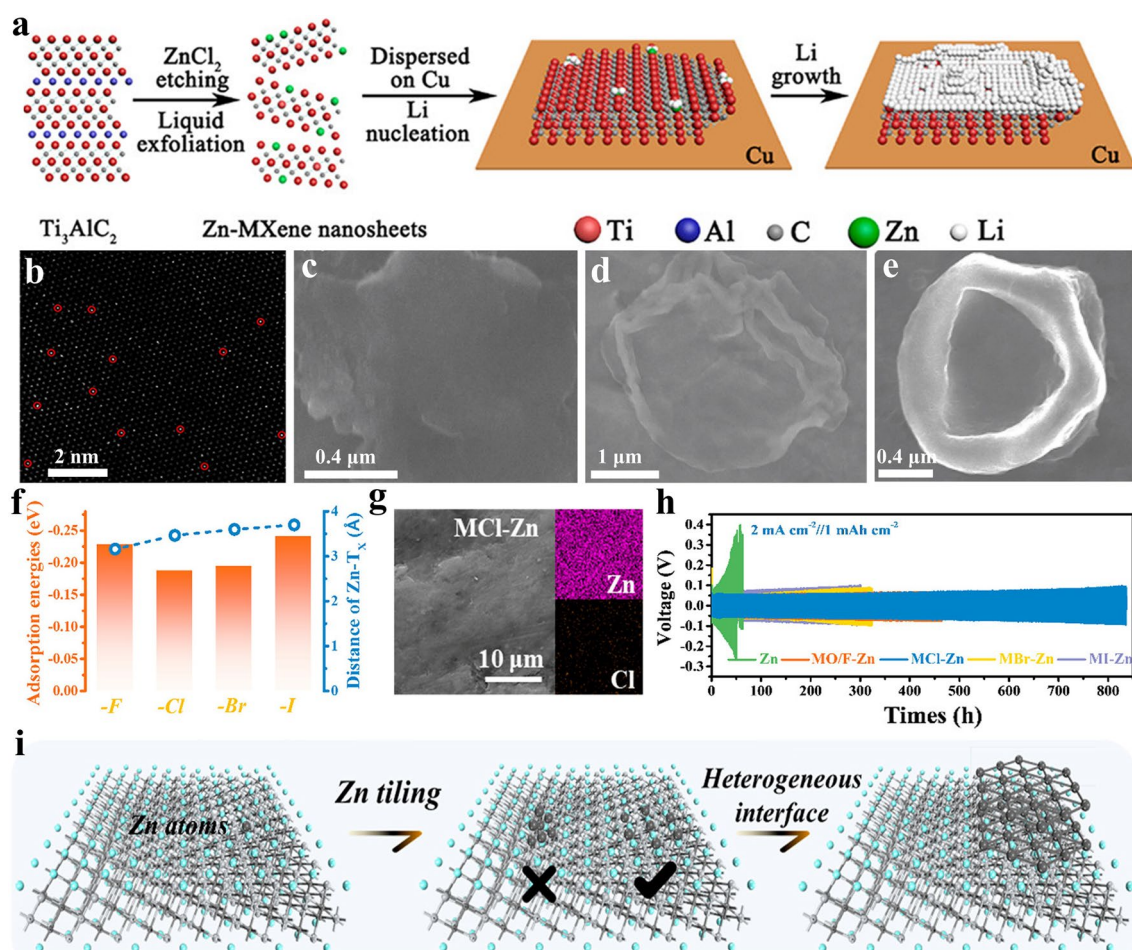


Fig. 13 **a** Schematic showing the preparation of Zn-MXene for Li nucleation and growth. **b** HAADF-STEM image of Zn-MXene nanosheets. **c–e** SEM images of Zn-MXene nanosheets after Li plating with capacities of 5, 20 and $60 \mu\text{Ah cm}^{-2}$, respectively. Reproduced with permission from [156] Copyright 2020, American Chemical Society. **f** Calculated atomic distance between Zn atom and neighboring halogen termination as well as Zn adsorption energies of different MXene surfaces. **g** SEM image and EDS mapping of the $\text{Ti}_3\text{C}_2\text{Cl}_2$ -Zn electrode after cycling. **h** Long-term cyclic performance of various symmetric cells. **i** Schematic diagram of the Zn deposition process on the MXene substrate. Reproduced with permission from [212] Copyright 2021, American Chemical Society

metallic-level conductivities and good affinity to Zn metal via theoretical simulation (Fig. 13f), which is conducive to the deposition of Zn^{2+} ions. Consequently, Zn^{2+} ions tend to grow horizontally rather than vertically under the regulation of outermost halogen surface groups, which effectively inhibits the disordered growth of Zn metal at the beginning. Subsequently, the constructed coherent heterogeneous interface induces the uniform deposition of Zn metal (Fig. 13i). As expected, the obtained halogenated MXene-Zn anode exhibits better electrochemical performance than bare Zn metal anode. Among the MXenes with $-\text{Cl}$, $-\text{Br}$ or $-\text{I}$ terminations, the $-\text{Cl}$ functionalized Ti_3C_2 MXene-Zn anode possesses the strongest ability to inhibit the growth of Zn dendrites derived from its medium adsorption and diffusion for Zn^{2+} . Consequently, $\text{Ti}_3\text{C}_2\text{Cl}_2$ -Zn electrode exhibits a flat and smooth surface after cycling, and a cycle life of 840 h at 2 mA cm^{-2} with a fixed capacity of 1 mAh cm^{-2} for symmetric cells (Fig. 13g–h). Finally, the $\text{Ti}_3\text{C}_2\text{Cl}_2$ -Zn// $\text{Ti}_3\text{C}_2\text{I}_2$ full cell demonstrates superior long-term cyclic stability up to 9,000 cycles, which is better than that of Zn// $\text{Ti}_3\text{C}_2\text{I}_2$ battery. The above two works indicate that MXenes obtained by Lewis acidic etching have a good induction effect on the uniform growth of metal anodes.

4.1.6 Dual-Ion Batteries

As a novel battery concept, the dual-ion batteries (DIBs) demonstrate a brand-new working mechanism, which is realized by intercalating the anions and cations of electrolyte into respective electrodes. In general, DIBs possess some advantages such as high theoretical energy density, low cost and long cycle life [213]. Nevertheless, low anode specific capacity of DIBs still remains a big problem. MXenes, as a type of 2D layered material, have abundant nano-level channels to allow the insertion and de-insertion of ions and can be regarded as electrodes for DIBs. In 2022, $\text{Ti}_3\text{C}_2\text{Cl}_2$ MXene with adjustable in-plane porosity was obtained by eutectic molten salts ($\text{NaCl}/\text{ZnCl}_2$) etching (Fig. 14a) [113]. The formation mechanism of in-plane pore has been discussed previously in detail. Specifically, the surface area and mesoporous volume of $\text{Ti}_3\text{C}_2\text{Cl}_2$ MXene increase gradually with the rise of NaCl content in $\text{ZnCl}_2/\text{NaCl}$ mixture (Fig. 14b–e), which can create more active sites and benefit the Li^+ migration. For example, when the mole percent of NaCl in $\text{ZnCl}_2/\text{NaCl}$ mixture is 60%, the obtained

$\text{Ti}_3\text{C}_2\text{Cl}_2$ -60 MXene delivers a specific surface area of $85 \text{ m}^2 \text{ g}^{-1}$ and pore size concentrates on 3–4 nm. Additionally, $\text{Ti}_3\text{C}_2\text{Cl}_2$ -60 demonstrates superior TiC_6 octahedral core symmetry and low Li^+ migration kinetics. Consequently, the $\text{Ti}_3\text{C}_2\text{Cl}_2$ -60 MXene as LIBs anode delivers a discharge capacity of 382 mAh g^{-1} at 0.1 A g^{-1} . Further, when paired with graphite cathode, $\text{Ti}_3\text{C}_2\text{Cl}_2$ -60/graphite DIBs afford a high discharge capacity of 242 mAh g^{-1} at 0.1 A g^{-1} (Fig. 14f), and the superior cyclic stability with 83% capacity retention can also be obtained (141 mAh g^{-1} after 1000 cycles at 1 A g^{-1}), demonstrating excellent electrochemical performance. The in-plane porous MXene produced by Lewis acidic molten salts etching can also be utilized in other fields such as catalysis.

4.1.7 Supercapacitors

SCs store and release energy through the physical adsorption and desorption of electrolyte ions on the electrode surface, and show higher energy density compared with common capacitors [214]. Up to now, SCs have been regarded as a reliable and promising energy storage device due to high power density, environmental friendliness and high safety [215]. MXenes become one of the best electrodes for SCs owing to the moderate specific area, high electronic conductivity, rich ion diffusion channels and large faradaic pseudocapacitance [28, 216]. MXene was first used as electrode material for SCs in 2013 [217]. Yury et al. reported the synthesis of a series of cations (Li^+ , Na^+ , K^+ , NH_4^+ and Mg^{2+})-intercalated $\text{Ti}_3\text{C}_2\text{T}_x$ MXene, and a volumetric capacitance of 350 F cm^{-3} can be obtained in KOH electrolyte, which is better than that of traditional porous carbon. Later, freestanding $\text{Ti}_3\text{C}_2\text{T}_x$ films prepared by LiF/HCl etching exhibit a high volumetric capacitance of 900 F cm^{-3} at 2 mV s^{-1} in H_2SO_4 electrolyte [65]. Recently, MXenes synthesized by Lewis acidic etching have also been investigated as electrode materials for SCs. For example, Ti_3C_2 -Cu composites was prepared by $\text{CuCl}_2 \cdot 2\text{H}_2\text{O}$ Lewis acidic salts etching in 2021, and the Cu nanoparticles are tightly anchored on the $\text{Ti}_3\text{C}_2\text{T}_x$ MXene via Ti–O–Cu interfacial bond [122]. Previous studies have shown that O-terminated MXenes exhibit high capacitance due to the easy absorption of H^+ by $-\text{O}$ functional group. The Ti_3C_2 -Cu electrode is able to deliver a capacitance of 885 F g^{-1} at 0.5 A g^{-1} in H_2SO_4 electrolyte. Additionally, the symmetric SCs based



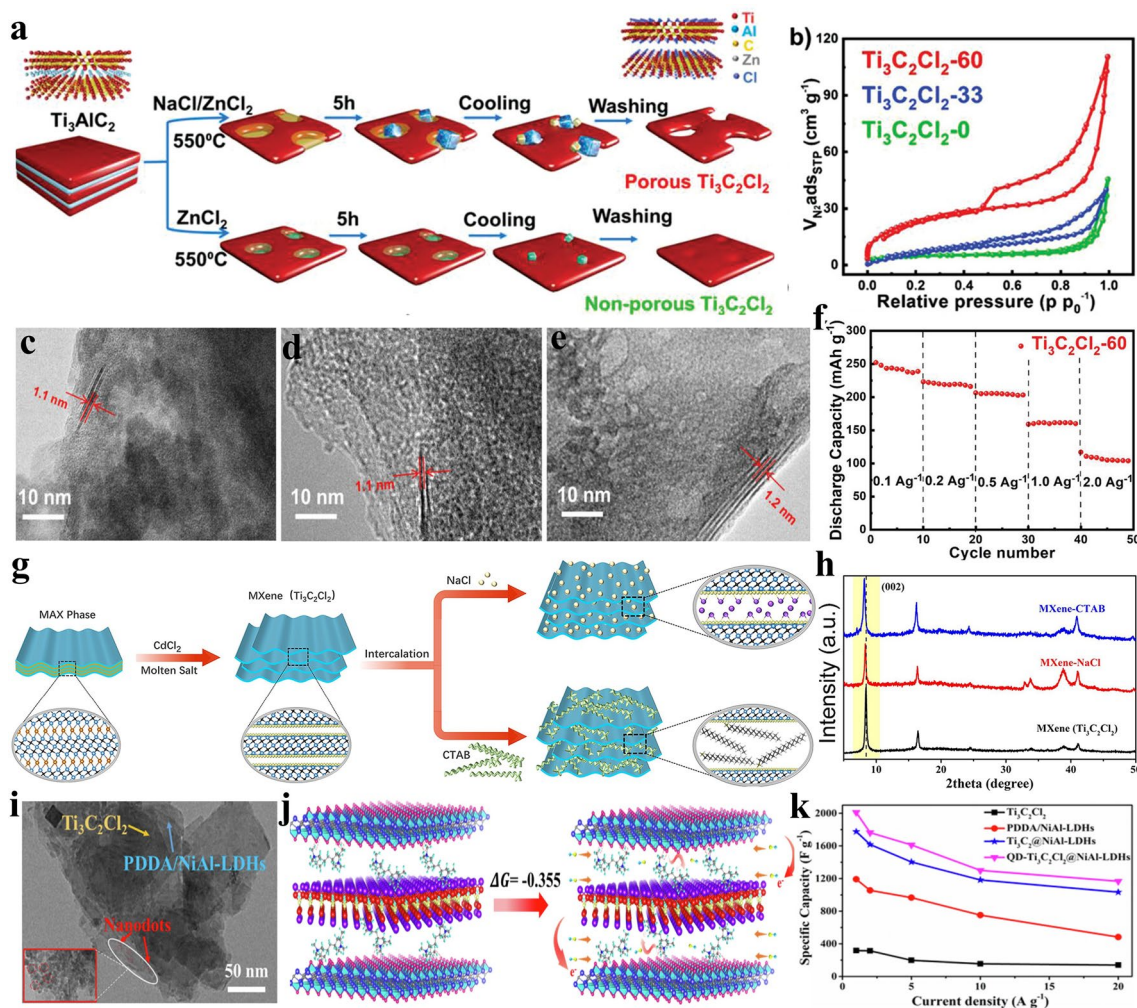


Fig. 14 **a** Schematic showing the preparation of in-plane porous $\text{Ti}_3\text{C}_2\text{Cl}_2$ MXene via eutectic etching. **b** N_2 adsorption–desorption isotherms of various MXenes. TEM images of $\text{Ti}_3\text{C}_2\text{Cl}_2$ MXene obtained by eutectic etching with **c** 0%, **d** 33% and **e** 60% NaCl mole percent in the NaCl/ZnCl₂ mixture. **f** Rate performance of $\text{Ti}_3\text{C}_2\text{Cl}_2$ -60/graphite DIBs. Reproduced with permission from [113] Copyright 2021, Wiley–VCH. **g** Schematic demonstrating the preparation of MXene-NaCl and MXene-CTAB. **h** XRD patterns of MXene-NaCl and MXene-CTAB. Reproduced with permission from [219] Copyright 2021, Elsevier. **i** HRTEM image of QD- $\text{Ti}_3\text{C}_2\text{Cl}_2$ @NiAl-LDHs composites. **j** The free energy diagram of pseudocapacitive process on the QD- $\text{Ti}_3\text{C}_2\text{Cl}_2$ @NiAl-LDHs. **k** Specific capacities of the various electrodes at different current densities. Reproduced with permission from [222] Copyright 2021, Elsevier

on Ti_3C_2 -Cu achieve a high areal energy density of $103.3 \mu\text{Wh cm}^{-2}$ at 0.8 mW cm^{-2} . The superior electrochemical performance of Ti_3C_2 -Cu electrode is mainly attributed to high content of -O termination, high pseudocapacitive contribution of Cu nanoparticles, boosted charge/mass transfer kinetics and strong interaction between MXene and Cu.

Later, Khan et al. synthesized $\text{Ti}_3\text{C}_2\text{Cl}_2$, $\text{Ti}_3\text{C}_2\text{Br}_2$ and $\text{Ti}_3\text{C}_2\text{I}_2$ MXene via CuCl_2 , CuBr_2 and CuI molten salts etching, respectively [218]. When used as electrode materials for SCs in 3 M H_2SO_4 electrolyte, typical pseudocapacitive-shaped CV curves can be obtained and a specific capacity of

92, 29 and 63 C g^{-1} can be afforded for $\text{Ti}_3\text{C}_2\text{Cl}_2$, $\text{Ti}_3\text{C}_2\text{Br}_2$ and $\text{Ti}_3\text{C}_2\text{I}_2$ MXene at 5 mV s^{-1} . Further, the capacity retention ratio can reach as high as 85.22% after 10,000 cycles at 1.4 A g^{-1} for $\text{Ti}_3\text{C}_2\text{I}_2$ electrode, suggesting outstanding long-term cyclic stability. The excellent electrochemical performance of -F, -Br or -I functionalized MXene mainly benefits from the high electrochemical activity of corresponding halogen surface groups. In order to further improve the performance of MXenes produced by Lewis acidic etching, several common and effective strategies such as tuning the interlayer spacing and compositing MXene with other

electroactive materials have been proposed by researchers. For example, Zhang et al. reported the synthesis of $\text{Ti}_3\text{C}_2\text{Cl}_2$ MXene via CdCl_2 etching in 2022 and then increased the interlayer spacing of MXene by the intercalation of NaCl and cetyltrimethylammonium bromide (CTAB), respectively (Fig. 14g) [219]. As expected, large organic cation CTA^+ can greatly enlarge the interlayer spacing to 1.16 nm, while the small Na^+ cation-intercalated MXene shows a value of 1.14 nm (Fig. 14h). The large interlayer spacing of MXene-CTAB can increase the contact area between MXene and electrolyte, boost the ion diffusion kinetics and decrease the charge transfer resistance. Additionally, the CTA^+ cations can react with the ions between MXene layers, and effectively adsorb counter ions in the electrolyte to deliver additional specific capacitance. Consequently, the $\text{Ti}_3\text{C}_2\text{Cl}_2$ MXene-CTAB electrode can provide a higher capacitance of 258.28 F g^{-1} in $(\text{NH}_4)_2\text{SO}_4$ electrolyte than MXene- NaCl . The highest energy density of MXene-CTAB electrode can reach 11.48 Wh kg^{-1} at a power density of 200 W kg^{-1} . More importantly, $\text{Ti}_3\text{C}_2\text{Cl}_2$ MXene-CTAB exhibits superior cyclic durability with only 7% capacitance loss after 3000 cycles at 1.0 A g^{-1} , which is superior to that of $\text{Ti}_3\text{C}_2\text{Cl}_2$ MXene and $\text{Ti}_3\text{C}_2\text{Cl}_2$ MXene- NaCl .

LDHs have been regarded as promising electrode materials for SCs owing to their high specific capacitance and energy density [220]. However, low electronic conductivity of LDHs results in inferior rate capability and cyclic performance [221]. Hybridizing LDHs with highly conductive MXenes may lead to great improvement in electrode performance. In 2022, Zhao et al. firstly prepared $\text{Ti}_3\text{C}_2\text{Cl}_2$ MXene nanodots (QD- $\text{Ti}_3\text{C}_2\text{Cl}_2$) via CdCl_2 etching and subsequent hydrothermal reaction, and the nanodots are distributed on the surface of MXene nanosheets [222]. Then, the negatively-charged QD- $\text{Ti}_3\text{C}_2\text{Cl}_2$ can integrate with positively-charged NiAl-LDHs to electrostatically fabricate QD- $\text{Ti}_3\text{C}_2\text{Cl}_2$ @NiAl-LDHs composites, where the NiAl-LDHs nanosheets are dispersed on MXene nanosheets (Fig. 14i). Derived from the superior charge transfer kinetics of QD- $\text{Ti}_3\text{C}_2\text{Cl}_2$, a small band gap of 0.52 eV can be obtained for QD- $\text{Ti}_3\text{C}_2\text{Cl}_2$ @NiAl-LDHs, which is lower than that of NiAl-LDHs (1.51 eV), demonstrating enhanced electronic conductivity. Additionally, compared with NiAl-LDHs, QD- $\text{Ti}_3\text{C}_2\text{Cl}_2$ @NiAl-LDHs hybrids possess a higher specific area of $658.74 \text{ m}^2 \text{ g}^{-1}$ and lower Gibbs free energy of redox reaction (-0.355 eV) (Fig. 14j), greatly accelerating the mass transport and adsorption of active species. Therefore,

the obtained QD- $\text{Ti}_3\text{C}_2\text{Cl}_2$ @NiAl-LDHs electrode achieves a pretty high capacitance of 2010.8 F g^{-1} at 1.0 A g^{-1} (Fig. 14k), and excellent long-term cyclic performance with 94.1% capacitance retention after 10,000 cycles, which is better than those of NiAl-LDHs electrode. Additionally, a large energy density of 100.5 Wh kg^{-1} can be delivered for QD- $\text{Ti}_3\text{C}_2\text{Cl}_2$ @NiAl-LDHs at a power density of 299.8 W kg^{-1} . The above examples reveal that MXenes prepared by Lewis acidic etching are promising anodes for electrochemical energy storage systems.

4.2 Energy Conversion

Exploring renewable energy is one of the greatest challenges for the sustainable development of contemporary society. Advanced energy conversion systems such as photovoltaic electrodes, catalysis, and fuel cell, will play a crucial role in the future [223]. For example, photovoltaic devices such as silicon solar cells have been commercialized on a large scale and dominate the market in China, and perovskite solar cells (PSCs) are attracting increasing attention. Additionally, several common and classical catalysis reactions including hydrogen evolution reaction (HER), oxygen evolution reaction (OER), carbon dioxide reduction reaction (CO_2RR) and nitrogen reduction reaction (NRR) have also been widely investigated in the past decades [224].

4.2.1 Perovskite Solar Cells

Compared with silicon solar cells, PSCs possess the advantages of low cost, high absorption coefficient, easy preparation and high theoretical photoelectric conversion efficiency (PCE). In recent years, a high PCE value of 25.7% can be obtained for PSCs, which makes PSCs become one of the most promising photovoltaic devices in the near future [225]. However, defective interfaces and grain boundaries of PSCs greatly deteriorate device performance [226]. Recently, MXenes have been intensively researched in PSCs as additive, electrode or hole/electron transport layer owing to their high electrical conductivity and carrier mobility, adjustable work function, abundant surface functional groups and excellent mechanical property [227]. In 2021, Zhou et al. synthesized $\text{Ti}_3\text{C}_2\text{Cl}_x$ MXene suspension via CdCl_2 etching and following IPA intercalation, and the $\text{Ti}_3\text{C}_2\text{Cl}_x$ MXene as additive is then incorporated into the bulk and surface



of perovskite film (Fig. 15a–b) [159]. The peak shift in Pb 4f XPS spectrum indicates that the -Cl surface group with strong electron-withdrawing ability in $\text{Ti}_3\text{C}_2\text{Cl}_x$ MXene and the unsaturated Pb^{2+} in CsPbBr_3 can form Pb-Cl bond along the interface (Fig. 15c). The strong interaction between $\text{Ti}_3\text{C}_2\text{Cl}_x$ MXene and CsPbBr_3 can effectively relieve the lattice strain of perovskite (Fig. 15d), and the defects situated at the interface and grain boundaries can be healed. Therefore, a high PCE of 11.08% and open-circuit voltage of 1.702 V can be obtained for the fabricated all-inorganic CsPbBr_3 PSCs. More importantly, the $\text{Ti}_3\text{C}_2\text{Cl}_x$ -functionalized CsPbBr_3 devices exhibit outstanding long-term stability of

100 days under 80% relative humidity and 25 °C (Fig. 15e), demonstrating the high-quality of perovskite films.

Later, $\text{Ti}_3\text{C}_2\text{Cl}_x$ quantum dots ($\text{Ti}_3\text{C}_2\text{Cl}_x$ QDs) with an average size of around 8 nm were prepared through CuCl_2 etching, subsequent hydrothermal reaction and ultrasonication treatment (Fig. 15f) [228]. As followed, the $\text{Ti}_3\text{C}_2\text{Cl}_x$ QDs is introduced into the precursor solution to fabricate perovskite layer via one-step processing. Similarly, the -Cl functional groups in $\text{Ti}_3\text{C}_2\text{Cl}_x$ QDs can generate chemical bond with Pb^{2+} cations in $\text{Rb}_{0.05}\text{Cs}_{0.05}(\text{FA}_{0.83}\text{MA}_{0.17})_{0.90}\text{Pb}(\text{I}_{0.83}\text{Br}_{0.17})_3$ perovskite compound, which can also be confirmed by the peaks move

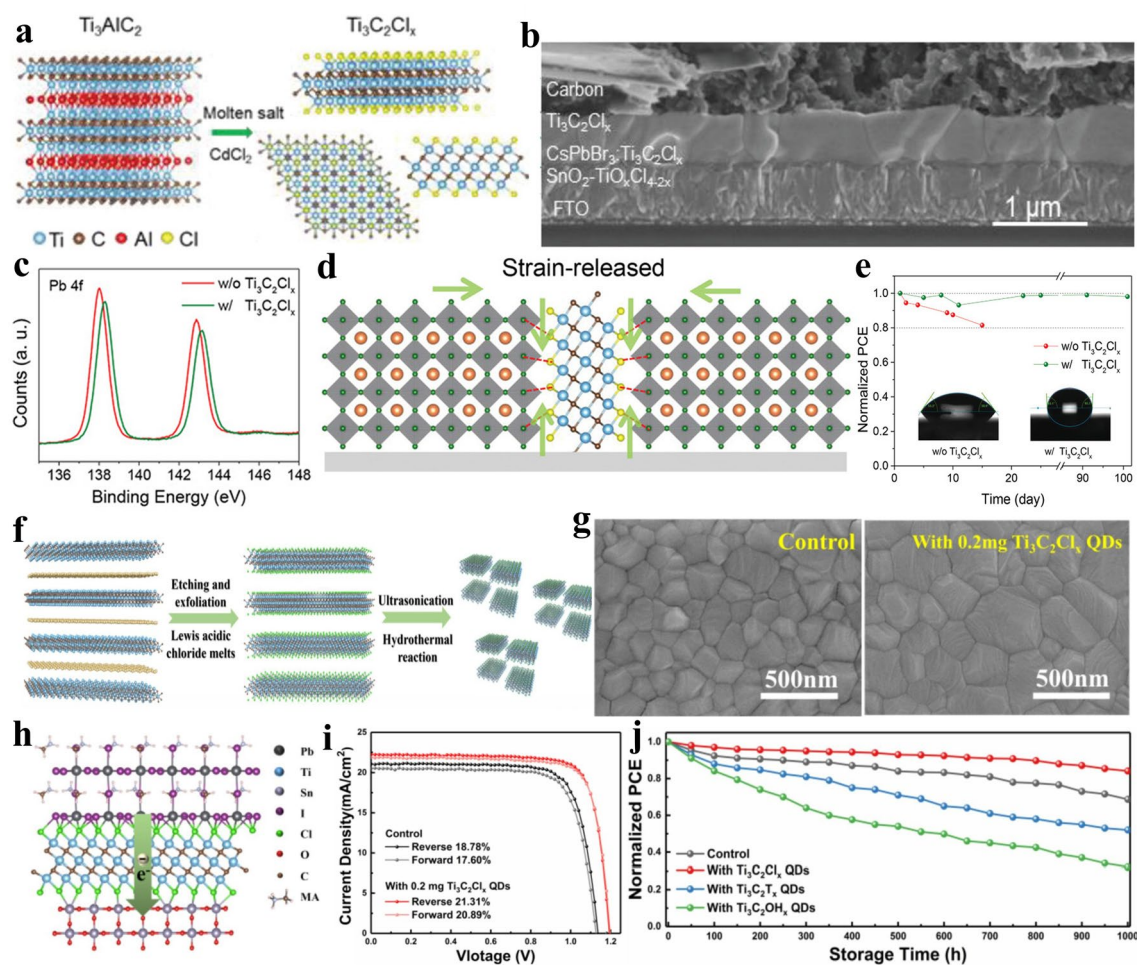


Fig. 15 **a** Schematic showing the preparation of $\text{Ti}_3\text{C}_2\text{Cl}_x$ MXene. **b** Cross-sectional SEM image of all-inorganic PSCs. **c** Pb 4f XPS spectra of CsPbBr_3 perovskite film. **d** Schematic of released strain in the CsPbBr_3 grains with $\text{Ti}_3\text{C}_2\text{Cl}_x$ MXene. **e** Long-term stability of the devices in air under 80% relative humidity and 25 °C. Reproduced with permission from [159] Copyright 2021, The Authors, published by Wiley–VCH. **f** Schematic demonstrating the preparation of $\text{Ti}_3\text{C}_2\text{Cl}_x$ QDs. **g** SEM images of pristine and $\text{Ti}_3\text{C}_2\text{Cl}_x$ QDs-modified perovskite films. **h** Schematic illustration of the perovskite- $\text{Ti}_3\text{C}_2\text{Cl}_x$ QDs- SnO_2 heterojunction. **i** Reverse and forward scans for the pristine and $\text{Ti}_3\text{C}_2\text{Cl}_x$ QDs-modified devices. **j** Normalized PCEs against storage time for the pristine and $\text{Ti}_3\text{C}_2\text{Cl}_x$ QDs-treated devices. Reproduced with permission from [228] Copyright 2021, Elsevier

in Pb 4f and Cl 2p XPS spectra. Additionally, scanning electron microscopy (SEM) images demonstrate that the perovskite grain size can be enlarged from 273 to 453 nm after the addition of $\text{Ti}_3\text{C}_2\text{Cl}_x$ QDs (Fig. 15g), reducing the number of grain boundary. The introduction of $\text{Ti}_3\text{C}_2\text{Cl}_x$ QDs acting as nucleation sites can effectively slow down the growth of perovskite crystal and the film crystallinity can be greatly enhanced with an optimized orientation, thus leading to fewer crystal distortion. Moreover, the interfacial charge transfer resistance between perovskite layer and SnO_2 electron transport layer can be greatly reduced owing to the highly conductive $\text{Ti}_3\text{C}_2\text{Cl}_x$, and the energy level alignment can be further improved (Fig. 15h). Consequently, the $\text{Ti}_3\text{C}_2\text{Cl}_x$ QDs-modified device can deliver a high PCE value of 21.31% and an open-circuit voltage of 1.19 V (Fig. 15i). Furthermore, the extraordinary long-term stability with 84% PCE retention after 1000 h storage time under 40% relative humidity can be afforded for $\text{Ti}_3\text{C}_2\text{Cl}_x$ QDs-modified device (Fig. 15j). The two works indicate that the Cl-terminated MXenes prepared by Lewis acidic etching has great potential to enhance the performance of PSCs devices.

4.2.2 Hydrogen Evolution Reaction

H_2 is regarded as a clean and renewable energy source that can replace fossil fuels in the future owing to its high heat value and pollution-free combustion product. The HER is an effective method to produce high-purity H_2 via water splitting [229]. Some noble catalysts such as Au, Pt and Pd have been widely used to accelerate the H_2 evolution kinetics and decrease overpotentials because of their high activities [230]. Nevertheless, high price and low reserve greatly impede the large-scale application of noble catalysts. In recent years, MXenes have been considerably researched as catalyst derived from their 2D layered structure, tailorable surface chemistry, diverse composition, high electrical conductivity and superior mechanical stability [231, 232]. Particularly, the polar terminations of MXenes can strongly interact with other materials to form high-performance catalysts. For example, Jiang et al. firstly synthesized Ti_3CNCl_2 MXene via NiCl_2 molten salt etching of Ti_3AlCN MAX. Then, $\text{Ti}_3\text{CNCl}_2@ \text{CoS}_2$ core-shell architecture as efficient HER catalyst can be obtained by hydrothermal

reaction [233]. Theoretical calculations reveal that electron can transfer from Ti_3CNCl_2 MXene to CoS_2 through -Cl functional group, demonstrating strong interaction between them. Additionally, the Gibbs free energy of H_2 adsorption of $\text{Ti}_3\text{CNCl}_2@ \text{CoS}_2$ hybrids is close to zero, indicating a strong catalytic activity. It is noteworthy that the electrons of $\text{Ti}_3\text{CNCl}_2@ \text{CoS}_2$ become more delocalized, which suggests that H^+ cations are easy to combine with electrons. As a result, benefiting from the synergistic effect of CoS_2 and highly-conductive Ti_3CNCl_2 , the constructed $\text{Ti}_3\text{CNCl}_2@ \text{CoS}_2$ hybrids deliver a low Tafel slope of 89 mV dec^{-1} and small charge transfer resistance in 0.5 M H_2SO_4 electrolyte. Moreover, boosted long-term stability can be obtained for $\text{Ti}_3\text{CNCl}_2@ \text{CoS}_2$, which can sustain catalytic activity for 10 h and the current density shows almost no attenuation.

4.2.3 Overall Water Splitting

Water splitting provides a simple, effective and promising method for H_2 and O_2 production, which can effectively solve the energy crisis [234]. In general, electrolysis of water is composed of HER at the cathode and the OER at the anode and requires a theoretical voltage of 1.23 V [235]. Nevertheless, the multi-electron reaction results in sluggish kinetics, which greatly limits the H_2 and O_2 production and increases the drive voltage [236]. Exploring high-performance electrocatalysts can effectively solve the above-mentioned issues. For example, Sarfraz et al. reported the synthesis of Cl-terminated $\text{Ti}_3\text{C}_2\text{Cl}_2$ MXene via CuCl_2 etching of Ti_3AlC_2 precursor in 2022, and $\text{Ti}_3\text{C}_2\text{Cl}_2$ MXene with obvious lamellar structure is then used as catalyst for water splitting in 1 M KOH solution [237]. Compared with $\text{Ti}_3\text{C}_2\text{T}_x$ MXene obtained by HF etching (HF- $\text{Ti}_3\text{C}_2\text{T}_x$ MXene), $\text{Ti}_3\text{C}_2\text{Cl}_2$ MXene possesses an enlarged interlayer spacing, more active sites and stable architecture. Therefore, $\text{Ti}_3\text{C}_2\text{Cl}_2$ electrode shows a smaller overpotential of 330 mV than HF- $\text{Ti}_3\text{C}_2\text{T}_x$ MXene (390 mV) at 30 mA cm^{-2} for OER. Similarly, a lower HER overpotential of 259 mV can be obtained for $\text{Ti}_3\text{C}_2\text{Cl}_2$ at 10 mA cm^{-2} , while HF- $\text{Ti}_3\text{C}_2\text{T}_x$ MXene demonstrates a large overpotential of 444 mV at the same current density. Notably, $\text{Ti}_3\text{C}_2\text{Cl}_2$ electrode exhibits a low Tafel slope of 48 and 92 mV dec^{-1} for OER and HER, respectively, indicating excellent catalytic activity for water splitting.

4.2.4 Carbon Dioxide Reduction Reaction

In recent years, the depletion of fossil fuels has produced a large amount of CO₂, leading to a huge impact on the environment, such as greenhouse effect and the extinction of some species [238]. Therefore, it is necessary to reduce CO₂ emission or find effective ways to use it. The CO₂RR is an effective and green method to convert CO₂ into high-value chemicals or fuels [239]. However, CO₂RR suffers from sluggish kinetics owing to the good stability of CO₂, and efficient catalysts are therefore required [240]. In 2021, Zhao et al. synthesized single atom Cu immobilized Ti₃C₂Cl_x MXene (SA-Cu-MXene) as CO₂RR electrocatalyst via ZnCl₂ molten salt etching of Ti₃(Al_{1-x}Cu_x)C₂ MAX (Fig. 16a) [158]. It is worth mentioning that the Cu atoms can be well preserved during the selective etching process. The content of Cu single atoms is approximately to be 1.0 wt% and many bright dots representing Cu atoms

can be observed in HAADF-STEM image (Fig. 16b). Additionally, XAS measurement indicates that Cu atoms are coordinated by –O surface groups of Ti₃C₂Cl_x MXene via Cu–O bond (Fig. 16c). Owing to the superior charge transfer kinetics of MXene and unsaturated electronic structure of Cu atoms, the obtained catalyst can greatly reduce the energy barrier from CO₂ to CH₃OH and deliver a maximum Faradaic efficiency value of 59.1% at –1.4 V (Fig. 16d–e), demonstrating outstanding catalytic capability. More importantly, a high Faradaic efficiency of over 58% can still be obtained after 30 h, which indicates enhanced stability.

4.2.5 Nitrogen Reduction Reaction

NH₃, as a particularly important chemical material, has played a key role in industry and agriculture. At present, large-scale NH₃ synthesis mainly relies on the traditional

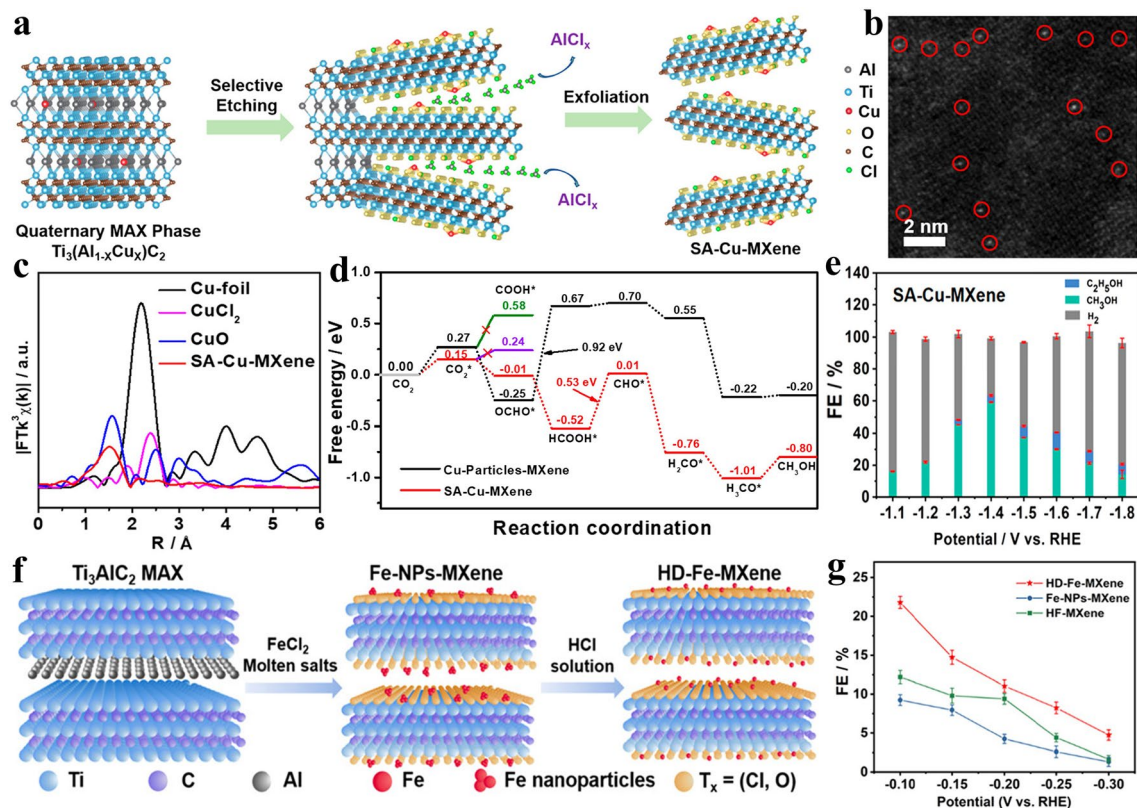


Fig. 16 **a** Schematic of the synthesis of SA-Cu-MXene. **b** HAADF-STEM image of SA-Cu-MXene. **c** XAS spectra of SA-Cu-MXene. **d** Free energy diagram of CO₂ to CH₃OH. **e** Faradaic efficiency of SA-Cu-MXene at various potentials. Reproduced with permission from [158] Copyright 2021, American Chemical Society. **f** Schematic of the preparation of HD-Fe-MXene. **g** Faradaic efficiency of different materials at various potentials. Reproduced with permission from [244] Copyright 2022, The Authors, published by Wiley–VCH

Haber–Bosch process, which requires to be carried out under high temperature and pressure (300–500 °C and 150–200 atm) [241]. In short, Haber–Bosch process not only consumes huge energy but also releases plenty of greenhouse gases into the atmosphere. The electrocatalytic NRR has attracted intensive attention as a green method to produce NH_3 at room temperature and atmospheric pressure [242]. Nevertheless, promising electrocatalysts with superior stability and high activity are also required to promote the NRR process, which suffers from a large overpotential and low yield of NH_3 owing to the strong $\text{N}\equiv\text{N}$ bond in N_2 [243]. For example, Wang et al. prepared highly dispersed Fe immobilized in fluorine-free $\text{Ti}_3\text{C}_2\text{T}_x$ MXene (HD-Fe-MXene) as NRR electrocatalyst in 0.1 M Na_2SO_4 electrolyte through FeCl_2 etching and HCl washing (Fig. 16f) [244]. The XRD pattern indicates that the formed Fe nanoparticles can be eliminated by HCl, and energy-dispersive spectroscopy and XPS analysis demonstrate that the remaining Fe atoms with a content of 3.12 wt% are highly anchored on the surface of $\text{Ti}_3\text{C}_2\text{T}_x$ MXene via Fe–O bond. Benefiting from the rich active sites and outstanding electrical conductivity of Fe atoms and fluorine-free $\text{Ti}_3\text{C}_2\text{T}_x$ MXene, the adsorption and activation of N_2 as well as charge transfer kinetics can be considerably improved. Consequently, the obtained electrocatalyst can afford a high NH_3 yield of $18.25 \mu\text{g h}^{-1} \text{mg}^{-1}$ and a Faradaic efficiency of 21.8% (Fig. 16g). Additionally, boosted stability with almost unchanged current density after 24 h testing can be obtained for HD-Fe-MXene electrode.

4.3 Sensors

In modern society, sensors play an increasingly significant role in environmental protection, disease detection and industrial production, etc. Currently, there are different types of sensors, such as gas sensors, biosensors and sound sensors [245]. Owing to the medium specific surface area, layered structure, rich active sites and superior electronic conductivity, MXenes have been regarded as promising sensitive materials in recent years [44]. For example, Wu et al. synthesized $\text{Ti}_3\text{C}_2\text{Cl}_2$ MXene via ZnCl_2 etching in 2021 and investigated its gas-sensing performance [246]. They found that $\text{Ti}_3\text{C}_2\text{Cl}_2$ MXene exhibits a response value of 13.2% to NH_3 , indicating the potential of $\text{Ti}_3\text{C}_2\text{Cl}_2$ MXene in gas sensors. In addition, Au/Pt/ $\text{Ti}_3\text{C}_2\text{Cl}_2$ hybrids as sensors were fabricated by ZnCl_2 etching and subsequent self-reduction

process (Fig. 17a) [247]. The Ti species with low-valence can effectively reduce Au^{3+} and Pt^{4+} cations to Au and Pt nanoparticles, respectively, which are then distributed on the surface of $\text{Ti}_3\text{C}_2\text{Cl}_2$ nanosheets (Fig. 17b). By virtue of the superior catalytic activity of obtained Au/Pt/ $\text{Ti}_3\text{C}_2\text{Cl}_2$ composites, a colorimetric sensing platform is constructed to in-situ detect the H_2O_2 from HeLa cells. The fabricated sensor possesses a wide detection range of 50–10,000 μM and detection limit of 10.24 μM (Fig. 17c), demonstrating promising application in intracellular biosensing.

4.4 Microwave Absorption

With the rapid development of information technology in recent years, smart devices based on electromagnetic wave have been utilized more and more frequently, thus resulting in increasingly serious electromagnetic pollution [248, 249]. Therefore, exploring advanced microwave absorption materials is becoming increasingly important. MXenes demonstrate great potential in the fields of microwave absorption based on the following aspects: (1) The layered architecture can realize multiple reflection and scattering of electromagnetic wave; (2) The high electronic conductivity endows MXenes with high dielectric loss; (3) The surface groups of MXenes will produce dipole under electromagnetic field, which further strengthens the dielectric loss [52]. It is noteworthy that MXenes/metal hybrids obtained by one-step Lewis acidic etching can exhibit good microwave absorption performance due to the addition of ferromagnetic metals. For example, Wang et al. firstly prepared $\text{Ti}_3\text{CNCl}_2(\text{Co})$ hybrids via CoCl_2 etching, and $\text{Ti}_3\text{CNCl}_2(\text{Co})$ composites were then distributed on the surface of reduced graphene oxide (RGO) nanosheets to form Ti_3CNCl_2 -decorated RGO aerogel via the crosslinking effect of dopamine hydrochloride (Fig. 17d) [250]. Benefiting from the conductivity loss of 3D interconnecting conductive network, improved polarization loss of abundant heterogeneous interfaces and surface functional groups as well as magnetic loss of Co nanoparticles, the $\text{Ti}_3\text{CNCl}_2/\text{RGO}$ aerogel can deliver a minimum reflection loss intensity of -62.62 dB at 17.2 GHz with a thickness of 2.5 mm (Fig. 17e), indicating its boosted microwave absorbing ability.

Table 3 provides an overall summary of the performance of MXenes and MXene-based materials in the fields of LIBs, SIBs, ZIBs, Li–S batteries, metal anodes, DIBs, SCs, PSCs,

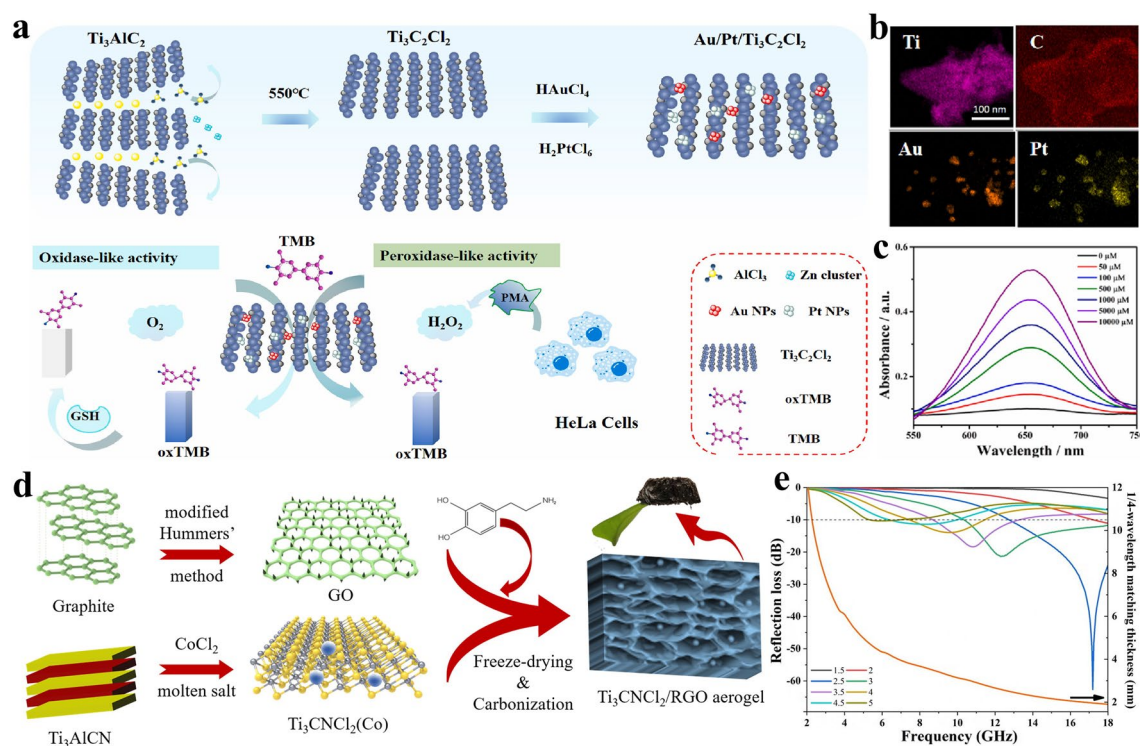


Fig. 17 **a** Schematic demonstrating the synthesis of Au/Pt/Ti₃C₂Cl₂ hybrids for in-situ detection of H₂O₂ and colorimetric detection of glutathione. **b** EDS element mapping of Au/Pt/Ti₃C₂Cl₂ composites. **c** Absorption spectra of Au/Pt/Ti₃C₂Cl₂ nanocomposites system with increasing concentrations of H₂O₂. Reproduced with permission from [247] Copyright 2022, Elsevier. **d** Schematic representing the preparation of Ti₃CNCl₂/RGO aerogel. **e** Reflection loss of Ti₃CNCl₂/RGO. Reproduced with permission from [250] Copyright 2021, Elsevier

HER, overall water splitting, CO₂RR, NRR, sensors and microwave absorption.

5 Summary and Perspectives

In the past eleven years, great progress has been achieved in the development of MXenes, which can be effectively confirmed by the increasing publications. Notably, the compositional and structural diversity of MXenes have been considerably expanded. In terms of composition, M-site atoms, X-site atoms and surface groups all exhibit rich selection space. Structurally, *i*-MXenes, *o*-MXenes and high-entropy MXenes have also been extensively explored. It can be anticipated that if an efficient and general preparation method is applied, plenty of new MXenes with various compositions and structures can be successfully obtained, and they may demonstrate some fascinating properties. Therefore, exploring a safe, green, non-hazardous, low-cost and easily scalable synthesis method has always been the research focus in

the MXene community. Up to now, many preparation strategies for MXenes have been proposed, such as HF etching, in-situ HF etching, bifluoride salts etching, electrochemical etching, alkali etching, common molten salts etching, ionic liquids etching, halogen etching and chemical vapor deposition. Nevertheless, they all have their own shortcomings and are unsuitable for large-scale application (Table 1). For example, HF etching, in-situ HF etching and alkali etching all exhibit high or medium experimental risk. Additionally, bifluoride salts etching, alkali etching, common molten salts etching, ionic liquids etching and halogen etching demonstrate poor universality. More importantly, the MXenes prepared by above-mentioned methods fail to demonstrate controllable and uniform terminations. Lewis acidic etching, as an emerging preparation strategy for MXenes, has attracted increasing attention in the past three years owing to a series of merits, such as significantly boosted safety, superior generality, the ability to endow MXenes with uniform surface groups and the potential for large-scale application.

Table 3 Summary of the performance of MXenes and MXene-based materials prepared by Lewis acidic etching route

Materials	Application	Performance	Refs
Ti ₃ C ₂ T _x	LIBs	205 mAh g ⁻¹ at 0.6C	[67]
e-MS-Ti ₃ C ₂ T _x	LIBs	225 mAh g ⁻¹ at 0.2 A g ⁻¹ , 95 mAh g ⁻¹ at 16 A g ⁻¹	[153]
Ti ₃ C ₂ Br _x	LIBs	189 mAh g ⁻¹ at 0.05 A g ⁻¹	[178]
Ti ₃ C ₂ T _x /Sn	LIBs	226.2 mAh g ⁻¹ after 1,000 cycles at 0.2 A g ⁻¹	[145]
Ti ₂ CT _x	LIBs	280 mAh g ⁻¹ at 0.1 A g ⁻¹ , 160 mAh g ⁻¹ at 2 A g ⁻¹	[112]
Ti ₂ CT _x	LIBs	280 mAh g ⁻¹ at 0.1 A g ⁻¹	[175]
Ti ₂ NT _x	LIBs	350 mAh g ⁻¹ after 1200 cycles at 1 A g ⁻¹	[176]
Nb ₂ CT _x	LIBs	330 mAh g ⁻¹ at 0.05 A g ⁻¹ , 80 mAh g ⁻¹ at 10 A g ⁻¹	[119]
Ti ₃ C ₂ T _x /FeS ₂	SIBs	474.9 mAh g ⁻¹ after 600 cycles at 5 A g ⁻¹	[147]
Ti ₃ C ₂ T _x /CuS	SIBs	347 mAh g ⁻¹ after 800 cycles at 3 A g ⁻¹	[148]
Fe ₂ O ₃ @Ti ₃ C ₂ T _x	SIBs	350 mAh g ⁻¹ after 200 cycles at 1.0 A g ⁻¹	[180]
Ti ₃ C ₂ I ₂	ZIBs	181 mAh g ⁻¹ at 0.25 A g ⁻¹	[123]
Ti ₃ C ₂ I ₂	ZIBs	207 mAh g ⁻¹ at 0.5 A g ⁻¹ , 126 mAh g ⁻¹ at 5 A g ⁻¹	[194]
SA-Zn-MXene	Li-S	80% retention after 200 cycles at 4C	[157]
N-MX-CoS ₂	Li-S	651 mAh g ⁻¹ after 700 cycles at 1C	[146]
Zn-MXene	Li metal	11.3 ± 0.1 mV overpotential, 1,200 h cycle life	[156]
Ti ₃ C ₂ Cl ₂	Zn metal	840 h at 2 mA cm ⁻² with a capacity of 1 mAh cm ⁻²	[212]
Ti ₃ C ₂ Cl ₂	DIBs	141 mAh g ⁻¹ after 1000 cycles at 1 A g ⁻¹	[113]
Ti ₃ C ₂ Cl ₂	SCs	92 C g ⁻¹ at 5 mV s ⁻¹	[218]
Ti ₃ C ₂ Cl ₂ -CTAB	SCs	7% capacitance loss after 3,000 cycles at 1.0 A g ⁻¹	[219]
N-containing Ti ₃ C ₂ T _x	SCs	303 F g ⁻¹ at 2 V s ⁻¹	[126]
Ti ₃ C ₂ -Cu	SCs	103.3 μWh cm ⁻² at 0.8 mW cm ⁻²	[122]
QD-Ti ₃ C ₂ Cl ₂ @NiAl-LDHs	SCs	2010.8 F g ⁻¹ at 1.0 A g ⁻¹	[222]
Ti ₃ C ₂ Cl _x	PSCs	11.08% conversion efficiency, 1.702 V voltage	[159]
Ti ₃ C ₂ Cl _x QDs	PSCs	21.31% conversion efficiency, 1.19 V voltage	[228]
Ti ₃ CNCl ₂ @CoS ₂	HER	Tafel slope of 89 mV dec ⁻¹	[233]
Ti ₃ C ₂ T _x :Co	HER	103.6 mV overpotential at 10 mA cm ⁻²	[232]
Ti ₃ C ₂ Cl ₂	Water splitting	330 mV overpotential at 30 mA cm ⁻² for OER 259 mV overpotential at 10 mA cm ⁻² for HER	[237]
SA-Cu-MXene	CO ₂ RR	59.1% Faradaic efficiency	[158]
HD-Fe-MXene	NRR	21.8% Faradaic efficiency	[244]
Ti ₃ C ₂ Cl ₂	Sensors	13.2% response to NH ₃	[246]
Au/Pt/Ti ₃ C ₂ Cl ₂	Sensors	Wide detection range of 50–10,000 μM	[247]
Ti ₃ CNCl ₂ /RGO	Microwave absorption	-62.62 dB at 17.2 GHz	[250]

In this review, we have systematically introduced the Lewis acidic molten salts etching strategy from four aspects: etching mechanism, terminations regulation, in-situ formed metals and delamination of multi-layered MXenes. Briefly, the etching mechanism is mainly based on the replacement reaction between metal cations in Lewis acidic molten salts and zero-valence A-site atoms in MAX precursor. The difficulty degree of etching reaction mainly depends on the redox potentials of molten cations and A-site atoms, but has nothing to do with the M, X-site atoms and *n* value in

MAX phase. A simple criterion is that the metal cations in Lewis acidic salts with high redox potentials can readily etch the MAX phases with low redox potential A-site atoms. Accordingly, some nitride MAX including Ti₂AlN and Ti₄AlN₃ and non-Al MAX such as Ti₃SiC₂ and Ta₂GaC with high exfoliation energy can be successfully etched by various Lewis acidic molten salts. Additionally, uniform Cl, Br or I-terminated MXenes is able to be obtained by Lewis acidic etching, and they all exhibit metallic-level conductivities and even superconductivity in the low-temperature

region. These redox-active groups-terminated MXenes have been investigated in SCs and advanced batteries. More importantly, halogen groups such as $-Cl$ and $-Br$ can be substituted by S^{2-} , Se^{2-} , Te^{2-} , N^{3-} and NH_2^- anions from Lewis bases molten salts via nucleophilic reaction owing to the low dissociation energies of $Ti-Br$ and $Ti-Cl$ bond, really realizing the controllable terminations. Further, the in-situ generated metal nanoparticles can be tightly anchored among the MXenes substrate during the etching process. The rational and effective application of MXenes/metals and one-step sulfidation treatment-obtained MXenes/metal sulfides composites in LIBs, SIBs, Li-S batteries, SCs and HER have been demonstrated. Subsequently, the multi-layered MXenes obtained by Lewis acidic etching have been delaminated into few-layered nanosheets via *n*-BuLi, IPA, TBAOH, DMSO or *i*-PrA intercalation. Finally, the application of obtained MXenes and MXene-based hybrids via Lewis acidic etching route in LIBs, SIBs, ZIBs, Li-S batteries, metal anodes, DIBs, SCs, PSCs, HER, overall water splitting, CO_2RR , NRR, sensors and microwave absorption have been carefully summarized. Up to now, most applications are concentrated in the fields of energy storage and conversion. However, the development of Lewis acidic etching is still in its infancy, and more efforts are required to fully understand this method and promote its widespread application. Some main challenges and opportunities are listed as follows:

- (1) At present, there are still some details to be researched during the Lewis acidic etching process. For example, the reaction between metal cations in Lewis acidic molten salts and M species in MAX phase during the etching process has been confirmed, which generally results in the formation of single atom-implanted MXenes. However, the specific mechanism and the difficulty degree of above reaction still require further exploration through a lot of experiments and theoretical calculations, which is conducive to the controlled preparation of single atom-implanted MXenes. In addition, a recent study has proved that NaCl can not only provide molten salts environment during the etching process, but also act as pore-forming agent to form $Ti_3C_2Cl_2$ MXene with in-plane porosity. In the future, more attention should be paid to investigate the universality of NaCl as pore-forming agent, which can greatly promote the preparation of other in-plane porous MXenes through Lewis acidic etching. Notably, the in-situ formed metal nanoparticles are usually aggregated during the cooling process and then anchor on the surface of MXenes. It is unclear whether there are some metal clusters in the interlayer of MXenes. Furthermore, preventing the agglomeration of metal nanoparticles is also worth investigating.
- (2) In the future, more researches should be carried out to synthesize nitride MXenes via Lewis acidic etching. It can be expected that more nitride MXenes will be successfully prepared due to the superior universality of Lewis acidic etching. Currently, Lewis acidic molten salts are mainly used to etch MAX phase precursors. The future studies are needed to investigate that whether non-MAX ternary layered compounds such as Mo_2Ga_2C can be etched by Lewis acidic salts. Further, transition metal borides (MAB) such as $MoAlB$ and Cr_2AlB_2 , which is similar to MAX phase, have attracted intensive interests in the past few years. Therefore, the universal preparation of MBene by etching MAB precursors with Lewis acidic molten salts is worthy of in-depth investigation. Finally, the parameters of Lewis acidic etching reaction, including the molar ratio of MAX precursor and Lewis acidic salts, reaction temperature, time and atmosphere, are widely different in reported literatures (Table 2). More efforts are still required to optimize the etching parameters on the premise of ensuring the successful preparation of MXenes, such as selecting low-cost Lewis acidic salts, decreasing the amount of Lewis acidic salts and reaction temperature and changing the reaction atmosphere from protective gas to air, which is beneficial for the large-scale preparation of MXenes via Lewis acidic etching.
- (3) Although MXenes prepared by Lewis acidic etching can be theoretically terminated by uniform halogen groups, some halogen terminations will inevitably be replaced by $-O$ in air atmosphere or during the washing process. In addition, the surface group substitution/elimination reactions in molten inorganic salts are carried out in Ar-filled glovebox in order to avoid the competition between $-O$ functional group and other terminations. In the future, it is an urgent issue to maintain uniform termination for MXenes obtained by Lewis acidic etching under air atmosphere. All in all, combined with Lewis acidic etching, termination exchange reaction in Lewis bases molten salts medium can indeed endow MXenes with unconventional terminations. Therefore, much work should be needed to explore the influence of new terminations (S, Se, Te, N, NH, etc.) on the properties of various MXenes, such as electronic, optical and mechanical, magnetic properties as well as ion migration kinetics, hydrophilicity, chemical and thermal stability, etc.

- (4) So far, MXenes/metals hybrids prepared by Lewis acidic etching have been successfully applied in LIBs and SCs. In the future, MXenes/metals composites exhibit great research potential in catalysis, metal anodes and other fields. For example, benefiting from the unique layered structure and superior charge/mass transfer kinetics of MXenes as well as nucleation induction effect of some metals (Co, Sn, etc.), MXenes/metals hybrids can be utilized as three-dimensional frameworks to suppress the dendrite growth of metal anodes (Li, Na, K, Zn, etc.). Furthermore, the obtained MXenes/metals hybrids can be transformed to MXenes/metal compounds composites via one-step sulfurization, phosphorization, selenization or tellurization treatment. Currently, most of the research was concentrated in MXenes/metal sulfides hybrids, such as N-MX-CoS₂ and Ti₃C₂T_x/FeS₂. In the future, more studies should be performed to prepare MXenes/metal phosphides, MXenes/metal selenides or MXenes/metal tellurides hybrids via Lewis acidic etching route, which can be rationally and effectively applied in LIBs, SIBs, potassium-ion batteries and so on.
- (5) Up to now, most of MXenes prepared by Lewis acidic etching are still at multi-layered state (Table 2). The absence of hydrophilic terminations such as -OH makes it difficult for the obtained multi-layered MXenes to be dispersed in water and then intercalated by large organic molecules, thus reducing the delamination efficiency and exhibiting a low yield of few-layered and single-layered nanosheets. Although some attempts have been made, such as improving the hydrophilicity of MXenes by KOH treatment, or intercalating MXenes by *n*-BuLi in organic solvent NMF, there is still no safe, green, efficient and easily scalable method to delaminate the Lewis acidic molten salts-etched multi-layered MXenes. In the future, great efforts should be made to explore other appropriate delamination methods, such as high-energy ball milling and electrochemical delamination.

In conclusion, although some progress has been made in the development of Lewis acidic etching, it is still in the early stage. In order to solve the above-mentioned challenges, much more work should still be done in the near future. It can be anticipated that Lewis acidic etching will experience a rapid development period, which can attract more and more researchers in MXene community to widely utilize this emerging preparation strategy.

Acknowledgements This work was financially supported by the Highstar Corporation HSD20210118 and Taihu Electric Corporation 0001.

Funding Open access funding provided by Shanghai Jiao Tong University.

Open Access This article is licensed under a Creative Commons Attribution 4.0 International License, which permits use, sharing, adaptation, distribution and reproduction in any medium or format, as long as you give appropriate credit to the original author(s) and the source, provide a link to the Creative Commons licence, and indicate if changes were made. The images or other third party material in this article are included in the article's Creative Commons licence, unless indicated otherwise in a credit line to the material. If material is not included in the article's Creative Commons licence and your intended use is not permitted by statutory regulation or exceeds the permitted use, you will need to obtain permission directly from the copyright holder. To view a copy of this licence, visit <http://creativecommons.org/licenses/by/4.0/>.

References

1. K.S. Novoselov, A.K. Geim, S.V. Morozov, D. Jiang, Y. Zhang et al., Electric field effect in atomically thin carbon films. *Science* **306**(5696), 666–669 (2004). <https://doi.org/10.1126/science.1102896>
2. C. Tan, X. Cao, X.J. Wu, Q. He, J. Yang et al., Recent advances in ultrathin two-dimensional nanomaterials. *Chem. Rev.* **117**(9), 6225–6331 (2017). <https://doi.org/10.1021/acs.chemrev.6b00558>
3. M. Chhowalla, H.S. Shin, G. Eda, L.J. Li, K.P. Loh et al., The chemistry of two-dimensional layered transition metal dichalcogenide nanosheets. *Nat. Chem.* **5**(4), 263–275 (2013). <https://doi.org/10.1038/nchem.1589>
4. Q. Weng, X. Wang, X. Wang, Y. Bando, D. Golberg, Functionalized hexagonal boron nitride nanomaterials: emerging properties and applications. *Chem. Soc. Rev.* **45**(14), 3989–4012 (2016). <https://doi.org/10.1039/C5CS00869G>
5. S. Cao, J. Low, J. Yu, M. Jaroniec, Polymeric photocatalysts based on graphitic carbon nitride. *Adv. Mater.* **27**(13), 2150–2176 (2015). <https://doi.org/10.1002/adma.201500033>
6. T. Hartman, Z. Sofer, Beyond graphene: chemistry of group 14 graphene analogues: silicene, germanene, and stanene. *ACS Nano* **13**(8), 8566–8576 (2019). <https://doi.org/10.1021/acsnano.9b04466>
7. H. Liu, K. Hu, D. Yan, R. Chen, Y. Zou et al., Recent advances on black phosphorus for energy storage, catalysis, and sensor applications. *Adv. Mater.* **30**(32), 1800295 (2018). <https://doi.org/10.1002/adma.201800295>
8. V. Nicolosi, M. Chhowalla, M.G. Kanatzidis, M.S. Strano, J.N. Coleman, Liquid exfoliation of layered materials. *Science* **340**(6139), 1226419 (2013). <https://doi.org/10.1126/science.1226419>



9. L. Lv, Z. Yang, K. Chen, C. Wang, Y. Xiong, 2D layered double hydroxides for oxygen evolution reaction: from fundamental design to application. *Adv. Energy Mater.* **9**(17), 1803358 (2019). <https://doi.org/10.1002/aenm.201803358>
10. A. Zavabeti, A. Jannat, L. Zhong, A.A. Haidry, Z. Yao et al., Two-dimensional materials in large-areas: synthesis, properties and applications. *Nano-Micro Lett.* **12**(1), 66 (2020). <https://doi.org/10.1007/s40820-020-0402-x>
11. M. Naguib, M. Kurtoglu, V. Presser, J. Lu, J. Niu et al., Two-dimensional nanocrystals produced by exfoliation of Ti_3AlC_2 . *Adv. Mater.* **23**(37), 4248–4253 (2011). <https://doi.org/10.1002/adma.201102306>
12. M. Naguib, V.N. Mochalin, M.W. Barsoum, Y. Gogotsi, 25th anniversary article: MXenes: a new family of two-dimensional materials. *Adv. Mater.* **26**(7), 992–1005 (2014). <https://doi.org/10.1002/adma.201304138>
13. M. Naguib, O. Mashtalir, J. Carle, V. Presser, J. Lu et al., Two-dimensional transition metal carbides. *ACS Nano* **6**(2), 1322–1331 (2012). <https://doi.org/10.1021/nn204153h>
14. Y. Gogotsi, Q. Huang, MXenes: two-dimensional building blocks for future materials and devices. *ACS Nano* **15**(4), 5775–5780 (2021). <https://doi.org/10.1021/acsnano.1c03161>
15. X. Li, Z. Huang, C.E. Shuck, G. Liang, Y. Gogotsi, C. Zhi, MXene chemistry, electrochemistry and energy storage applications. *Nat. Rev. Chem.* **6**(6), 389–404 (2022). <https://doi.org/10.1038/s41570-022-00384-8>
16. Y. An, Y. Tian, J. Feng, Y. Qian, MXenes for advanced separator in rechargeable batteries. *Mater. Today* **57**, 146–179 (2022). <https://doi.org/10.1016/j.mattod.2022.06.006>
17. M. Sokol, V. Nату, S. Kota, M.W. Barsoum, On the chemical diversity of the MAX phases. *Trends Chem.* **1**(2), 210–223 (2019). <https://doi.org/10.1016/j.trechm.2019.02.016>
18. J. Halim, S. Kota, M.R. Lukatskaya, M. Naguib, M.-Q. Zhao et al., Synthesis and characterization of 2D molybdenum Carbide (MXene). *Adv. Funct. Mater.* **26**(18), 3118–3127 (2016). <https://doi.org/10.1002/adfm.201505328>
19. J. Zhou, X. Zha, F.Y. Chen, Q. Ye, P. Eklund et al., A two-dimensional zirconium carbide by selective etching of Al_2C_3 from nanolaminated $\text{Zr}_3\text{Al}_3\text{C}_5$. *Angew. Chem. Int. Ed.* **55**(16), 5008–5013 (2016). <https://doi.org/10.1002/anie.201510432>
20. J. Zhou, X. Zha, X. Zhou, F. Chen, G. Gao et al., Synthesis and electrochemical properties of two-dimensional hafnium carbide. *ACS Nano* **11**(4), 3841–3850 (2017). <https://doi.org/10.1021/acsnano.7b00030>
21. M. Shekhirev, C.E. Shuck, A. Sarycheva, Y. Gogotsi, Characterization of MXenes at every step, from their precursors to single flakes and assembled films. *Prog. Mater. Sci.* **120**, 100757 (2021). <https://doi.org/10.1016/j.pmatsci.2020.100757>
22. N.R. Hemanth, B. Kandasubramanian, Recent advances in 2D MXenes for enhanced cation intercalation in energy harvesting applications: a review. *Chem. Eng. J.* **392**, 123678 (2020). <https://doi.org/10.1016/j.cej.2019.123678>
23. D. Xiong, X. Li, Z. Bai, S. Lu, Recent advances in layered $\text{Ti}_3\text{C}_2\text{T}_x$ MXene for electrochemical energy storage. *Small* **14**(17), 1703419 (2018). <https://doi.org/10.1002/sml.201703419>
24. B. Anasori, M.R. Lukatskaya, Y. Gogotsi, 2D metal carbides and nitrides (MXenes) for energy storage. *Nat. Rev. Mater.* **2**(2), 16098 (2017). <https://doi.org/10.1038/natrevmats.2016.98>
25. S. Zhang, W.Q. Han, Recent advances in MXenes and their composites in lithium/sodium batteries from the viewpoints of components and interlayer engineering. *Phys. Chem. Chem. Phys.* **22**(29), 16482–16526 (2020). <https://doi.org/10.1039/D0CP02275F>
26. B.C. Wyatt, A. Rosenkranz, B. Anasori, 2D MXenes: tunable mechanical and tribological properties. *Adv. Mater.* **33**(17), 2007973 (2021). <https://doi.org/10.1002/adma.202007973>
27. B. Anasori, Y. Gogotsi, MXenes: trends, growth, and future directions. *Graphene 2D Mater.* **7**(3–4), 75–79 (2022). <https://doi.org/10.1007/s41127-022-00053-z>
28. M.K. Aslam, Y. Niu, M. Xu, MXenes for non-lithium-ion (Na, K, Ca, Mg, and Al) batteries and supercapacitors. *Adv. Energy Mater.* **11**(2), 2000681 (2020). <https://doi.org/10.1002/aenm.202000681>
29. A. Shayesteh Zeraati, S.A. Mirkhani, P. Sun, M. Naguib, P.V. Braun et al., Improved synthesis of $\text{Ti}_3\text{C}_2\text{T}_x$ MXenes resulting in exceptional electrical conductivity, high synthesis yield, and enhanced capacitance. *Nanoscale* **13**(6), 3572–3580 (2021). <https://doi.org/10.1039/D0NR06671K>
30. J. Luo, W. Zhang, H. Yuan, C. Jin, L. Zhang et al., Pillared Structure design of mxene with ultralarge interlayer spacing for high-performance lithium-ion capacitors. *ACS Nano* **11**(3), 2459–2469 (2017). <https://doi.org/10.1021/acsnano.6b07668>
31. M. Naguib, M.W. Barsoum, Y. Gogotsi, Ten years of progress in the synthesis and development of MXenes. *Adv. Mater.* **33**(39), 2103393 (2021). <https://doi.org/10.1002/adma.202103393>
32. M. Han, C.E. Shuck, R. Rakhmanov, D. Parchment, B. Anasori et al., Beyond $\text{Ti}_3\text{C}_2\text{T}_x$: MXenes for electromagnetic interference shielding. *ACS Nano* **14**(4), 5008–5016 (2020). <https://doi.org/10.1021/acsnano.0c01312>
33. G. Deysher, C.E. Shuck, K. Hantanasirisakul, N.C. Frey, A.C. Foucher et al., Synthesis of Mo_4VAIC_4 MAX phase and two-dimensional Mo_4VC_4 MXene with five atomic layers of transition metals. *ACS Nano* **14**(1), 204–217 (2020). <https://doi.org/10.1021/acsnano.9b07708>
34. Y. Gogotsi, B. Anasori, The rise of MXenes. *ACS Nano* **13**(8), 8491–8494 (2019). <https://doi.org/10.1021/acsnano.9b06394>
35. M. Dadashi Firouzjaei, M. Karimiziarani, H. Moradkhani, M. Elliott, B. Anasori, MXenes: the two-dimensional influencers. *Mater. Today Adv.* **13**, 100202 (2022). <https://doi.org/10.1016/j.mtadv.2021.100202>
36. B. Ahmed, A.E. Ghazaly, J. Rosen, i-MXenes for energy storage and catalysis. *Adv. Funct. Mater.* **30**(47), 2000894 (2020). <https://doi.org/10.1002/adfm.202000894>

37. K. Fan, Y. Ying, X. Luo, H. Huang, Nitride MXenes as sulfur hosts for thermodynamic and kinetic suppression of polysulfide shuttling: a computational study. *J. Mater. Chem. A* **9**(45), 25391–25398 (2021). <https://doi.org/10.1039/D1TA06759A>
38. D. Johnson, Z. Qiao, E. Uwadiunor, A. Djire, Holdups in nitride MXene's development and limitations in advancing the field of MXene. *Small* **18**(17), 2106129 (2022). <https://doi.org/10.1002/sml.202106129>
39. J. Nan, X. Guo, J. Xiao, X. Li, W. Chen et al., Nanoengineering of 2D MXene-based materials for energy storage applications. *Small* **17**(9), 1902085 (2021). <https://doi.org/10.1002/sml.201902085>
40. T. Su, X. Ma, J. Tong, H. Ji, Z. Qin et al., Surface engineering of MXenes for energy and environmental applications. *J. Mater. Chem. A* **10**(19), 10265–10296 (2022). <https://doi.org/10.1039/D2TA01140A>
41. J. Björk, J. Rosen, Functionalizing MXenes by tailoring surface terminations in different chemical environments. *Chem. Mater.* **33**(23), 9108–9118 (2021). <https://doi.org/10.1021/acs.chemmater.1c01264>
42. A.S.F. Vladislav Kamysbayev, H. Hu, X. Rui, F. Lagunas, D. Wang et al., Covalent surface modifications and superconductivity of two-dimensional metal carbide MXenes. *Science* **369**(6506), 979–983 (2020). <https://doi.org/10.1126/science.aba8311>
43. Y. Wei, P. Zhang, R.A. Soomro, Q. Zhu, B. Xu, Advances in the synthesis of 2D MXenes. *Adv. Mater.* **33**(39), 2103148 (2021). <https://doi.org/10.1002/adma.202103148>
44. M.S. Bhargava Reddy, S. Kailasa, B.C.G. Marupalli, K.K. Sadasivuni, S. Aich, A family of 2D-MXenes: synthesis, properties, and gas sensing applications. *ACS Sens.* **7**(8), 2132–2163 (2022). <https://doi.org/10.1021/acssensors.2c01046>
45. A.R. VahidMohammadi, J. Rosen, Y. Gogotsi, The world of two-dimensional carbides and nitrides (MXenes). *Science* **372**(6547), eabf1581 (2021). <https://doi.org/10.1126/science.abf1581>
46. C. Zhang, Y. Ma, X. Zhang, S. Abdolhosseinzadeh, H. Sheng et al., Two-dimensional transition metal carbides and nitrides (MXenes): synthesis, properties, and electrochemical energy storage applications. *Energy Environ. Mater.* **3**(1), 29–55 (2020). <https://doi.org/10.1002/eem2.12058>
47. D. Er, J. Li, M. Naguib, Y. Gogotsi, V.B. Shenoy, Ti_3C_2 MXene as a high capacity electrode material for metal (Li, Na, K, Ca) ion batteries. *ACS Appl. Mater. Interfaces* **6**(14), 11173–11179 (2014). <https://doi.org/10.1021/am501144q>
48. B.-M. Jun, S. Kim, J. Heo, C.M. Park, N. Her et al., Review of MXenes as new nanomaterials for energy storage/delivery and selected environmental applications. *Nano Res.* **12**(3), 471–487 (2018). <https://doi.org/10.1007/s12274-018-2225-3>
49. X. Zhang, Z. Zhang, Z. Zhou, MXene-based materials for electrochemical energy storage. *J. Energy Chem.* **27**(1), 73–85 (2018). <https://doi.org/10.1016/j.jechem.2017.08.004>
50. X. Guo, C. Wang, W. Wang, Q. Zhou, W. Xu et al., Vacancy manipulating of molybdenum carbide mxenes to enhance faraday reaction for high performance lithium-ion batteries. *Nano Res. Energy* **1**, e9120026 (2022). <https://doi.org/10.26599/NRE.2022.9120026>
51. H.E. Karahan, K. Goh, C.J. Zhang, E. Yang, C. Yildirim et al., MXene materials for designing advanced separation membranes. *Adv. Mater.* **32**(29), 1906697 (2020). <https://doi.org/10.1002/adma.201906697>
52. A. Iqbal, P. Sambyal, C.M. Koo, 2D MXenes for electromagnetic shielding: a review. *Adv. Funct. Mater.* **30**(47), 2000883 (2020). <https://doi.org/10.1002/adfm.202000883>
53. C. Tsounis, P.V. Kumar, H. Masood, R.P. Kulkarni, G.S. Gautam et al., Advancing MXene electrocatalysts for energy conversion reactions: surface, stoichiometry, and stability. *Angew. Chem. Int. Ed.* **62**(4), e202210828 (2022). <https://doi.org/10.1002/anie.202210828>
54. X. Li, W. You, C. Xu, L. Wang, L. Yang et al., 3D seed-germination-like MXene with in situ growing CNTs/Ni heterojunction for enhanced microwave absorption via polarization and magnetization. *Nano-Micro Lett.* **13**(1), 157 (2021). <https://doi.org/10.1007/s40820-021-00680-w>
55. S. Abdolhosseinzadeh, X. Jiang, H. Zhang, J. Qiu, C. Zhang, Perspectives on solution processing of two-dimensional MXenes. *Mater. Today* **48**, 214–240 (2021). <https://doi.org/10.1016/j.mattod.2021.02.010>
56. C.J. Zhang, L. McKeon, M.P. Kremer, S.H. Park, O. Ronan et al., Additive-free MXene inks and direct printing of micro-supercapacitors. *Nat. Commun.* **10**(1), 1795 (2019). <https://doi.org/10.1038/s41467-019-09398-1>
57. S. Venkateshalu, M. Shariq, N.K. Chaudhari, K. Lee, A.N. Grace, 2D non-carbide MXenes: an emerging material class for energy storage and conversion. *J. Mater. Chem. A* **10**(38), 20174–20189 (2022). <https://doi.org/10.1039/D2TA05392F>
58. Z. Du, C. Wu, Y. Chen, Z. Cao, R. Hu et al., High-entropy atomic layers of transition-metal carbides (MXenes). *Adv. Mater.* **33**(39), 2101473 (2021). <https://doi.org/10.1002/adma.202101473>
59. Q. Tang, Z. Zhou, P. Shen, Are MXenes Promising Anode Materials for Li ion batteries? computational studies on electronic properties and Li storage capability of Ti_3C_2 and $\text{Ti}_3\text{C}_2\text{X}_2$ ($\text{X} = \text{F}, \text{OH}$) monolayer. *J. Am. Chem. Soc.* **134**(40), 16909–16916 (2012). <https://doi.org/10.1021/ja308463r>
60. Y. Xie, P.R.C. Kent, Hybrid density functional study of structural and electronic properties of functionalized $\text{Ti}_{n+1}\text{X}_n$ ($\text{X} = \text{C}, \text{N}$) monolayers. *Phys. Rev. B.* **87**(23), 235441 (2013). <https://doi.org/10.1103/PhysRevB.87.235441>
61. H. Kim, Z. Wang, H.N. Alshareef, MXetronics: electronic and photonic applications of MXenes. *Nano Energy* **60**, 179–197 (2019). <https://doi.org/10.1016/j.nanoen.2019.03.020>
62. K. Wang, H. Jin, H. Li, Z. Mao, L. Tang et al., Role of surface functional groups to superconductivity in Nb_2C -MXene: experiments and density functional theory calculations. *Surf. Interfaces* **29**, 101711 (2022). <https://doi.org/10.1016/j.surfin.2021.101711>
63. R.M. Ronchi, J.T. Arantes, S.F. Santos, Synthesis, structure, properties and applications of MXenes: current status



- and perspectives. *Ceram. Int.* **45**(15), 18167–18188 (2019). <https://doi.org/10.1016/j.ceramint.2019.06.114>
64. C.E. Shuck, Y. Gogotsi, Taking MXenes from the lab to commercial products. *Chem. Eng. J.* **401**, 125786 (2020). <https://doi.org/10.1016/j.cej.2020.125786>
65. M. Ghidui, M.R. Lukatskaya, M.Q. Zhao, Y. Gogotsi, M.W. Barsoum, Conductive two-dimensional titanium carbide “Clay” with high volumetric capacitance. *Nature* **516**(7529), 78–81 (2014). <https://doi.org/10.1038/nature13970>
66. M. Li, J. Lu, K. Luo, Y. Li, K. Chang et al., Element replacement approach by reaction with lewis acidic molten salts to synthesize nanolaminated MAX phases and MXenes. *J. Am. Chem. Soc.* **141**(11), 4730–4737 (2019). <https://doi.org/10.1021/jacs.9b00574>
67. Y. Li, H. Shao, Z. Lin, J. Lu, L. Liu et al., A general lewis acidic etching route for preparing MXenes with enhanced electrochemical performance in non-aqueous electrolyte. *Nat. Mater.* **19**(8), 894–899 (2020). <https://doi.org/10.1038/s41563-020-0657-0>
68. V. Singh, D. Joung, L. Zhai, S. Das, S.I. Khondaker et al., Graphene based materials: past, present and future. *Prog. Mater. Sci.* **56**(8), 1178–1271 (2011). <https://doi.org/10.1016/j.pmatsci.2011.03.003>
69. A.K. Geim, K.S. Novoselov, The rise of graphene. *Nat. Mater.* **6**(3), 183–191 (2007). <https://doi.org/10.1038/nmat1849>
70. M. Anayee, C.E. Shuck, M. Shekhirev, A. Goad, R. Wang et al., Kinetics of Ti_3AlC_2 etching for $Ti_3C_2T_x$ MXene synthesis. *Chem. Mater.* **34**(21), 9589–9600 (2022). <https://doi.org/10.1021/acs.chemmater.2c02194>
71. K.R.G. Lim, M. Shekhirev, B.C. Wyatt, B. Anasori, Y. Gogotsi et al., Fundamentals of MXene synthesis. *Nat. Synth.* **1**(8), 601–614 (2022). <https://doi.org/10.1038/s44160-022-00104-6>
72. P. Huang, S. Zhang, H. Ying, W. Yang, J. Wang et al., Fabrication of Fe nanocomplex pillared few-layered $Ti_3C_2T_x$ MXene with enhanced rate performance for lithium-ion batteries. *Nano Res.* **14**(4), 1218–1227 (2021). <https://doi.org/10.1007/s12274-020-3221-y>
73. P. Huang, S. Zhang, H. Ying, Z. Zhang, W. Han, Few-layered Ti_3C_2 MXene anchoring bimetallic selenide $NiCo_2Se_4$ nanoparticles for superior sodium-ion batteries. *Chem. Eng. J.* **417**, 129161 (2021). <https://doi.org/10.1016/j.cej.2021.129161>
74. C. Huang, S. Shi, H. Yu, Work function adjustment of Nb_2CT_x nanoflakes as hole and electron transport layers in organic solar cells by controlling surface functional groups. *ACS Energy Lett.* **6**(10), 3464–3472 (2021). <https://doi.org/10.1021/acsenergylett.1c01656>
75. D. Sha, C. Lu, W. He, J. Ding, H. Zhang et al., Surface selection strategy for V_2CT_x MXene toward superior Zn-ion storage. *ACS Nano* **16**(2), 2711–2720 (2022). <https://doi.org/10.1021/acsnano.1c09639>
76. S. Zhao, X. Meng, K. Zhu, F. Du, G. Chen et al., Li-Ion uptake and increase in interlayer spacing of Nb_4C_3 MXene. *Energy Storage Mater.* **8**, 42–48 (2017). <https://doi.org/10.1016/j.ensm.2017.03.012>
77. G. Liang, X. Li, Y. Wang, S. Yang, Z. Huang et al., Building durable aqueous K-ion capacitors based on MXene family. *Nano Res. Energy* **1**, e9120002 (2022). <https://doi.org/10.26599/NRE.2022.9120002>
78. O. Mashtalir, M. Naguib, V.N. Mochalin, Y. Dall’Agnese, M. Heon et al., Intercalation and delamination of layered carbides and carbonitrides. *Nat. Commun.* **4**(1), 1716 (2013). <https://doi.org/10.1038/ncomms2664>
79. M. Naguib, R.R. Unocic, B.L. Armstrong, J. Nanda, Large-scale delamination of multi-layers transition metal carbides and carbonitrides “MXenes.” *Dalton Trans.* **44**(20), 9353–9358 (2015). <https://doi.org/10.1039/C5DT01247C>
80. O. Mashtalir, M.R. Lukatskaya, M.Q. Zhao, M.W. Barsoum, Y. Gogotsi, Amine-assisted delamination of Nb_2C MXene for Li-ion energy storage devices. *Adv. Mater.* **27**(23), 3501–3506 (2015). <https://doi.org/10.1002/adma.201500604>
81. M. Alhabeab, K. Maleski, B. Anasori, P. Lelyukh, L. Clark et al., Guidelines for synthesis and processing of two-dimensional titanium carbide ($Ti_3C_2T_x$ MXene). *Chem. Mater.* **29**(18), 7633–7644 (2017). <https://doi.org/10.1021/acs.chemmater.7b02847>
82. T.S. Mathis, K. Maleski, A. Goad, A. Sarycheva, M. Anayee et al., Modified MAX phase synthesis for environmentally stable and highly conductive Ti_3C_2 MXene. *ACS Nano* **15**(4), 6420–6429 (2021). <https://doi.org/10.1021/acsnano.0c08357>
83. M. Naguib, J. Halim, J. Lu, K.M. Cook, L. Hultman et al., New two-dimensional niobium and vanadium carbides as promising materials for Li-ion batteries. *J. Am. Chem. Soc.* **135**(43), 15966–15969 (2013). <https://doi.org/10.1021/ja405735d>
84. B. Anasori, Y. Xie, M. Beidaghi, J. Lu, B.C. Hosler et al., Two-dimensional, ordered, double transition metals carbides (MXenes). *ACS Nano* **9**(10), 9507–9516 (2015). <https://doi.org/10.1021/acsnano.5b03591>
85. M. Alhabeab, K. Maleski, T.S. Mathis, A. Sarycheva, C.B. Hatter et al., Selective etching of silicon from Ti_3SiC_2 (MAX) To obtain 2D titanium carbide (MXene). *Angew. Chem. Int. Ed.* **57**(19), 5444–5448 (2018). <https://doi.org/10.1002/anie.201802232>
86. X. Sang, Y. Xie, M.W. Lin, M. Alhabeab, K.L. Van Aken et al., Atomic defects in monolayer titanium carbide ($Ti_3C_2T_x$) MXene. *ACS Nano* **10**(10), 9193–9200 (2016). <https://doi.org/10.1021/acsnano.6b05240>
87. A. Lipatov, M. Alhabeab, M.R. Lukatskaya, A. Boson, Y. Gogotsi et al., Effect of synthesis on quality, electronic properties and environmental stability of individual monolayer Ti_3C_2 MXene flakes. *Adv. Electron. Mater.* **2**(12), 1600255 (2016). <https://doi.org/10.1002/aelm.201600255>
88. F. Liu, J. Zhou, S. Wang, B. Wang, C. Shen et al., Preparation of high-purity V_2C MXene and electrochemical properties as Li-ion batteries. *J. Electrochem. Soc.* **164**(4), A709–A713 (2017). <https://doi.org/10.1149/2.0641704jes>
89. B. Soundiraraju, B.K. George, Two-dimensional titanium nitride (Ti_2N) MXene: synthesis, characterization, and potential application as surface-enhanced raman scattering substrate. *ACS Nano* **11**(9), 8892–8900 (2017). <https://doi.org/10.1021/acsnano.7b03129>

90. X. Wang, C. Garnerio, G. Rochard, D. Magne, S. Morisset et al., A New etching environment (FeF3/HCl) for the synthesis of two-dimensional titanium carbide MXenes: a route towards selective reactivity vs. water. *J. Mater. Chem. A* **5**(41), 22012–22023 (2017). <https://doi.org/10.1039/C7TA01082F>
91. M. Guo, W.-C. Geng, C. Liu, J. Gu, Z. Zhang et al., Ultrahigh areal capacitance of flexible MXene electrodes: electrostatic and steric effects of terminations. *Chem. Mater.* **32**(19), 8257–8265 (2020). <https://doi.org/10.1021/acs.chemmater.0c02026>
92. J. Halim, M.R. Lukatskaya, K.M. Cook, J. Lu, C.R. Smith et al., Transparent conductive two-dimensional titanium carbide epitaxial thin films. *Chem. Mater.* **26**(7), 2374–2381 (2014). <https://doi.org/10.1021/cm500641a>
93. A. Feng, Y. Yu, Y. Wang, F. Jiang, Y. Yu et al., Two-dimensional MXene Ti_3C_2 produced by exfoliation of Ti_3AlC_2 . *Mater. Des.* **114**, 161–166 (2017). <https://doi.org/10.1016/j.matdes.2016.10.053>
94. V. Natu, R. Pai, M. Sokol, M. Carey, V. Kalra et al., 2D $Ti_3C_2T_x$ MXene synthesized by water-free etching of Ti_3AlC_2 in polar organic solvents. *Chem* **6**(3), 616–630 (2020). <https://doi.org/10.1016/j.chempr.2020.01.019>
95. M.R. Lukatskaya, J. Halim, B. Dyatkin, M. Naguib, Y.S. Buranova et al., Room-temperature carbide-derived carbon synthesis by electrochemical etching of MAX phases. *Angew. Chem. Int. Ed.* **53**(19), 4877–4880 (2014). <https://doi.org/10.1002/anie.201402513>
96. M.-Q. Zhao, M. Sedran, Z. Ling, M.R. Lukatskaya, O. Mashtalir et al., Synthesis of carbon/sulfur nanolaminates by electrochemical extraction of titanium from Ti_2SC . *Angew. Chem. Int. Ed.* **54**(16), 4810–4814 (2015). <https://doi.org/10.1002/anie.201500110>
97. W. Sun, S.A. Shah, Y. Chen, Z. Tan, H. Gao et al., Electrochemical etching of Ti_2AlC to Ti_2CT_x (MXene) in low-concentration hydrochloric acid solution. *J. Mater. Chem. A* **5**(41), 21663–21668 (2017). <https://doi.org/10.1039/C7TA05574A>
98. S. Yang, P. Zhang, F. Wang, A.G. Ricciardulli, M.R. Lohe et al., Fluoride-free synthesis of two-dimensional titanium carbide (MXene) using a binary aqueous system. *Angew. Chem. Int. Ed.* **57**(47), 15491–15495 (2018). <https://doi.org/10.1002/anie.201809662>
99. S.Y. Pang, Y.T. Wong, S. Yuan, Y. Liu, M.K. Tsang et al., Universal strategy for HF-free facile and rapid synthesis of two-dimensional MXenes as multifunctional energy materials. *J. Am. Chem. Soc.* **141**(24), 9610–9616 (2019). <https://doi.org/10.1021/jacs.9b02578>
100. X. Xie, Y. Xue, L. Li, S. Chen, Y. Nie et al., Surface Al leached Ti_3AlC_2 as a substitute for carbon for use as a catalyst support in a harsh corrosive electrochemical system. *Nanoscale* **6**(19), 11035–11040 (2014). <https://doi.org/10.1039/C4NR02080D>
101. T. Li, L. Yao, Q. Liu, J. Gu, R. Luo et al., Fluorine-free synthesis of high-purity $Ti_3C_2T_x$ (T=OH, O) via alkali treatment. *Angew. Chem. Int. Ed.* **57**(21), 6115–6119 (2018). <https://doi.org/10.1002/anie.201800887>
102. S. Zhang, H. Ying, P. Huang, T. Yang, W.-Q. Han, Hierarchical utilization of raw $Ti_3C_2T_x$ MXene for fast preparation of various $Ti_3C_2T_x$ MXene derivatives. *Nano Res.* **15**(3), 2746–2755 (2021). <https://doi.org/10.1007/s12274-021-3847-4>
103. P. Urbankowski, B. Anasori, T. Makaryan, D. Er, S. Kota et al., Synthesis of two-dimensional titanium nitride Ti_4N_3 (MXene). *Nanoscale* **8**(22), 11385–11391 (2016). <https://doi.org/10.1039/C6NR02253G>
104. H. Zong, R. Qi, K. Yu, Z. Zhu, Ultrathin Ti_2NT_x MXene-wrapped MOF-derived CoP frameworks towards hydrogen evolution and water oxidation. *Electrochim. Acta* **393**, 139068 (2021). <https://doi.org/10.1016/j.electacta.2021.139068>
105. P. Urbankowski, B. Anasori, K. Hantanasirisakul, L. Yang, L. Zhang et al., 2D molybdenum and vanadium nitrides synthesized by ammoniation of 2D transition metal carbides (MXenes). *Nanoscale* **9**(45), 17722–17730 (2017). <https://doi.org/10.1039/C7NR06721F>
106. J. Mei, G.A. Ayoko, C. Hu, J.M. Bell, Z. Sun, Two-dimensional fluorine-free mesoporous Mo_2C MXene via UV-induced selective etching of Mo_2Ga_2C for energy storage. *Sustain. Mater. Technol.* **25**, e00156 (2020). <https://doi.org/10.1016/j.susmat.2020.e00156>
107. J. Mei, G.A. Ayoko, C. Hu, Z. Sun, Thermal reduction of sulfur-containing MAX phase for MXene production. *Chem. Eng. J.* **395**, 125111 (2020). <https://doi.org/10.1016/j.cej.2020.125111>
108. H. Shi, P. Zhang, Z. Liu, S. Park, M.R. Lohe et al., Ambient-stable two-dimensional titanium carbide (MXene) enabled by iodine etching. *Angew. Chem. Int. Ed.* **60**(16), 8689–8693 (2021). <https://doi.org/10.1002/anie.202015627>
109. A. Jawaid, A. Hassan, G. Neher, D. Nepal, R. Pachter et al., Halogen etch of Ti_3AlC_2 MAX phase for MXene fabrication. *ACS Nano* **15**(2), 2771–2777 (2021). <https://doi.org/10.1021/acsnano.0c08630>
110. S. Husmann, O. Budak, H. Shim, K. Liang, M. Aslan et al., Ionic liquid-based synthesis of MXene. *Chem. Commun.* **56**(75), 11082–11085 (2020). <https://doi.org/10.1039/D0CC03189E>
111. C. Xu, L. Wang, Z. Liu, L. Chen, J. Guo et al., Large-area high-quality 2D ultrathin Mo_2C superconducting crystals. *Nat. Mater.* **14**(11), 1135–1141 (2015). <https://doi.org/10.1038/nmat4374>
112. G. Ma, H. Shao, J. Xu, Y. Liu, Q. Huang et al., Li-ion storage properties of two-dimensional titanium-carbide synthesized via fast one-pot method in air atmosphere. *Nat. Commun.* **12**(1), 5085 (2021). <https://doi.org/10.1038/s41467-021-25306-y>
113. M. Zhang, R. Liang, N. Yang, R. Gao, Y. Zheng et al., Eutectic etching toward in-plane porosity manipulation of Cl-terminated MXene for high-performance dual-ion battery anode. *Adv. Energy Mater.* **12**(1), 2102493 (2022). <https://doi.org/10.1002/aenm.202102493>
114. J.L. Hart, K. Hantanasirisakul, A.C. Lang, B. Anasori, D. Pinto et al., Control of MXenes' electronic properties through termination and intercalation. *Nat. Commun.* **10**(1), 522 (2019). <https://doi.org/10.1038/s41467-018-08169-8>



115. J. Jiang, S. Bai, J. Zou, S. Liu, J.-P. Hsu et al., Improving stability of MXenes. *Nano Res.* **15**(7), 6551–6567 (2022). <https://doi.org/10.1007/s12274-022-4312-8>
116. Y. Jiang, Y. Zhang, Q. Huang, L. Hao, S. Du, The compositional dependence of structural stability and resulting properties for $M_{n+1}C_nT_2$ ($M = \text{Sc, Ti, V}$; $T = \text{O, OH, F, Cl, Br}$ and I ; $n = 1, 2$): First-principle investigations. *J. Mater. Res. Technol.* **9**(6), 14979–14989 (2020). <https://doi.org/10.1016/j.jmrt.2020.10.083>
117. P. Huang, H. Ying, S. Zhang, Z. Zhang, W.-Q. Han, Multidimensional synergistic architecture of Ti_3C_2 MXene/ CoS_2 @N-doped carbon for sodium-ion batteries with ultralong cycle lifespan. *Chem. Eng. J.* **429**, 132396 (2022). <https://doi.org/10.1016/j.cej.2021.132396>
118. X. Guo, J. Zhang, J. Song, W. Wu, H. Liu et al., MXene encapsulated titanium oxide nanospheres for ultra-stable and fast sodium storage. *Energy Storage Mater.* **14**, 306–313 (2018). <https://doi.org/10.1016/j.ensm.2018.05.010>
119. H. Dong, P. Xiao, N. Jin, B. Wang, Y. Liu et al., Molten salt derived Nb_2CT_x MXene anode for Li-ion batteries. *ChemElectroChem* **8**(5), 957–962 (2021). <https://doi.org/10.1002/celec.202100142>
120. Y. Xie, M. Naguib, V.N. Mochalin, M.W. Barsoum, Y. Gogotsi et al., Role of surface structure on Li-ion energy storage capacity of two-dimensional transition-metal carbides. *J. Am. Chem. Soc.* **136**(17), 6385–6394 (2014). <https://doi.org/10.1021/ja501520b>
121. Y. Xie, Y. Dall’Agnese, M. Naguib, Y. Gogotsi, M.W. Barsoum et al., Prediction and Characterization of MXene nanosheet anodes for non-lithium-ion batteries. *ACS Nano* **8**(9), 9606–9615 (2014). <https://doi.org/10.1021/nn503921j>
122. Y. Bai, C. Liu, T. Chen, W. Li, S. Zheng et al., MXene-copper/cobalt hybrids via lewis acidic molten salts etching for high performance symmetric supercapacitors. *Angew. Chem. Int. Ed.* **60**(48), 25318–25322 (2021). <https://doi.org/10.1002/anie.202112381>
123. M. Li, X. Li, G. Qin, K. Luo, J. Lu et al., Halogenated Ti_3C_2 MXenes with electrochemically active terminals for high-performance zinc ion batteries. *ACS Nano* **15**(1), 1077–1085 (2021). <https://doi.org/10.1021/acsnano.0c07972>
124. J. Lu, I. Persson, H. Lind, J. Palisaitis, M. Li et al., $\text{Ti}_{n+1}\text{C}_n$ MXenes with fully saturated and thermally stable Cl terminations. *Nanoscale Adv.* **1**(9), 3680–3685 (2019). <https://doi.org/10.1039/C9NA00324J>
125. S.-S. Cui, X. Liu, Y.-B. Shi, M.-Y. Ding, X.-F. Yang, Construction of atomic-level charge transfer channel in $\text{Bi}_{12}\text{O}_{17}\text{Cl}_2$ /MXene heterojunctions for improved visible-light photocatalytic performance. *Rare Met.* **41**(7), 2405–2416 (2022). <https://doi.org/10.1007/s12598-022-02011-3>
126. L. Liu, H. Zschiesche, M. Antonietti, B. Daffos, N.V. Tarakina et al., Tuning the surface chemistry of MXene to improve energy storage: example of nitrification by salt melt. *Adv. Energy Mater.* **13**(2), 2202709 (2022). <https://doi.org/10.1002/aenm.202202709>
127. S. Sardar, A. Jana, Covalent surface alteration of MXenes and its effect on superconductivity. *Matter* **3**(5), 1397–1399 (2020). <https://doi.org/10.1016/j.matt.2020.10.007>
128. T. Zhang, L. Chang, X. Zhang, H. Wan, N. Liu et al., Simultaneously tuning interlayer spacing and termination of MXenes by Lewis-basic halides. *Nat. Commun.* **13**(1), 6731 (2022). <https://doi.org/10.1038/s41467-022-34569-y>
129. J. Wu, M. Ihsan-Ul-Haq, F. Ciucci, B. Huang, J.-K. Kim, Rationally designed nanostructured metal chalcogenides for advanced sodium-ion batteries. *Energy Storage Mater.* **34**, 582–628 (2021). <https://doi.org/10.1016/j.ensm.2020.10.007>
130. Y. Xie, J. Hu, Z. Han, T. Wang, J. Zheng et al., Encapsulating sodium deposition into carbon rhombic dodecahedron guided by sodiophilic sites for dendrite-free Na metal batteries. *Energy Storage Mater.* **30**, 1–8 (2020). <https://doi.org/10.1016/j.ensm.2020.05.008>
131. H. Wang, X. Li, Y. Jiang, M. Li, Q. Xiao et al., A universal single-atom coating strategy based on tannic acid chemistry for multifunctional heterogeneous catalysis. *Angew. Chem. Int. Ed.* **61**(14), e202200465 (2022). <https://doi.org/10.1002/anie.202200465>
132. H.J. Kwon, J.-H. Park, S.J. Suh, Multilayered Cu/NiFe thin films for electromagnetic interference shielding at high frequency. *J. Alloys Compd.* **914**, 165330 (2022). <https://doi.org/10.1016/j.jallcom.2022.165330>
133. J.-D. Musah, A.M. Ilyas, S. Venkatesh, S. Mensah, S. Kwofie et al., Isovalent substitution in metal chalcogenide materials for improving thermoelectric power generation—a critical review. *Nano Res. Energy* **1**, 9120034 (2022). <https://doi.org/10.26599/NRE.2022.9120034>
134. S. Zhang, H. Ying, P. Huang, J. Wang, Z. Zhang et al., Rational design of pillared $\text{SnS}/\text{Ti}_3\text{C}_2\text{T}_x$ MXene for superior lithium-ion storage. *ACS Nano* **14**(12), 17665–17674 (2020). <https://doi.org/10.1021/acsnano.0c08770>
135. X. Liu, F. Xu, Z. Li, Z. Liu, W. Yang et al., Design strategy for MXene and metal chalcogenides/oxides hybrids for supercapacitors, secondary batteries and electro/photocatalysis. *Coord. Chem. Rev.* **464**, 214544 (2022). <https://doi.org/10.1016/j.ccr.2022.214544>
136. H. Saini, N. Srinivasan, V. Sedajova, M. Majumder, D.P. Dubal et al., Emerging MXene@metal-organic framework hybrids: design strategies toward versatile applications. *ACS Nano* **15**(12), 18742–18776 (2021). <https://doi.org/10.1021/acsnano.1c06402>
137. S. Zhou, Y. Zhao, R. Shi, Y. Wang, A. Ashok et al., Vacancy-rich MXene-immobilized Ni single atoms as a high-performance electrocatalyst for the hydrazine oxidation reaction. *Adv. Mater.* **34**(36), 2204388 (2022). <https://doi.org/10.1002/adma.202204388>
138. J. Chen, X. Yuan, F. Lyu, Q. Zhong, H. Hu et al., Integrating MXene nanosheets with cobalt-tipped carbon nanotubes for an efficient oxygen reduction reaction. *J. Mater. Chem. A* **7**(3), 1281–1286 (2019). <https://doi.org/10.1039/C8TA10574J>
139. X. Xu, Y. Zhang, H. Sun, J. Zhou, Z. Liu et al., Orthorhombic cobalt ditelluride with Te vacancy defects anchoring on elastic MXene enables efficient potassium-ion storage. *Adv. Mater.* **33**(31), 2100272 (2021). <https://doi.org/10.1002/adma.202100272>

140. W. Peng, J. Han, Y.R. Lu, M. Luo, T.S. Chan et al., A general strategy for engineering single-metal sites on 3D porous N, P Co-doped $\text{Ti}_3\text{C}_2\text{T}_x$ MXene. *ACS Nano* **16**(3), 4116–4125 (2022). <https://doi.org/10.1021/acsnano.1c09841>
141. Y. Tian, Y. An, S. Xiong, J. Feng, Y. Qian, A general method for constructing robust, flexible and freestanding MXene@metal anodes for high-performance potassium-ion batteries. *J. Mater. Chem. A* **7**(16), 9716–9725 (2019). <https://doi.org/10.1039/C9TA02233C>
142. Q. Li, T. Song, Z. Wang, X. Wang, X. Zhou et al., A general strategy toward metal sulfide nanoparticles confined in a sulfur-doped $\text{Ti}_3\text{C}_2\text{T}_x$ MXene 3D porous aerogel for efficient ambient N_2 electroreduction. *Small* **17**(45), 2103305 (2021). <https://doi.org/10.1002/sml.202103305>
143. J. Li, Z. Li, X. Liu, C. Li, Y. Zheng et al., Interfacial engineering of $\text{Bi}_2\text{S}_3/\text{Ti}_3\text{C}_2\text{T}_x$ MXene based on work function for rapid photo-excited bacteria-killing. *Nat. Commun.* **12**(1), 1224 (2021). <https://doi.org/10.1038/s41467-021-21435-6>
144. L. Han, X. Peng, H.-T. Wang, P. Ou, Y. Mi et al., Chemically coupling SnO_2 quantum dots and MXene for efficient CO_2 electroreduction to formate and Zn- CO_2 battery. *Proc. Natl. Acad. Sci. USA* **119**(42), e2207326119 (2022). <https://doi.org/10.1073/pnas.2207326119>
145. Z. Wu, S. Zhu, X. Bai, M. Liang, X. Zhang et al., One-step in-situ synthesis of Sn-nanoconfined $\text{Ti}_3\text{C}_2\text{T}_x$ MXene composites for Li-ion battery anode. *Electrochim. Acta* **407**, 139916 (2022). <https://doi.org/10.1016/j.electacta.2022.139916>
146. C. Yang, Y. Li, W. Peng, F. Zhang, X. Fan, In situ N-doped CoS_2 anchored on MXene toward an efficient bifunctional catalyst for enhanced lithium-sulfur batteries. *Chem. Eng. J.* **427**, 131792 (2022). <https://doi.org/10.1016/j.cej.2021.131792>
147. P. Huang, H. Ying, S. Zhang, Z. Zhang, W.-Q. Han, Molten salts etching route driven universal construction of MXene/transition metal sulfides heterostructures with interfacial electronic coupling for superior sodium storage. *Adv. Energy Mater.* **12**(39), 2202052 (2022). <https://doi.org/10.1002/aenm.202202052>
148. P. Huang, H. Ying, S. Zhang, Z. Zhang, W.-Q. Han, In situ fabrication of MXene/CuS Hybrids with Interfacial Covalent Bonding via Lewis acidic etching route for efficient sodium storage. *J. Mater. Chem. A* **10**(41), 22135–22144 (2022). <https://doi.org/10.1039/D2TA06695E>
149. A. Sarycheva, Y. Gogotsi, Raman spectroscopy analysis of the structure and surface chemistry of $\text{Ti}_3\text{C}_2\text{T}_x$ MXene. *Chem. Mater.* **32**(8), 3480–3488 (2020). <https://doi.org/10.1021/acs.chemmater.0c00359>
150. M. Shekhirev, Y. Ogawa, C.E. Shuck, M. Anayee, T. Torita et al., Delamination of $\text{Ti}_3\text{C}_2\text{T}_x$ nanosheets with NaCl and KCl for improved environmental stability of MXene films. *ACS Appl. Nano Mater.* **5**(11), 16027–16032 (2022). <https://doi.org/10.1021/acsnano.2c03701>
151. M. Malaki, A. Maleki, R.S. Varma, MXenes and ultrasonication. *J. Mater. Chem. A* **7**(18), 10843–10857 (2019). <https://doi.org/10.1039/C9TA01850F>
152. S. Zhang, P. Huang, J. Wang, Z. Zhuang, Z. Zhang et al., Fast and universal solution-phase flocculation strategy for scalable synthesis of various few-layered MXene powders. *J. Phys. Chem. Lett.* **11**(4), 1247–1254 (2020). <https://doi.org/10.1021/acs.jpcclett.9b03682>
153. L. Liu, M. Orbay, S. Luo, S. Duluard, H. Shao et al., Exfoliation and delamination of $\text{Ti}_3\text{C}_2\text{T}_x$ MXene prepared via molten salt etching route. *ACS Nano* **16**(1), 111–118 (2022). <https://doi.org/10.1021/acsnano.1c08498>
154. K. Arole, J.W. Blivin, S. Saha, D.E. Holta, X. Zhao et al., Water-dispersible $\text{Ti}_3\text{C}_2\text{T}_z$ MXene nanosheets by molten salt etching. *iScience* **24**(12), 103403 (2021). <https://doi.org/10.1016/j.isci.2021.103403>
155. K. Arole, J.W. Blivin, A.M. Bruce, S. Athavale, I.J. Echols et al., Exfoliation, delamination, and oxidation stability of molten salt etched Nb_2CT_z MXene nanosheets. *Chem. Commun.* **58**(73), 10202–10205 (2022). <https://doi.org/10.1039/D2CC02237K>
156. J. Gu, Q. Zhu, Y. Shi, H. Chen, D. Zhang et al., Single zinc atoms immobilized on MXene ($\text{Ti}_3\text{C}_2\text{Cl}_x$) layers toward dendrite-free lithium metal anodes. *ACS Nano* **14**(1), 891–898 (2020). <https://doi.org/10.1021/acsnano.9b08141>
157. D. Zhang, S. Wang, R. Hu, J. Gu, Y. Cui et al., Catalytic conversion of polysulfides on single atom zinc implanted MXene toward high-rate lithium-sulfur batteries. *Adv. Funct. Mater.* **30**(30), 2002471 (2020). <https://doi.org/10.1002/adfm.202002471>
158. Q. Zhao, C. Zhang, R. Hu, Z. Du, J. Gu et al., Selective etching quaternary MAX phase toward single atom copper immobilized MXene ($\text{Ti}_3\text{C}_2\text{Cl}_x$) for efficient CO_2 electroreduction to methanol. *ACS Nano* **15**(3), 4927–4936 (2021). <https://doi.org/10.1021/acsnano.0c09755>
159. Q. Zhou, J. Duan, J. Du, Q. Guo, Q. Zhang et al., Tailored lattice “Tape” to confine tensile interface for 11.08%-efficiency all-inorganic CsPbBr₃ perovskite solar cell with an ultrahigh voltage of 1.702 V. *Adv. Sci.* **8**(19), 2101418 (2021). <https://doi.org/10.1002/advs.202101418>
160. T.M. Gür, Review of electrical energy storage technologies, materials and systems: challenges and prospects for large-scale grid storage. *Energy Environ. Sci.* **11**(10), 2696–2767 (2018). <https://doi.org/10.1039/C8EE01419A>
161. Z. Zhu, T. Jiang, M. Ali, Y. Meng, Y. Jin et al., Rechargeable batteries for grid scale energy storage. *Chem. Rev.* **122**(22), 16610–16751 (2022). <https://doi.org/10.1021/acs.chemrev.2c00289>
162. S. Wang, S. Zhao, X. Guo, G. Wang, 2D material-based heterostructures for rechargeable batteries. *Adv. Energy Mater.* **12**(4), 2100864 (2022). <https://doi.org/10.1002/aenm.202100864>
163. Y. Dong, H. Shi, Z.S. Wu, Recent advances and promise of MXene-based nanostructures for high-performance metal ion batteries. *Adv. Funct. Mater.* **30**(47), 2000706 (2020). <https://doi.org/10.1002/adfm.202000706>
164. M. Fichtner, K. Edström, E. Ayerbe, M. Berecibar, A. Bhowmik et al., Rechargeable batteries of the future—the state of the art from a BATTERY 2030+ perspective. *Adv. Energy Mater.* **12**(17), 2102904 (2022). <https://doi.org/10.1002/aenm.202102904>

165. J.Y. Hwang, S.T. Myung, Y.K. Sun, Sodium-ion batteries: present and future. *Chem. Soc. Rev.* **46**(12), 3529–3614 (2017). <https://doi.org/10.1039/C6CS00776G>
166. M. Li, J. Lu, Z. Chen, K. Amine, 30 Years of lithium-ion batteries. *Adv. Mater.* **30**(33), 1800561 (2018). <https://doi.org/10.1002/adma.201800561>
167. Q. Liu, Y. Hu, X. Yu, Y. Qin, T. Meng et al., The pursuit of commercial silicon-based microparticle anodes for advanced lithium-ion batteries: a review. *Nano Res. Energy* **1**, e9120037 (2022). <https://doi.org/10.26599/NRE.2022.9120037>
168. D. Sun, M. Wang, Z. Li, G. Fan, L.-Z. Fan, A. Zhou, Two-dimensional Ti_3C_2 as anode material for Li-ion batteries. *Electrochem. Commun.* **47**, 80–83 (2014). <https://doi.org/10.1016/j.elecom.2014.07.026>
169. T. Zhang, L. Pan, H. Tang, F. Du, Y. Guo et al., Synthesis of two-dimensional $\text{Ti}_3\text{C}_2\text{T}_x$ MXene using $\text{HCl}+\text{LiF}$ etchant: enhanced exfoliation and delamination. *J. Alloys Compd.* **695**, 818–826 (2017). <https://doi.org/10.1016/j.jallcom.2016.10.127>
170. S. Zhang, H. Ying, B. Yuan, R. Hu, W.-Q. Han, Partial atomic tin nanocomplex pillared few-layered $\text{Ti}_3\text{C}_2\text{T}_x$ MXenes for superior lithium-ion storage. *Nano-Micro Lett.* **12**(1), 78 (2020). <https://doi.org/10.1007/s40820-020-0405-7>
171. M. Naguib, J. Come, B. Dyatkin, V. Presser, P.-L. Taberna et al., MXene: a promising transition metal carbide anode for lithium-ion batteries. *Electrochem. Commun.* **16**(1), 61–64 (2012). <https://doi.org/10.1016/j.elecom.2012.01.002>
172. J. Hu, B. Xu, C. Ouyang, S.A. Yang, Y. Yao, Investigations on V_2C and V_2CX_2 ($\text{X} = \text{F}, \text{OH}$) monolayer as a promising anode material for Li ion batteries from first-principles calculations. *J. Phys. Chem. C* **118**(42), 24274–24281 (2014). <https://doi.org/10.1021/jp507336x>
173. E.M.D. Siriwardane, J. Hu, First-principles investigation of Ti_2CSO and Ti_2CSSe Janus MXene structures for Li and Mg electrodes. *J. Phys. Chem. C* **125**(23), 12469–12477 (2021). <https://doi.org/10.1021/acs.jpcc.1c00082>
174. C. Wang, H. Xie, S. Chen, B. Ge, D. Liu et al., Atomic cobalt covalently engineered interlayers for superior lithium-ion storage. *Adv. Mater.* **30**(32), 1802525 (2018). <https://doi.org/10.1002/adma.201802525>
175. J. Chen, Q. Jin, Y. Li, H. Shao, P. Liu et al., Molten salt-shielded synthesis (MS^3) of MXenes in air. *Energy Environ. Mater.* (2022). <https://doi.org/10.1002/eem2.12328>
176. Y. Cao, S. Wei, Q. Zhou, P. Zhang, C. Wang et al., Ti-Cl bonds decorated Ti_2NT_x MXene towards high-performance lithium-ion batteries. *2D Mater.* **10**(1), 014001 (2023). <https://doi.org/10.1088/2053-1583/ac953b>
177. P. Liu, B. Guan, M. Lu, H. Wang, Z. Lin, Influence of aqueous solutions treatment on the Li^+ storage properties of molten salt derived $\text{Ti}_3\text{C}_2\text{Cl}_x$ MXene. *Electrochem. Commun.* **136**, 107236 (2022). <https://doi.org/10.1016/j.elecom.2022.107236>
178. P. Liu, P. Xiao, M. Lu, H. Wang, N. Jin et al., Lithium storage properties of $\text{Ti}_3\text{C}_2\text{T}_x$ ($\text{T}_x = \text{F}, \text{Cl}, \text{Br}$) MXenes. *Chin. Chem. Lett.* (2022). <https://doi.org/10.1016/j.ccllet.2022.04.024>
179. E. Goikolea, V. Palomares, S. Wang, I.R. Larramendi, X. Guo et al., Na-ion batteries—approaching old and new challenges. *Adv. Energy Mater.* **10**(44), 2002055 (2020). <https://doi.org/10.1002/aenm.202002055>
180. Y. Liu, C. Gao, R. Zhou, F. Hong, G. Tong et al., Heteroatoms preintercalated Cl-terminated $\text{Ti}_3\text{C}_2\text{T}_x$ MXene wrapped with mesoporous Fe_2O_3 nanospheres for improved sodium ion storage. *New J. Chem.* **47**(2), 618–627 (2022). <https://doi.org/10.1039/D2NJ05061G>
181. J. Cao, J. Li, D. Li, Z. Yuan, Y. Zhang et al., Strongly coupled 2D transition metal chalcogenide-mxene-carbonaceous nanoribbon heterostructures with ultrafast ion transport for boosting sodium/potassium ions storage. *Nano-Micro Lett.* **13**(1), 113 (2021). <https://doi.org/10.1007/s40820-021-00623-5>
182. Y.-S. Hu, Y. Li, Unlocking Sustainable Na-ion batteries into industry. *ACS Energy Lett.* **6**(11), 4115–4117 (2021). <https://doi.org/10.1021/acscenergylett.1c02292>
183. D. Su, K. Kretschmer, G. Wang, Improved electrochemical performance of Na-ion batteries in ether-based electrolytes: a case study of ZnS nanospheres. *Adv. Energy Mater.* **6**(2), 1501785 (2016). <https://doi.org/10.1002/aenm.201501785>
184. Y.V. Lim, X.L. Li, H.Y. Yang, Recent tactics and advances in the application of metal sulfides as high-performance anode materials for rechargeable sodium-ion batteries. *Adv. Funct. Mater.* **31**(10), 2006761 (2021). <https://doi.org/10.1002/adfm.202006761>
185. Q. Pan, Z. Tong, Y. Su, S. Qin, Y. Tang, Energy storage mechanism, challenge and design strategies of metal sulfides for rechargeable sodium/potassium-ion batteries. *Adv. Funct. Mater.* **31**(37), 2103912 (2021). <https://doi.org/10.1002/adfm.202103912>
186. Y. Xiao, F. Yue, Z. Wen, Y. Shen, D. Su et al., Elastic buffering layer on CuS enabling high-rate and long-life sodium-ion storage. *Nano-Micro Lett.* **14**(1), 193 (2022). <https://doi.org/10.1007/s40820-022-00924-3>
187. B. Li, X. Zhang, T. Wang, Z. He, B. Lu et al., Interfacial engineering strategy for high-performance Zn metal anodes. *Nano-Micro Lett.* **14**(1), 6 (2021). <https://doi.org/10.1007/s40820-021-00764-7>
188. J. Chen, Y. Ding, D. Yan, J. Huang, S. Peng, Synthesis of MXene and its application for zinc-ion storage. *SusMat* **2**(3), 293–318 (2022). <https://doi.org/10.1002/sus2.57>
189. J. Yang, B. Yin, Y. Sun, H. Pan, W. Sun et al., Zinc anode for mild aqueous zinc-ion batteries: challenges, strategies, and perspectives. *Nano-Micro Lett.* **14**(1), 42 (2022). <https://doi.org/10.1007/s40820-021-00782-5>
190. G. Fang, J. Zhou, A. Pan, S. Liang, Recent advances in aqueous zinc-ion batteries. *ACS Energy Lett.* **3**(10), 2480–2501 (2018). <https://doi.org/10.1021/acscenergylett.8b01426>
191. Z. Wang, J. Huang, Z. Guo, X. Dong, Y. Liu et al., A metal-organic framework host for highly reversible dendrite-free zinc metal anodes. *Joule* **3**(5), 1289–1300 (2019). <https://doi.org/10.1016/j.joule.2019.02.012>
192. F. Yu, L. Pang, X. Wang, E.R. Waclawik, F. Wang et al., Aqueous alkaline-acid hybrid electrolyte for zinc-bromine battery with 3 V voltage window. *Energy Storage Mater.* **19**, 56–61 (2019). <https://doi.org/10.1016/j.ensm.2019.02.024>

193. Y. Tian, S. Chen, Y. He, Q. Chen, L. Zhang et al., A highly reversible dendrite-free Zn anode via spontaneous galvanic replacement reaction for advanced zinc-iodine batteries. *Nano Res. Energy* **1**, e9120025 (2022). <https://doi.org/10.26599/NRE.2022.9120025>
194. X. Li, M. Li, Z. Huang, G. Liang, Z. Chen et al., Activating the I^0/I^+ redox couple in an aqueous I_2 -Zn battery to achieve a high voltage plateau. *Energy Environ. Sci.* **14**(1), 407–413 (2021). <https://doi.org/10.1039/D0EE03086D>
195. S.H. Chung, A. Manthiram, Current status and future prospects of metal-sulfur batteries. *Adv. Mater.* **31**(27), 1901125 (2019). <https://doi.org/10.1002/adma.201901125>
196. H. Wang, Z. Cui, S.-A. He, J. Zhu, W. Luo et al., Construction of ultrathin layered MXene-TiN heterostructure enabling favorable catalytic ability for high-areal-capacity lithium-sulfur batteries. *Nano-Micro Lett.* **14**(1), 189 (2022). <https://doi.org/10.1007/s40820-022-00935-0>
197. S. Huang, R. Guan, S. Wang, M. Xiao, D. Han et al., Polymers for high performance Li-S batteries: material selection and structure design. *Prog. Polym. Sci.* **89**, 19–60 (2019). <https://doi.org/10.1016/j.progpolymsci.2018.09.005>
198. Q. Zhao, Q. Zhu, Y. Liu, B. Xu, Status and prospects of MXene-based lithium-sulfur batteries. *Adv. Funct. Mater.* **31**(21), 2100457 (2021). <https://doi.org/10.1002/adfm.20210457>
199. W. Bao, L. Liu, C. Wang, S. Choi, D. Wang et al., Facile synthesis of crumpled nitrogen-doped MXene nanosheets as a new sulfur host for lithium-sulfur batteries. *Adv. Energy Mater.* **8**(13), 1702485 (2018). <https://doi.org/10.1002/aenm.201702485>
200. C. Zhang, J.J. Biendicho, T. Zhang, R. Du, J. Li et al., Combined high catalytic activity and efficient polar tubular nanostructure in urchin-like metallic $NiCo_2Se_4$ for high-performance lithium-sulfur batteries. *Adv. Funct. Mater.* **29**(34), 1903842 (2019). <https://doi.org/10.1002/adfm.201903842>
201. X. Xiao, H. Wang, W. Bao, P. Urbankowski, L. Yang et al., Two-dimensional arrays of transition metal nitride nanocrystals. *Adv. Mater.* **31**(33), 1902393 (2019). <https://doi.org/10.1002/adma.201902393>
202. J. Wu, T. Ye, Y. Wang, P. Yang, Q. Wang et al., Understanding the catalytic kinetics of polysulfide redox reactions on transition metal compounds in Li-S batteries. *ACS Nano* **16**(10), 15734–15759 (2022). <https://doi.org/10.1021/acsnano.2c08581>
203. Q. Chen, Y. Wei, X. Zhang, Z. Yang, F. Wang et al., Vertically aligned MXene nanosheet arrays for high-rate lithium metal anodes. *Adv. Energy Mater.* **12**(18), 2200072 (2022). <https://doi.org/10.1002/aenm.202200072>
204. C. Wei, Y. Tao, H. Fei, Y. An, Y. Tian et al., Recent advances and perspectives in stable and dendrite-free potassium metal anodes. *Energy Storage Mater.* **30**, 206–227 (2020). <https://doi.org/10.1016/j.ensm.2020.05.018>
205. B. Sun, P. Li, J. Zhang, D. Wang, P. Munroe et al., Dendrite-free sodium-metal anodes for high-energy sodium-metal batteries. *Adv. Mater.* **30**(29), 1801334 (2018). <https://doi.org/10.1002/adma.201801334>
206. H. Ying, P. Huang, Z. Zhang, S. Zhang, Q. Han et al., Free-standing and flexible interfacial layer enables bottom-up Zn deposition toward dendrite-free aqueous Zn-Ion batteries. *Nano-Micro Lett.* **14**(1), 180 (2022). <https://doi.org/10.1007/s40820-022-00921-6>
207. L. Ma, J. Cui, S. Yao, X. Liu, Y. Luo et al., Dendrite-free lithium metal and sodium metal batteries. *Energy Storage Mater.* **27**, 522–554 (2020). <https://doi.org/10.1016/j.ensm.2019.12.014>
208. C. Zhang, A. Wang, J. Zhang, X. Guan, W. Tang et al., 2D materials for lithium/sodium metal anodes. *Adv. Energy Mater.* **8**(34), 1802833 (2018). <https://doi.org/10.1002/aenm.201802833>
209. Z. Li, K. Zhu, P. Liu, L. Jiao, 3D confinement strategy for dendrite-free sodium metal batteries. *Adv. Energy Mater.* **12**(4), 2100359 (2022). <https://doi.org/10.1002/aenm.20210359>
210. C. Wei, Y. Tao, Y. An, Y. Tian, Y. Zhang et al., Recent advances of emerging 2D MXene for stable and dendrite-free metal anodes. *Adv. Funct. Mater.* **30**(45), 2004613 (2020). <https://doi.org/10.1002/adfm.202004613>
211. K. Sun, Y. Shen, J. Min, J. Pang, Y. Zheng et al., MOF-derived Zn/Co Co-Doped MnO/C microspheres as cathode and $Ti_3C_2@Zn$ as anode for aqueous zinc-ion full battery. *Chem. Eng. J.* **454**, 140394 (2023). <https://doi.org/10.1016/j.cej.2022.140394>
212. X. Li, M. Li, K. Luo, Y. Hou, P. Li et al., Lattice matching and halogen regulation for synergistically induced uniform zinc electrodeposition by halogenated Ti_3C_2 MXenes. *ACS Nano* **16**(1), 813–822 (2022). <https://doi.org/10.1021/acsnano.1c08358>
213. M. Wang, Y. Tang, A review on the features and progress of dual-ion batteries. *Adv. Energy Mater.* **8**(19), 1703320 (2018). <https://doi.org/10.1002/aenm.201703320>
214. L. Dong, W. Yang, W. Yang, Y. Li, W. Wu et al., Multivalent metal ion hybrid capacitors: a review with a focus on zinc-ion hybrid capacitors. *J. Mater. Chem. A* **7**(23), 13810–13832 (2019). <https://doi.org/10.1039/C9TA02678A>
215. N. Choudhary, C. Li, J. Moore, N. Nagaiah, L. Zhai et al., Asymmetric Supercapacitor electrodes and devices. *Adv. Mater.* **29**(21), 1605336 (2017). <https://doi.org/10.1002/adma.201605336>
216. Q. Wu, P. Li, Y. Wang, F. Wu, Construction and electrochemical energy storage performance of free-standing hexagonal Ti_3C_2 film for flexible supercapacitor. *Appl. Surf. Sci.* **593**, 153380 (2022). <https://doi.org/10.1016/j.apsusc.2022.153380>
217. M.R. Lukatskaya, O. Mashtalir, C.E. Ren, Y. Dall'Agnese, P. Rozier et al., Cation intercalation and high volumetric capacitance of two-dimensional titanium carbide. *Science* **341**(6153), 1502–1505 (2013). <https://doi.org/10.1126/science.1241488>
218. U. Khan, Y. Luo, L.B. Kong, W. Que, Synthesis of fluorine free MXene through lewis acidic etching for application as



- electrode of proton supercapacitors. *J. Alloys Compd.* **926**, 166903 (2022). <https://doi.org/10.1016/j.jallcom.2022.166903>
219. Y. Zhang, Z. Zhao, C. Luo, X. Wu, W. Chen, Toward understood the electrochemical capacitance mechanism of MXene by intercalation of inorganic ions and organic macromolecular ions. *Appl. Surf. Sci.* **578**, 152030 (2022). <https://doi.org/10.1016/j.apsusc.2021.152030>
220. C. Jing, B. Dong, Y. Zhang, Chemical modifications of layered double hydroxides in the supercapacitor. *Energy Environ. Mater.* **3**(3), 346–379 (2020). <https://doi.org/10.1002/eem2.12116>
221. D. Zhang, J. Cao, X. Zhang, N. Insin, R. Liu et al., NiMn layered double hydroxide nanosheets in-situ anchored on Ti₃C₂ MXene via chemical bonds for superior supercapacitors. *ACS Appl. Energy Mater.* **3**(6), 5949–5964 (2020). <https://doi.org/10.1021/acsaem.0c00863>
222. Z. Zhao, X. Wu, C. Luo, Y. Wang, W. Chen, Rational design of Ti₃C₂Cl₂ MXenes nanodots-interspersed MXene@NiAl-layered double hydroxides for enhanced pseudocapacitor storage. *J. Colloid Interface Sci.* **609**, 393–402 (2022). <https://doi.org/10.1016/j.jcis.2021.12.041>
223. H. Liu, L. Syama, L. Zhang, C. Lee, C. Liu et al., High-entropy alloys and compounds for electrocatalytic energy conversion applications. *SusMat* **1**(4), 482–505 (2021). <https://doi.org/10.1002/sus2.32>
224. J. Pang, B. Chang, H. Liu, W. Zhou, Potential of MXene-based heterostructures for energy conversion and storage. *ACS Energy Lett.* **7**(1), 78–96 (2022). <https://doi.org/10.1021/acsenenergylett.1c02132>
225. A. Rajagopal, K. Yao, A.K. Jen, Toward perovskite solar cell commercialization: a perspective and research roadmap based on interfacial engineering. *Adv. Mater.* **30**(32), 1800455 (2018). <https://doi.org/10.1002/adma.201800455>
226. Y. Zhang, L. Xu, J. Sun, Y. Wu, Z. Kan et al., 24.11% high performance perovskite solar cells by dual interfacial carrier mobility enhancement and charge-carrier transport balance. *Adv. Energy Mater.* **12**(37), 2201269 (2022). <https://doi.org/10.1002/aenm.202201269>
227. L. Yin, Y. Li, X. Yao, Y. Wang, L. Jia et al., MXenes for solar cells. *Nano-Micro Lett.* **13**(1), 78 (2021). <https://doi.org/10.1007/s40820-021-00604-8>
228. X. Liu, Z. Zhang, J. Jiang, C. Tian, X. Wang et al., Chlorine-terminated MXene quantum dots for improving crystallinity and moisture stability in high-performance perovskite solar cells. *Chem. Eng. J.* **432**, 134382 (2022). <https://doi.org/10.1016/j.cej.2021.134382>
229. L. Wang, Y. Hao, L. Deng, F. Hu, S. Zhao et al., Rapid complete reconfiguration induced actual active species for industrial hydrogen evolution reaction. *Nat. Commun.* **13**(1), 5785 (2022). <https://doi.org/10.1038/s41467-022-33590-5>
230. K. Khan, A.K. Tareen, M. Iqbal, Y. Zhang, A. Mahmood et al., Recent advance in MXenes: new horizons in electrocatalysis and environmental remediation technologies. *Prog. Solid State Chem.* **68**, 100370 (2022). <https://doi.org/10.1016/j.progsolidstchem.2022.100370>
231. X. Bai, J. Guan, MXenes for electrocatalysis applications: modification and hybridization. *Chin. J. Catal.* **43**(8), 2057–2090 (2022). [https://doi.org/10.1016/S1872-2067\(21\)64030-5](https://doi.org/10.1016/S1872-2067(21)64030-5)
232. R. Luo, R. Li, C. Jiang, R. Qi, M. Liu et al., Facile synthesis of cobalt modified 2D titanium carbide with enhanced hydrogen evolution performance in alkaline media. *Int. J. Hydrogen Energy* **46**(64), 32536–32545 (2021). <https://doi.org/10.1016/j.ijhydene.2021.07.110>
233. J. Jiang, S. Bai, M. Yang, J. Zou, N. Li et al., Strategic design and fabrication of MXenes-Ti₃CNCl₂@CoS₂ core-shell nanostructure for high-efficiency hydrogen evolution. *Nano Res.* **15**(7), 5977–5986 (2022). <https://doi.org/10.1007/s12274-022-4276-8>
234. Z. Wu, H. Zong, B. Fu, Z. Zhang, MXene with controlled surface termination groups for boosting photoelectrochemical water splitting. *J. Mater. Chem. A* **10**(46), 24793–24801 (2022). <https://doi.org/10.1039/D2TA06313A>
235. X. Li, L. Zhao, J. Yu, X. Liu, X. Zhang et al., Water splitting: from electrode to green energy system. *Nano-Micro Lett.* **12**(1), 131 (2020). <https://doi.org/10.1007/s40820-020-00469-3>
236. Y. Tang, C. Yang, X. Xu, Y. Kang, J. Henzie et al., MXene nanoarchitectonics: defect-engineered 2D MXenes towards enhanced electrochemical water splitting. *Adv. Energy Mater.* **12**(12), 2103867 (2022). <https://doi.org/10.1002/aenm.202103867>
237. B. Sarfraz, M.T. Mehran, M.M. Baig, S.R. Naqvi, A.H. Khoja et al., HF free greener Cl-terminated MXene as novel electrocatalyst for overall water splitting in alkaline media. *Int. J. Energy Res.* **46**(8), 10942–10954 (2022). <https://doi.org/10.1002/er.7895>
238. L. Li, I.M.U. Hasan, R. He, L. Peng et al., Copper as a single metal atom based photo-, electro-, and photoelectrochemical catalyst decorated on carbon nitride surface for efficient CO₂ reduction: a review. *Nano Res. Energy* **1**, e9120015 (2022). <https://doi.org/10.26599/NRE.2022.9120015>
239. J. Pang, R.G. Mendes, A. Bachmatiuk, L. Zhao, H.Q. Ta et al., Applications of 2D MXenes in energy conversion and storage systems. *Chem. Soc. Rev.* **48**(1), 72–133 (2019). <https://doi.org/10.1039/C8CS00324F>
240. Q. Tang, P. Xiong, H. Wang, Z. Wu, Boosted CO₂ photoreduction performance on Ru-Ti₃CN MXene-TiO₂ photocatalyst synthesized by non-HF lewis acidic etching method. *J. Colloid Interface Sci.* **619**, 179–187 (2022). <https://doi.org/10.1016/j.jcis.2022.03.137>
241. Y. Wan, J. Xu, R. Lv, Heterogeneous Electrocatalysts design for nitrogen reduction reaction under ambient conditions. *Mater. Today* **27**, 69–90 (2019). <https://doi.org/10.1016/j.mattod.2019.03.002>
242. T. Najam, S.S.A. Shah, L. Peng, M.S. Javed, M. Imran et al., Synthesis and nano-engineering of MXenes for energy conversion and storage applications: recent advances and perspectives. *Coord. Chem. Rev.* **454**, 214339 (2022). <https://doi.org/10.1016/j.ccr.2021.214339>

243. S. Xiao, Y. Zheng, X. Wu, M. Zhou, X. Rong et al., Tunable structured MXenes with modulated atomic environments: a powerful new platform for electrocatalytic energy conversion. *Small* **18**(41), 2203281 (2022). <https://doi.org/10.1002/sml.202203281>
244. Y. Wang, Y. Sun, H. Li, W. Zhang, S. Wu et al., Controlled etching to immobilize highly dispersed Fe in MXene for electrochemical ammonia production. *Carbon Neutralization* **1**(2), 117–125 (2022). <https://doi.org/10.1002/cnl.12.18>
245. J. Pang, S. Peng, C. Hou, X. Wang, T. Wang et al., Applications of MXenes in human-like sensors and actuators. *Nano Res.* (2022). <https://doi.org/10.1007/s12274-022-5272-8>
246. M. Wu, Y. An, R. Yang, Z. Tao, Q. Xia et al., $V_2C_2T_x$ and $Ti_3C_2T_x$ MXenes nanosheets for gas sensing. *ACS Appl. Nano Mater.* **4**(6), 6257–6268 (2021). <https://doi.org/10.1021/acsnm.1c01059>
247. X. Xi, J. Wang, Y. Wang, H. Xiong, M. Chen et al., Preparation of Au/Pt/ $Ti_3C_2Cl_2$ nanoflakes with self-reducing method for colorimetric detection of glutathione and intracellular sensing of hydrogen peroxide. *Carbon* **197**, 476–484 (2022). <https://doi.org/10.1016/j.carbon.2022.06.068>
248. J. Cheng, C. Li, Y. Xiong, H. Zhang, H. Raza et al., Recent advances in design strategies and multifunctionality of flexible electromagnetic interference shielding materials. *Nano-Micro Lett.* **14**(1), 80 (2022). <https://doi.org/10.1007/s40820-022-00823-7>
249. R. Yang, X. Gui, L. Yao, Q. Hu, L. Yang et al., Ultrathin, lightweight, and flexible CNT buckypaper enhanced using MXenes for electromagnetic interference shielding. *Nano-Micro Lett.* **13**(1), 66 (2021). <https://doi.org/10.1007/s40820-021-00597-4>
250. K. Wang, W. Chu, H. Li, Y. Chen, Y. Cai et al., Ferromagnetic Ti_3CNCl_2 -decorated RGO aerogel: from 3D interconnecting conductive network construction to ultra-broadband microwave absorber with thermal insulation property. *J. Colloid Interface Sci.* **604**, 402–414 (2021). <https://doi.org/10.1016/j.jcis.2021.05.166>
251. C. Chen, X. Zhao, Y. Chen, W. Chu, Y. Wu et al., Photoinduced dual shape programmability of covalent adaptable networks with remarkable mechanical properties. *Nano Lett.* **22**(21), 8413–8421 (2022). <https://doi.org/10.1021/acs.nanolett.2c02181>

